UNIVERSITÀ DEGLI STUDI CATANIA

DIPARTIMENTO DI FISICA E ASTRONOMIA

Dottorato di Ricerca di Fisica

PAGANO EMANUELE VINCENZO

Space-time correlations of intermediate mass fragments emitted in heavy ion reactions at Fermi energy by intensity interferometry studied with CHIMERA and perspectives

Coordinatore: Prof. F. Riggi

Tutors:
Prof.ssa F. Rizzo
Dr. E. De Filippo
Dr. P. Russotto
Dr. G. Verde

XXVIII Ciclo (2013-2016)

"Dedicated to my two little baby girls,

Greta and Alice"

INDEX

Page

LIST OF TABLES

…… *IV*

LIST OF FIGURES

…… *V*

Chapter 1

1. Introduction

…….. *1*

Chapter 2

2. Basic aspects of the heavy ion physics

…….. *5*

2.1 The low energy HI collisions

…….. *6*

2.2 The high-energy HI collisions

…….. *10*

2.3 The H.I. Fermi energy domain

…….. *12*

2.3.1 Semi-peripheral collisions

…….. *15*

2.3.2 Time scale in Neck fragmentation

…….. *17*

2.3.3 Central collisions

…… *24*

2.3.4 Multifragmentation

…… *27*

2.3.5 Liquid-gas phase transition

…… 35

2.4 Theory and phenomenology basics of two particle correlation in intensity interferometry scenario.

……40

2.4.1 Historical introduction

…… 40

2.4.2 Correlation in nuclear physics

…… 44

2.4.3 Theory and phenomenological basis of two-proton correlation function

…… ...49

2.4.4 The case of the IMF-IMF correlation function

…… 58

Chapter 3

3. Signals of dynamical and statistical processes from IMF-IMF correlation function in the production of heavy fragments in PLF decay

…… 62

3.1 Theoretical comparisons

…… 93

Chapter 4

4. FARCOS, Femtoscope Array for Correlation and Spectroscpy

…… 99

4.1 Introduction

…… 99

4.2 Description

…… 102

4.3 First test with radioactive source and beam during the InKiIsSy experiment

…… 104

4.4 Light particles identification

…… 129

4.5 A new versatile electronic: GET (Generic electronic for TPC)

…… 133

4.6 Milestones and cost evaluation

…… 139

Chapter 5

5. Future perspectives: neutron detection

…….. 141

5.1 EJ-299-33 plastic scintillator: test with sources

…….. 145

Chapter 6

6. Conclusions

…… . 153

ACKNOWLEDGEMENTS

…….. 157

BIBLIOGRAPHY

…….. 159

List of Tables

Table Page

Chapter 4

1. *Summary upon the comparisons of the two ways for the identification procedure between the first two stages.* *129*

2. *Milestones of FARCOS construction.* *139*

3. *Cost predictions in k€.* *140*

List of Figures

Figure Page

Chapter 2

1. *Schematic view of Hi collision pattern at Coulomb energy.* *9*

2. *Reduced widths σ_0 measured for ^{40}Ar fragmentation at 213 MeV/nucl., ^{16}O fragmentation at 2100 MeV/nucl., and ^{12}C fragmentation at 1050 and 2100 MeV/nucl.. The data represent the mean value and spread of σ_0 for each fragment mass K (A_F in formula 1). The dashed line is the original σ_0 prediction by Goldhaber. (figure adapted from [MUR84]).* *13*

3. *Mean IMF multiplicity for $^{84}Kr+^{197}Au$ collisions as a function of beam energy (figure adapted from [LYN95]).* *13*

4. *Charge identification as a function of parallel velocity for heavy fragments in ternary events detected in the reaction $^{124}Sn+^{64}Ni$ at E_{lab}=35MeV/nucleon. Adapted from Figure 2 of Ref. [DEF05].* *19*

5. *Relative Kinetic energy correlation for the $^{124}Sn+^{64}Ni$ at E_{lab}=35MeV/nucleon (see text for description). Values of time scale are calculated in appendix of reference [DEF05].* *23*

6. Dynamical and statistical evaluation adapted from [DEF14]. *23*

7. *Evolution of the ratio between two and three body decays as function of the excitation energy of the ''composite'' system of mass in the range A = 200-220 amu from central and semi-central collisions. Adapted from[GER11].* *25*

8. *Evolution of the ratio of complete fusion cross section and reaction cross section as a function of the energy for six different systems [GER11].* *26*

9. *Mean IMFs multiplicity as a function of reduced impact parameter for four different incident energy from Aladin collaboration [GER11].* *28*

10. *Rise and fall of multi-fragmentation (in terms of reduced IMF multiplicity vs excitation energy) as observed by Aladin and Indra collaborations[GER11].* *29*

11. *Fragment emission time vs. excitation energy evaluated for several systems: for E*≥4-5 MeV it is possible to observe time saturation at about 100 fm/c [DUR01].* 30

12. *Isotherm curves in the pressure – density plane. In such representation the saturation point corresponds to the zero pressure point at finite density . The dashed lines correspond instead to the mechanical instabilities of the spinodal region [DUR01 and reference therein].* 32

13. *Systematic of the radial expansion energy as a function of excitation energy per nucleon in central collisions at Fermi energies [DUR01 and reference therein].* 34

14. *Typical fragment size distribution fitted by a power law. [CHO99].* 35

15. *Systematic of measured nuclear temperatures with the three different methods briefly discussed in the following of the section [DUR01 and references therein].* 36

16. *Schematic description of the three methods used in measuring temperature of emitting sources in nuclear collisions [GER11].* 37

17. *Schematically picture of an amplitude (Michelson) interferometer measures the single-body detection probability [EVP12].* 41

18. *Schematically picture of intensity interferometer (HBT) which measure the two-particle yields [EVP12].* 42

19. *Schematically represent of a nuclear experiment.* 44

20. *Correlation function π^+-π^+ (left panel) and π^--π^- measured in Au+Au at E/A=10.8 GeV from E877 collaboration at AGS laboratory of Brookhaven [EVP12, BARR97].* 47

21. *Space-time characterization of an emitting source using a p-p correlation function with the Gaussian approach [EPV12, EVP13, EVP13b, EVP14].* 53

22. *Imaging reconstructed p-p correlation function [EPV12, EVP13, EVP13b, EVP14].* 54

23. *Imaging evaluated source function.* 54

24. *Finite half-time effect on the source size [EPV12, EVP13, EVP13b, EVP14].* 55

25. *Directional p-p correlation functions measured in central collisions of Ar+Sc at 80 AMeV. Full circle: parallel correlation function; Open circle: transverse correlation function [LIS93].* *56*

Chapter 3

1. *The charge vs the parallel velocity of the detected particles in the experiment.* *63*
2. *Correlation between the relative velocity of IMF and TLF (Y axis) and IMF and PLF (X axis) (normalized to the Viola velocity) for different charge of IMF (4, 8, 12, 18) [VIO85].* *68*
3. *Charge vs parallel (to the beam axis) velocity for all charged particles detected in the experiment; the particles of interest in this analysis (see text) are those in the not hatched region* [EVP16]. *71*
4. *IMF-IMF correlation function for* $25 \leq Z_H + Z_L \leq 50$ *gated by different* Z_{Asy} *[EVP16].* *73*
5. $Z_H + Z_L$ *as a function of both the parallel velocity of the light IMF (top panel) and the parallel velocity of the heavy one (bottom panel) in the three ranges of* Z_{Asy} $(25 \leq Z_H + Z_L \leq 50)$ *[EVP16].* *75*
6. *Left. Total charged particles multiplicity (black line) and IMFs multiplicity for the three range of* Z_{Asy}*. In the top-right figure the same spectrum in linear scale to empathize the cross section differences. Right. The reduced impact parameter estimation according to Cavata method [CAV90].* *76*
7. *Total charged multiplicity for different* $Z_{Asy,}$ *selected ranges are* $25 \leq Z_H + Z_L \leq 35$ *(left panel) and* $35 \leq Z_H + Z_L \leq 50$ *(right panel) [EVP16].* *78*
8. $Z_H + Z_L$ *as a function of both the parallel velocity of the light IMF (top panel) and the parallel velocity of the heavy one (bottom panel) in the three ranges of* Z_{Asy} *in the most dissipative bin of sum* $25 \leq Z_H + Z_L \leq 35$**.** *80*
9. $Z_H + Z_L$ *as a function of both the parallel velocity of the light IMF (top panel) and the parallel velocity of the heavy one (bottom panel) in the three ranges of* Z_{Asy} *in the less dissipative bin of sum* $35 \leq Z_H + Z_L \leq 50$*.* *80*
10. *IMF-IMF correlation functions for different* Z_{Asy}*, left panel* $25 \leq Z_H + Z_L \leq 35$ *and* $35 \leq Z_H + Z_L \leq 50$ *right panel [EVP16].* *81*

11. *Ratio between the relative velocity of the two IMFs and the Viola velocity of the two IMFs for $25 \leq Z_H + Z_L \leq 35$ in the three ranges of charge asymmetry.* 83

12. *Ratio between the relative velocity of the two IMFs and the Viola velocity of the two IMFs for $35 \leq Z_H + Z_L \leq 50$ in the two (see text) ranges of charge asymmetry.* 84

13. *Schematic representation of the cosine of theta proximity angle.* 85

14. *Invariant cross section in the case of asymmetric breakup (left) and symmetric one (right) [DEF16b].* 86

15. *Ratio between relative velocity and the Viola velocity for the two IMFs.* 87

16. *Distribution of the cosine of theta proximity for the most symmetric IMFs ZAsy and for $25 \leq Z_H + Z_L \leq 50$ [EVP16].* 88

17. *The IMF-IMF correlation function gated in the cosine of theta proximity(black stars) and without conditions (white circle)[EVP16].* 89

18. *Ratio V_{rel}/V_{Viola} for $\cos\theta_{Prox} < 0.8$ (black spectrum) and for $\cos\theta_{Prox} \geq 0.8$ (red spectrum).* 91

19. *Comparisons between experimental (full lines) and simulate variable (dashed lines) [EVP16].* 94

20. *Calculated impact parameter distribution after the constrains.* 96

21. *Comparison between experimental (black points) and simulated (red points) correlation functions [EVP16].* 97

Chapter 4

1. *Schematic view of a cluster of FARCOS.* 103

2. *Typical matrix of uniformity gradient of a CsI(Tl) [EVP12][QUA14].* 105

3. *The InKiIsSy experimental setup. $^{124}Xe+^{64}Ni$ @ 35 AMeV was the studied reaction [EVP16b].* 106

4. *Schematic view of the prototype of the PAC of FARCOS (top of the figure). Picture of the PAC (bottom).* *107*
5. *Total hits multiplicity for the first front stage of DSSSD (top) and for the second stage front (bottom-left) and back (bottom-right).* *109*
6. *Constrained spectra (see Figure 5).* *110*
7. *Energy spectra in QDC channels the strip number 10 of the 300μm DSSSD of the telescope N°1 (no cut).* *111*
8. *Red spectrum like figure 7, the black one have the condition of* $Mult_{Hits}>8$. *112*
9. *Comparison among the three spectra without cut (red) and with the two conditions* $Mult_{Hits}>8$ *(black) and* $1\leq Mult_{Hits}\leq 8$ *(blue).* *113*
10. *ΔE-E identification matrix between the first two stages of DSSSDs without any conditions.* *114*
11. *ΔE-E Identification matrix between the first two stage of DSSSD for* $1\leq Mult_{Hits}\leq 8$. *116*
12. *ΔE-E Identification matrix between the first two stage of DSSSD for* $Mult_{Hits} > 8$. *117*
13. *ΔE-E Identification matrix between the first two stage of DSSSD respectively N°5 and N°27.* *118*
14. *ΔE-E Identification matrix between the first two stage of DSSSD respectively N°5 and N°15.* *119*
15. *Schematic view of the "Effetto Calotta".* *121*
16. *ΔE-E identification matrixes between 1 strip in the first stage and 1 strip in the second DSSSD stage for 320 runs after the pulser calibration in mV [EVP15]* *123*
17. *ΔE-E identification matrixes between 8 strips in the first stage (8-15) and 8 strips in the second DSSSD stage (16-23) for 40 runs after the pulser calibration in mV [EVP15].* *125*
18. *Comparison of the isotopic identification resolution in the two adopted identification procedures for* $3\leq Z\leq 6$ *[EVP15].* *126*
19. *Comparison of the isotopic identification resolution in the two ways for* $7\leq Z\leq 10$ *[EVP15].* *127*

20. *Typical identification matrix for the CsI(Tl) PSD (Fast/Slow) of a crystal form the telescope N°1 of FARCOS [EVP16b].* *131*

21. *The second part of the same matrix figure 20 [EVP16b].* *132*

22. *Schematic view of the GET electronic.* *134*

23. *Comparison between CHIMERA acquisition (left panel) and GET acquisition (right panel) in the case of CsI(Tl).* *135*

24. *Comparison between CHIMERA acquisition (left panel) and GET acquisition (right panel) in the case of DSSSD test using alpha source.* *136*

25. *The CLIR experimental setup. FARCOS is positioned in the CHIMERA scattering chamber [EVP16b].* *136*

26. *The so-called "Cocktail Beams" from the FRIBS facility od LNS in the case of CLIR experiment.* *137*

27. *Comparison between two ΔE-E identification matrixes obtained in the reaction $^{16}C+^{12}C$ at 40 AMeV (CLIR experiment) from two telescopes of CHIMERA detector of the same ring 2. Left: signal processed by GET. Right: signal processed by standard CHIMERA electronic [EVP16b].* *138*

Chapter 5

1. *(color line). Two-nucleon correlation functions gated on the total momentum of nucleon pairs. Adapted from [CHE03].* *142*

2. *a) Two-neutron correlation function; b) two-proton correlation function; c) n-p correlation function. In b) and c) there is also the comparison with the "event-mixing" technique (open circles) and the "single-product" technique (black dots). Adapted from [GHE00].* *143*

3. *Principal properties of the plastic scintillator [ELJTE].* *145*

4. *Emission spectrum of the EJ299-33 [ELJTE].* *146*

5. *Geometrical configuration of the EJ-299-33 [ELJTE].* *146*

6. *Particle identification patterns for 11 isotopes ranging from hydrogen to carbon. Plotted is the total light output in units of electron-equivalent MeV (abscissa) and the energy lost by the*

particle in the first transmission silicon detector ΔE (ordinate) adapted from [NYI13].
…….. *147*

7. *Pulse shape discrimination pattern for γ-rays, protons, α-particles and heavier fragments obtained using a conventional two-gate, two-channel QDC measurement as applied to the anode signals of the EJ 299-33 scintillation detector. Plotted on the ordinate axis is the PID signal derived from the two portions of the charge, total and tail, extracted from the anode of the EJ 299-33 detector assembly. Adapted from [NYI13].*
…….. *147*
8. *Test of the EJ-299-33 close to the first ring of CHIMERA detector.*
…….. *148*
9. *Test of the EJ-299-33 close to the sphere of the CHIMERA detector.*
…….. *149*
10. *Am-Be neutron source spectrum.*
…….. *150*
11. *PSD discrimination matrix of the EJ-299-33 using at the same time ^{60}C and Am-Be sources.*
…….. *150*
12. *PSD discrimination matrix of the EJ-299-33 using at the same time ^{232}Th and Am-Be sources.*
…….. *151*
13. *EJ-280 optical spectrum useful for wave length shifter.*
…….. *152*

1. INTRODUCTION

This PhD work is faced with some of the relevant physics cases and experimental problems related with the design, construction and experimental tests of a new multi detector array, characterised by both high energy and angular resolutions, devoted to the measurements of different multi correlation properties among charged particles which are abundantly produced in heavy-ion nuclear reactions with both stable and exotic beams with particular applications to the Fermi energy domain (10 AMeV - 200 AMeV).

Introductions about different physics cases and open questions of now-day scientific research (related to the proposal to design a new correlator) are described in second chapter of this work together with the underlying nuclear mechanics involved in heavy ion collisions at intermediate energies. Also, in the same chapter the expected performances of the new multi-detector array (FARCOS presented in chapter 4, see text) are linked to the proposal to produce sizeable advancements on the charged light particles (p-p, p-d,…), possible extension to n,p (or the more difficult task of n,n) and Intermediate mass fragment IMF-IMF correlations by the intensity interferometry technique (HBT).

In the third chapter will be presented a completely new application of the HBT technique in the IMF-IMF correlation function in order to perform a kind of “calibration” for correlation function in a well-studied physics case, that is the dynamical fission of the PLF in $^{124}Sn + ^{64}Ni$ at 35 AMeV as seen from CHIMERA detector. We also made simulations with the CoMD-II theoretical model in order to

compare the experimental IMF-IMF correlation function to the simulated one in the context of transport theory .

A basic description of the multi detector array FARCOS (Femtoscope ARray for COrrelation and Spectroscopy) is illustrated in the fourth chapter and the main steps of its construction, with particular emphasis on the preliminary tests performed with nuclear radioactive source (off beam); some results from on beam experiments are also discussed. In particular, a prototype made by 4 basic modules of FARCOS was tested on beam during the INKIISSY experiment performed in April 2013 with stable beam and during the CLIR experiment performed in March 2015 using the In Flight method to produce radioactive beam, both of them performed at INFN – Laboratori Nazionali del Sud in Catania (LNS). In particular, in chapter 4 these latter experiments and some of their results are discussed in some details (in particular the INKIISSY case), in connection with their different physics cases and the obtained performances of the first FARCOS prototype; in particular it is also shown the new electronic, the GET one, that we are planning to use for both CHIMERA and FARCOS arrays.

The energy regime where FARCOS was thought to be in operation is, as already mentioned above, the Fermi Energy domain that is characterised by a rich and unique phenomenology due to the strong persistence of typical phenomena of the low–energy Coulomb regime and the increasing importance with the energy of the nucleon-nucleon dissipative mechanisms. In fact, depending on incident energy and impact parameter, an impressive range of physical phenomena occur within large time-scales (from 10 to 1000 fm/c) with the excitation of

different degrees of freedom which are revealed to the measurements through imprints on space-time and particle-particle correlations.

Beside applications in the Fermi energy domain, it is also envisaged to couple the new correlator with devices mostly involved in different energy domains. An important example is the real possibility to further explore the symmetry energy term of nuclear matter at density well above the normal density ρ_0 (0.17 nucleon/fm^3), starting from previous experiment performed at GSI for the Au+Au system [RUS16]. The proposal is under study in our scientific collaboration and it is aimed to suggest a new experiment to be performed at GSI in a next future and at higher energies roughly ranging in the domain of 500 MeV/u to 1000 MeV/u.

Another important possibility opened by incoming experimental processes is to use FARCOS in the lower energy regime (10-15 MeV/u), in particular by studying the reaction mechanism and thermodynamics with exotic beams of the new facilities under construction like SPES at INFN-LNL (Laboratori Nazionali di Legnaro, Italy) or SPIRAL II at GANIL (France).

The main experimental effort and financial support in designing, testing and building the new array, FARCOS came principally from PRIN as supported by MIUR (2010-2013), and from the EXOCHIM (2010-2015) and NEWCHIM (2016-2020) experiments as supported by the INFN national nuclear committee (gruppo III) in Italy.

In chapter five, the future possibility of neutrons detections associated with FARCOS array is presented. In the first part of the chapter it is discussed the critical importance of neutron detection and the associated physical topics. In the second part we will show

preliminary tests performed at Laboratori Nazionali del Sud – INFN, on the new plastic scintillator EJ-299-33 with ^{12}C beam at 20 AMeV and using radioactive source to study its discrimination capabilities for charged particles, gamma and neutrons. Also others beam tests were performed, however , the results are under analysis and they will be presented in a future paper.

Finally in chapter six we summarize and conclude the work done in this PhD thesis and, taking into account indications from the studies descripted in the previous chapters (2, 3) we report also the next future perspectives.

2. Basic aspects of the heavy ion physics

In this work, particular attention to heavy-ion collisions (HI) at Fermi energy regime (E/A ~ 50MeV/nucleon - Nuclear Temperature ≤ 10MeV) is devoted. Besides that, introductions to the basic phenomenology of HI collisions at energy close to the Coulomb barrier of the two interacting ions (E/A ≤ 10MeV/nucleon - Nuclear Temperature ~ few MeV) and to moderately high energy regime (E/A ~few GeV/nucleon and Nuclear Temperature ~ tens of MeV) are also briefly discussed. Heavy Ion collisions in the regime of Quark-Gluon-Plasma (QGP) transition that is a subject of major interest in HI physics in the relativistic regime (E/A ~ hundreds of GeV/nucleon and Nuclear Temperature ~ 100MeV) is not discussed. However, it is important to notice that in this energy region HBT interferometry, that is the general methods discussed in detail in this work, is one of the investigation methods of major application [BAL16].

2.1 The low energy HI collisions

In the low energy domain (E ≈ 10-20 MeV/nucleon), the reaction mechanism is strongly dominated by the Coulomb barrier potential between the two interaction ions, depending on the impact parameter and the sizes of the colliding nuclei. Typical phenomena are: compound nucleus formation, incomplete fusion and deep inelastic reactions and fission (see figure 1) [BIR83, WIL76 NGO78, GRE85, BON86]. In this regime strong dissipations of both relative energy and angular momentum play a dominant role with the excitation of thermal and collective degrees of freedom. The two-body nucleon-nucleon (n-n) collisions are strongly inhibited by the quantum effect of Pauli blocking and the one body, i.e., mean-field energy dissipation, dominates the reaction mechanism. Very briefly the observed phenomenology is summarised as it follows. For large angular momenta (very close to grazing conditions of the two colliding nuclei) or, in a semi-classical picture, for large (grazing) impact parameters, it is possible to observe elastic scattering of projectile and target and inelastic collisions that are characterized by the mutual excitation of projectile and target in the exit channel as well stripping and pickup reactions. In these cases it is useful to classify the mechanisms as it was associated with peripheral collisions. With the decrease of the impact parameter below the grazing condition, binary Deep Inelastic Collisions (DIC) and multi-nucleon transfer reactions become the dominant aspects of the reaction [RAN81, RAN82]. Two correlated fragments in momentum space, the Projectile-Like Fragment (PLF) and

the Target-Like Fragment (TLF), of charge (mass) very close, respectively, to the projectile and target charges (masses) are observed. A large fraction of the relative kinetic energy is dissipated into internal degrees of freedom of the two systems (PLF and TLF) and it is shared between the two partners and, as final stage, converted in thermal excitation energy and collective rotation of high spin states. Angular correlations are substantially broadened (with respect to a typical two-body kinematics with only two bodies in the final stage) by a fast (10^{-22}-10^{-21}s) nucleon exchange between projectile and target and subsequent evaporation decay. Typical excitation energy of both PLF* and TLF*, as deduced by experimental total kinetic energy loss, of the order of 2-3 MeV/nucleon are observed in the exit channel. As a consequence of the sequential de-excitation towards the grounds states, an important multiplicity of statistically emitted light charged particles, neutrons and gamma rays are also observed. The reactions take place in a short time scale, of the order of 10^{-20}-10^{-22}s along with the paths of semi-classical trajectories close to the grazing one. The amount of the total excitation energy shared between the two primary partners could be studied by measuring the particle energy spectra and multiplicities associated with the PLF and TLF nuclei, respectively, in order to obtain quantitative information on the degree of equilibration of the internal degrees of freedom during the dissipative process. Under the assumption that a full equilibrium process is achieved in the binary system, as result of the interaction, the amount of excitation energy shared between the two primary partners

should be proportional to their respective mass numbers. Alternatively, in the extreme case of a fast non equilibrated process it is expected that equal amount of excitation energy is shared between the two primary partners, nearly independently by their masses. Neutron multiplicity measurements are important tools in these studies [FIO94].

For more central collisions (with substantial smaller impact parameters than the grazing one) between two medium mass nuclei (A_{proj}, $A_{targ} \leq 100$) the reaction mechanism is dominated by Compound Nucleus (CN) formation and light particles and gamma evaporation decays. If the excitation energy is relatively high, after the equilibration of the internal degrees of freedom during a time of the order of 10^{-16}-10^{-19}s, the CN can produce the fission in two lighter fragments that, sequentially, undergo a statistical de-excitation process by evaporation or gamma emission. For heavier interacting nuclei (A_{proj}, $A_{targ} > 100$) the Coulomb field in the entrance channel is too large for allowing an efficient formation of CN and, consequently, the persistence of DIC-like phenomena with a rapid re-separation of the two interacting PLF and TLF nuclei is observed and it is well reproduced in the context of semi classical predictions [WIL76] .

In this low energy domain the equilibration process of various degrees of freedom (isospin, excitation energy, shape, …) as a function of mass asymmetry, isospin, and beam energy, of a long living (10^{-16} s) fusion like system is studied by measuring single and coincidence energy spectra

and the possible deviation from an isotropic evaporation of Maxwellian-like energy distribution (with a slope representing the average temperatures of the residual nucleus) of the emitted light particles, whose relative abundances have to be compared either with the predictions of Hauser - Feshbach (HF) evaporative statistical codes (determined by the available phase space, nuclear level density parameters and transmission coefficients) [BER09] or with phenomenological energy distribution formulas for volume or surface emission [GOL78].

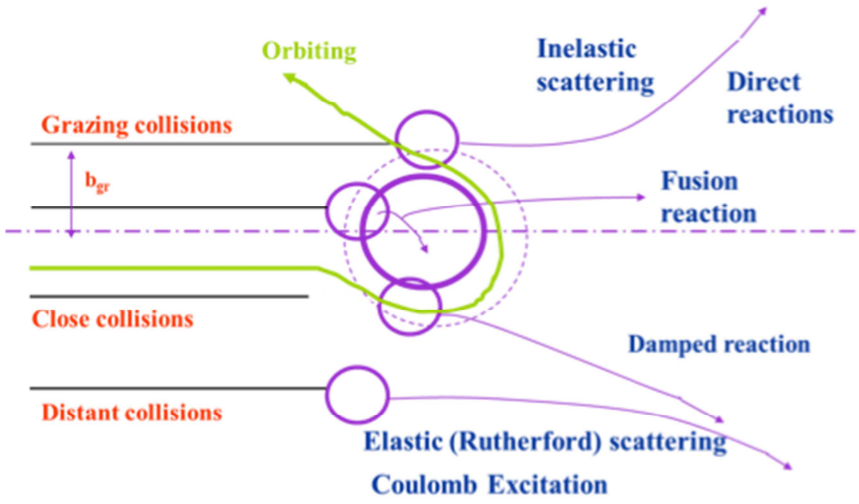

Figure 1: Schematic view of HI collisions pattern at Coulomb energy.

2.2 The high-energy HI collisions

In the high energy domain (E/A > 100 MeV/u) the reaction mechanism is understood by the participant-spectator picture [PEI94]. In the model it is assumed that an excited and compressed region of matter is created (Fire Ball) in the overlapping zone (essentially defined by the geometry of the collision) between the target and the projectile nuclei. The reminders of projectile and target nuclei, the PLF* and the TLF*, go on following their respective classical trajectories (assumed as straight lines for simplicity), essentially as ''spectator'' of the reaction. Their velocities in the C.M. system shows typical values centred at the beam (target) velocity of Gaussian shape whose dispersion is essentially determined by the Fermi momentum of nucleon inside the projectile (target) nucleus. PLF (TLF) production cross section is determined by the geometry of the impact parameter at the instant of the collision. The parallel momentum dispersion of PLFs along with the beam axis (measured very close to 0° in the lab system) follows the characteristic behaviour of the Goldhaber parabolic law distribution [GOL74]:

$$\sigma_{par}^2(A_F) = \sigma_0^2 \frac{A_F(A_P - A_F)}{A_P - 1} \quad (1)$$

where A_P and A_F are the PLF and the detected mass fragment (A_F) numbers, respectively. The reduced dispersion value σ_0 is linked to the Fermi momentum dispersion inside nucleus, $< P_{Fermi}^2 >$. In a pure fragmentation picture of the relativistic regime, σ_0 is given by the expression $\sigma_0^2 = \frac{1}{5} < P_{Fermi}^2 >$. Experimental data show substantial agreement with the Goldhaber picture with $\sigma_0 \approx 100 MeV/c$. In these conditions nucleon-nucleon interactions take place in the Fire Ball and, due to the decreasing role of the Pauli blocking with the energy,

the excitation mechanism is substantially dominated by incoherent intra-nuclear nucleon-nucleon cascade interactions. Very large value both of excitation energy (close or even higher of the mean binding energy of nuclear matter at normal density, i.e. 8 MeV/nucleon) and nuclear density (up to 2-3 times the normal nuclear density) will be expected to be reached in the Fire Ball together with a very large production of pions [PEI94]. A typical participant-spectator is the abrasion-ablation model [BOW73, DAY86]; instead, as already pencilled above, the collisional mechanism in the Fire-Ball is understood in the frame of Intra-nuclear Cascade calculation models [CUG88]. Production of Intermediate Mass Fragments (IMF) or clusters is strongly inhibited due to the large excitation energy and entropy production into the participant zone and the decay channel is dominated by a fast vaporisation process of the total system in nucleons, pions, or other sub-nuclear particles [PEI94].

2.3 The H.I. Fermi energy domain

In the Fermi energy domain (10 MeV/nucleon < E/A< 100 MeV/nucleon) one is faced with a typical phenomenology characterised by a clear evidence of a ''transition behaviour'' in the reaction mechanism [SCO83]. In this region different observables characterising the global features of the reaction mechanisms follow a characteristic behaviour of a rapid evolution as a function of the beam energy. One of the most spectacular signature of this transition mechanism is the rapid increase of the reduced linear momentum dispersion σ_0 of projectile-like fragments produced by fast projectile (target) fragmentation reactions in semi-peripheral collisions as is observed by inspecting figure 8 of the reference [GUE85]. One observes an increase of the PLF parallel dispersion, σ_0, from values (depending on the observed PLF) close to 40 MeV/c at ~20 MeV/nucleon to the saturation value of ~ 90 MeV/c at relativistic HI energies (see figure 5 of [GUE85]). In fact at low bombarding energies, due to the important role of transfer-like reactions, phase-space constraints produce a severe reduction of the observed value of σ_0. Further improvements of the simple Goldhaber model [GOL74] have been made Bertsch and Murphy. Relevant example of such effects have been described in references [MUR84, BER81], by using different approaches. Bertsch takes in to account the effect of the Pauli principle and Murphy has considered the fact that the fragment is also a Fermi gas which puts additional phase-space constraints leading to a lowering if the reduced width σ_0. The results of these calculations are presented in figure 2, where also a dependence of σ_0 from the mass of the fragments is shown (that is also in contrast with the pure fragmentation model of Goldhaber). Another important signature of the transition mechanism is the dramatic ''rise and fall'' of fragment

multiplicity in multi-fragmentation reactions in central collisions [LYN95]. This "rise and fall" of multi-fragmentation with the increase of the violence of the collision has been observed in early experiments [OGI91] and in figure 3 we can see the same behaviour for central ^{84}Kr + ^{197}Au collisions with the Miniball/wall array as a function of beam energy [LYN95].

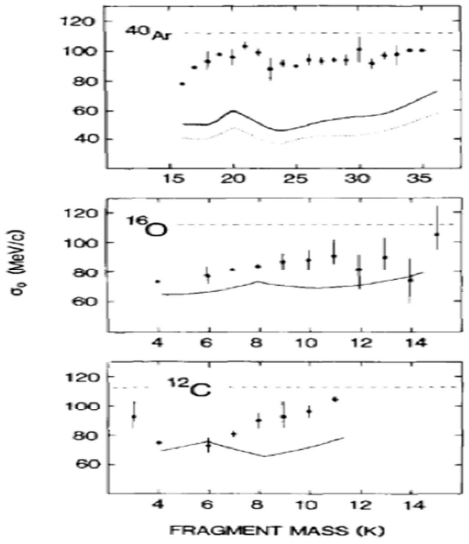

Figure 2: Reduced widths σ_0 measured for ^{40}Ar fragmentation at 213 MeV/nucl., ^{16}O fragmentation at 2100 MeV/nucl., and ^{12}C fragmentation at 1050 and 2100 MeV/nucl. The data represent the mean value and spread of σ_0 for each of the observed fragment mass K (A_F in formula 1). The dashed line is the original σ_0 prediction by the simple fragmentation model of Goldhaber (figure adapted from [MUR84]).

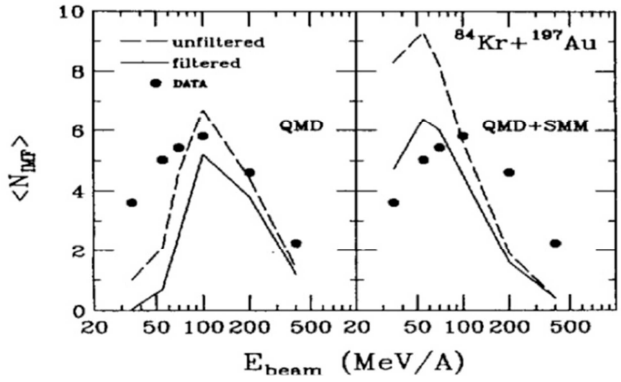

Figure 3: Mean IMF multiplicity for $^{84}Kr+^{197}Au$ collisions as a function of beam energy (figure adapted from [LYN95]).

In that experiment performed at MSU (E/A < 100 MeV/nucleon) and at GSI (E/A > 100 MeV/nucleon) with the Miniball apparatus [LYN95] we can see as the fragment multiplicity achieves its maximum at the energy close to 100 MeV/nucleon. The author compares the results with QMD and QMD+SMM models in order to explain the important role of the early dynamical phase in multi-fragmentation (QMD) in comparison with the Statistical Multi-fragmentation Model (SMS). This latter explicitly assumes a rapid disassemble of the ''composite'' nucleus after a rapid compression-expansion phase largely dominated by a transition (< 100fm/c) of the finite nuclear matter from normal baryonic density to low density ($\rho \sim 0.3\rho_0$) where the cluster are produced (freeze-out configuration). Multi-fragmentation in small clusters is supposed to take place in central collisions [DES90].

On the other hand, and in semi-peripheral collisions, several experiments already in '80 years of the last century [NAT81, MEN83; GUE83, BOR83, RAM84, RAM85] have shown that already in the 30 to 60 MeV/nucleon energy domain, the production of projectile-like fragments presents many of the features observed above 100 MeV/nucleon bombarding energies, i.e. a fragmentation of the projectile with cross sections dominated by the geometrical aspects of the reaction [WES76, GOS77, MOR78]. However, some typical low energy phenomena such as direct transfer reactions [MER85] and Deep inelastic energy dissipations [WIL76, DAY86], survive at Fermi energy. In nucleus-nucleus collisions at Fermi energies one observes phenomena characteristic of the transition from the dynamics driven by the mean field to the dynamics dominated by short mean-free path nucleon-nucleon interactions. Special attention is often paid to semi-peripheral collisions because this is the best way to study well-

localized processes taking place in the zone of contact between two colliding nuclei.

2.3.1 Semi-peripheral collisions

Since the first studies on projectile fragmentation in the 80' of the last century, the similarity with the high-energy domain was clearly evidenced [BORD90, GUE85, DAY86] together with the presence of dissipative processes very close to the ones observed in the Coulomb energy regime. As relevant case, transfer reactions that are typical mechanisms in the low-energy regime have been clearly seen. They were well evidenced and understood in the context of ''surface transfer reactions'' mechanisms [MER85]. In particular during the last two decades, several experiments have shown that at the frontier of the lower energies domain ($up \sim 40\ MeV/u$), in semi-peripheral collisions, the reaction mechanism shows essentially a binary character and the observed secondary PLFs and TLFs are the residues (after evaporation of neutrons, gamma rays and light charged particles) of a dynamical process where two or three bodies are emitted. Two of them are primary PLF and TLF products. The primary excited PLF moves forward peaked with the beam velocity, and the primary excited TLF moves slowly with a larger angular distribution in the laboratory frame of reference. Thus, in order to pin down genuine signals of the dynamical phase of the reactions responsible for the primary fragments, the statistical decay products from highly excited PLF* and TLF* have to be taken into account for a consistent description of the semi-peripheral reaction mechanism at Fermi energies. Occasionally, with properties depending on the transport properties in the nuclear medium of the nuclear symmetry term of EOS (diffusion and drift process) [SUN10] a third body is

produced and it is described in term of “neck rupture” of a residual overlap region connecting PLF and TLF in the first phase of the collision. As a result of these interactions, along with PLF, TLF and evaporated light charged particles, a new class of reaction products, the so-called ‘’Intermediate Mass Fragments’’ (IMF) with velocity close to C.M. velocity or slight higher, gradually become visible with the increase of the inelasticity of the collision. Usually, fragments with atomic number $Z \geq 3$ are classified as IMFs. However, depending on the specific studies the IMFs are indicated also in a larger range of atomic number. In this thesis, as an example, IMFs are assumed in the range, $3 \leq Z \leq 25$. Experimental evidences for abundant IMFs production not directly related to the statistical decay of PLF or TLF were accumulated in the past [MON94, TOK95, LEC95, STE95, SOB97] and with the advent of 4π arrays generations a more systematic analysis has been produced [LYN95, PAG12, LUK97, BOC00, LEF00, MIL01, MIL02, DAV02, PIA02, COLI03, DEF05, DEF05b, CAS12]. Some particularity of “non-statistical” IMFs production have been clearly establishment for semi-peripheral collisions:

- An enhancement emission is localized in mid-rapidity region, intermediate between TLF and PLF rapidity regions.
- The IMFs relative velocity distribution with respect of TLF or PLF cannot be explained in term of pure Coulomb repulsion following a statistical decay.
- Anisotropy of the IMFs angular distributions are indicating preferential emission directions and alignment tendency along with the PLF and TLF separation axis.
- For charge asymmetric systems the light particles and IMFs

emitted in the mid-rapidity region velocity are neutron richer than fragments statistically emitted from the PLF/TLF source (isospin migration).

These properties are usually referred as due to "Dynamical" or neck emission, within a time scale of the order of 100Fm/c. In summary: the interaction zone between primary PLF* and TLF* nuclei is seen as a precursor of the participant- spectator mid rapidity source, easily identified at relativistic energies, and the neck-like emission process can be viewed as a low-energy analogue of the participant zone (Fireball) during its expansion stage. Dynamical transport models strongly support the above described scenario [COL93, COL95, PAP01, PAP07].

Due to the relevance of the neck–fragmentation and dynamical emission for this PhD work, this peculiar mechanism is described with more details, with respect to the time scale and neutron enrichment associated with the process, in the following.

2.3.2 Time scale in Neck fragmentation

A detailed experimental evidence of the coexistence in semi-peripheral collisions of IMF production in a large time scale, ranging from a few fm/c up to hundreds of fm/c was given by CHIMERA collaboration [DEF05, DEF05b, RUS10, RUS14, RUS15, DEF16] by exploiting a new relative kinetic energy correlation methods [WIL05]. The evidence was based by the unique opportunity offered by the CHIMERA detection system to detect simultaneously the three biggest fragments in one event, the TLF (slow moving), PLF (fast moving) and IMF (intermediate velocity moving). As relevant example, in the following a nuclear reaction investigated with

CHIMERA in reverse kinematics, i.e., $^{124}Sn+^{64}Ni$ at E/A = 35MeV/nucleon is reported.

In figure 4 the full charge identification pattern, for ternary events observed in the reaction, is shown. Well separated class of fragments are clearly seen: projectile-like fragments (PLF) around the beam velocity (V_{beam}~8cm/ns), target-like fragments (TLF) with velocity less than 2 cm/ns, and a broad distribution of IMFs moving at intermediate velocities around the centre of mass velocity ($V_{c.m.}$~5cm/ns). Notice that at the PLF velocity, besides PLF residues with atomic number close to the projectile one (Z_{beam}=50), fragments of much smaller atomic numbers are seen in figure 4. They are fragments coming from the sequential decay of the primary PLF*.

In the case of ternary reactions where a PLF, a TLF and one massive IMF is seen in the final state (the charged particle multiplicity was constrained to a value ≤7 , in order to select peripheral collisions) important information on the mechanism can be obtained from analysis of relative velocities characterizing binary subsystems of the total three-body system.

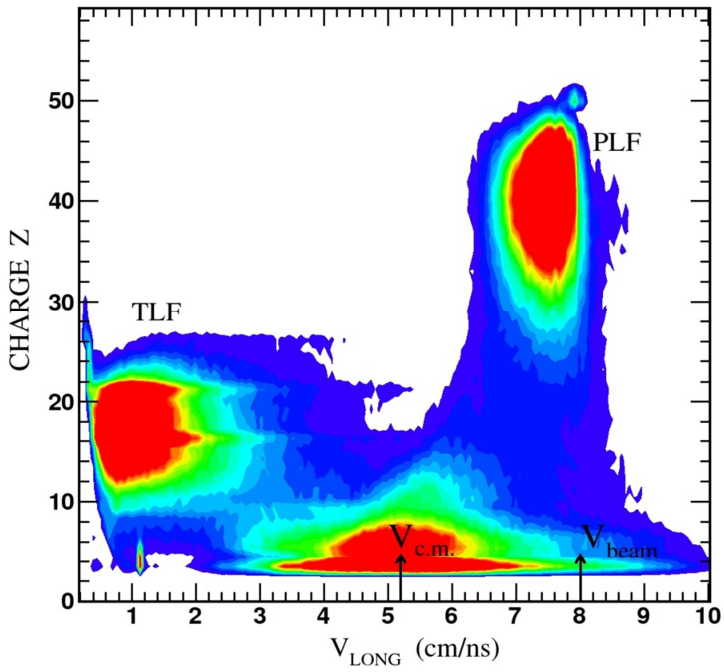

Figure 4: Charge identification as a function of parallel velocity for heavy fragments in ternary events detected in the reaction $^{124}Sn+^{64}Ni$ at E_{lab}=35MeV/nucleon. Adapted from Figure 2 of reference [DEF05].

In particular, the correlations between relative velocities of IMFs with respect to PLFs and TLFs, V_{rel} (IMF,PLF) and V_{rel}(IMF,TLF), respectively, have been considered. In figure 5 two-dimensional plot of these relative velocities for IMFs selected in the range ($4 \leq Z \leq 10$) are shown. The relative velocities V_{rel} (IMF,PLF) and V_{rel} (IMF,TLF) are normalized to the velocity V_{Viola}, corresponding to the kinetic energy of pure Coulomb repulsion for the two systems (PLF-IMF and TLF-IMF) as given by the Viola systematics [VIO85] for the asymmetric split of a given system [HIN87]. It can be readily checked that the correlation between the two relative velocities gives information on the scenario of the IMF formation, and particularly on the time when the IMF separates from PLF or TLF (or from both in the case of the instantaneous ternary split). In fact, in figure 5, it is shown the loci of points representing V_{rel}/V_{Viola} (IMF,PLF) vs. V_{rel}/V_{Viola} (IMF,TLF) correlation, calculated (full line) assuming that

the IMF separates either from the projectile (squares) or from target nucleus (circles) after a time interval of 40, 80, or 120 fm/c elapsed from the primary (binary) separation of the projectile from the target at t = 0. Details of these calculations, under the simplest assumption of one dimensional motion, are given in the appendix of reference [DEF05] and in following chapter of this thesis. Events close to the diagonal in the V_{rel}/V_{viola} (IMF,PLF) vs. V_{rel}/V_{viola} (IMF,TLF) plots in figure 5 correspond to prompt ternary divisions, whereas those approaching V_{rel}/V_{Viola} (IMF,PLF)=1 and V_{rel}/V_{Viola} (IMF,TLF)=1 values correspond to the sequential split of the primary projectile-like nucleus or the target-like nucleus, respectively. The time scale for all intermediate situations is rather short. It spans the time interval in the range 40-120 fm/c. Beyond that value, the predicted points of the V_{rel}/V_{Viola} (IMF,PLF) vs. V_{rel}/V_{Viola} (IMF,TLF) correlation move not further and are undistinguishable from much later "true" sequential decay processes (> 300 fm/c). Sensitivity of the plot to time resolution less than ~ 40 fm/c, is limited by the relative linear momentum resolving power of the used correlator (CHIMERA) due to the size of the angular opening in the detection region. However, localization of the events clearly demonstrates that at least in case of light (most probable) IMFs, the majority of them are emitted in almost prompt or "fast two-step" processes, within times of about 40–80 fm/c. Examining the correlation plots in figure 5, one can observe that generally there are more IMFs originating from the projectile breakup (upper branches) than from target breakup (lower branches). This effect originates partially from the asymmetry of the colliding system. However reduced efficiency for detection of TLFs within the angular range of the detecting system is not excluded (only the forward part of CHIMERA, angular coverage between 1 and 30 degree). The time

scale calibration discussed above was an important step in the understanding of dynamical component of the reaction of the neck-fragmentation process [WIL05]. This new kind of Wilczyński-like plot [BAR05] has been used to calibrate the time scale of IMFs emission in semi-peripheral collisions under the assumption of collinear motion of IMFs along with the PLF-TLF relative velocity direction. The analysis of the reaction $^{124}Sn + ^{64}Ni$ has shown a well-defined chronology: light IMFs ($Z < 9$), (as the example plotted in Figure 5) are emitted either on a short time scale (within 50 fm/c) with a prompt neck rupture mechanism or sequentially (>120 fm/c) after the re-separation of the binary PLF-TLF system. Heavier fragments ($Z \geq 9$) are emitted on a longer time scale (see figure 2 of chapter 3, for a more detailed discussion) and their pattern covers a time scale ranging from a fast (on the time scale of $\approx$ 300 fm/c) non-equilibrated fission-like splitting to a fully equilibrated fission process of longer time scale [RUS10, DEF05b]. These results were supported by different transport model simulations like the stochastic mean-field (SMF) [BAR05, RIZ08] and constrained molecular dynamical model (CoMD-II) [PAP07]. In chapter 3, a more detailed discussion about the separation between dynamical and statistical emission, i.e., between prompt and sequential decay will be shown. In this short introduction it is simple noticed that dynamical emission is associated with clear anisotropy of the angular distribution in the frame of the emitting source (PLF in the case of figure 6, (see below). In contrast, sequential and equilibrated emissions are associated with isotropic emission. The angular distributions are evaluated in Ref.[DEF05] by using the proximity angle ϑ_{PROX}, or its cosines, whose definition is clearly indicated in the insert of figure 6b (see below). In figure 6, and for

the reaction ^{124}Sn+^{64} Ni at 35 A MeV, the correlations between relative velocities Vrel/V_{Viola} of the three biggest fragments in an event for IMFs of charge $3 \leq Z \leq 18$ is reported in figure 6a; and the distribution of $\cos(\theta_{Prox})$ for Z = 8 (black line) and Z = 18 IMFs (red line) is reported in figure 6b. Figure 6b illustrates the observed anisotropy of the angular distribution: for $\cos(\theta_{Prox}) > 0.8$ a strong enhancement of the distribution indicates preferential emission of the fragments in a aligned configuration with the PLF-TLF: the fragment is emitted at backward angle with respect to the relative velocity vector (this latter is oriented in figure 6 from the TLF to the PLF). Notice that, assuming the condition $\cos(\theta_{Prox}) > 0.8$ (dynamical emission or aligned emission), the pattern of figure 6c is obtained: fragments are practically located on the diagonal of the relative velocity correlation plot, as expected for prompt emission (see description of figure 5). In contrast, assuming the condition $\cos(\theta_{Prox}) < 0$, i.e., fragment emitted in the forward direction (for $\theta_{Prox} > 90°$), i.e., in an angular region where anisotropy is not observed, the pattern of figure 6d is obtained: fragments are emitted with relative velocity with respect to the PLF corresponding to the Coulomb repulsion as given by Viola systematics.

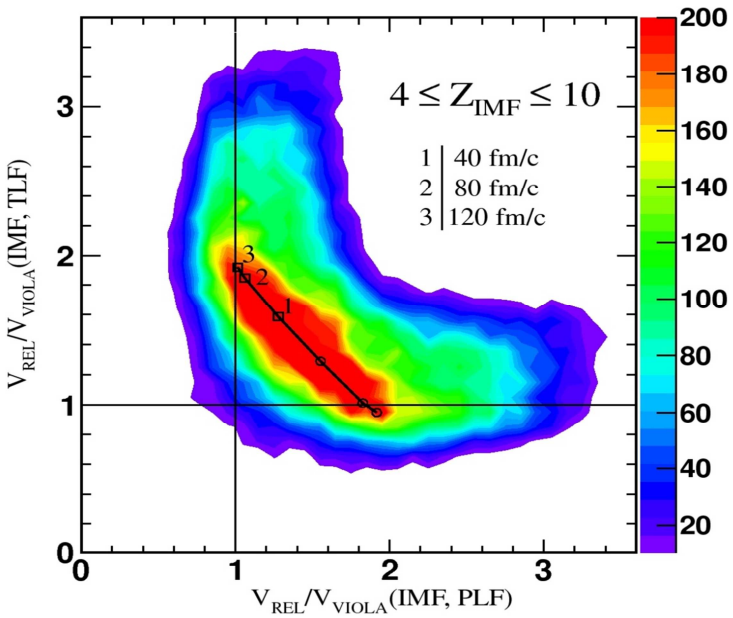

Figure 5: Relative Kinetic energy correlation for the $^{124}Sn+^{64}Ni$ at E_{lab}=35MeV/nucleon (see text for description). Values of time scale are calculated in appendix of Ref. [DEF05].

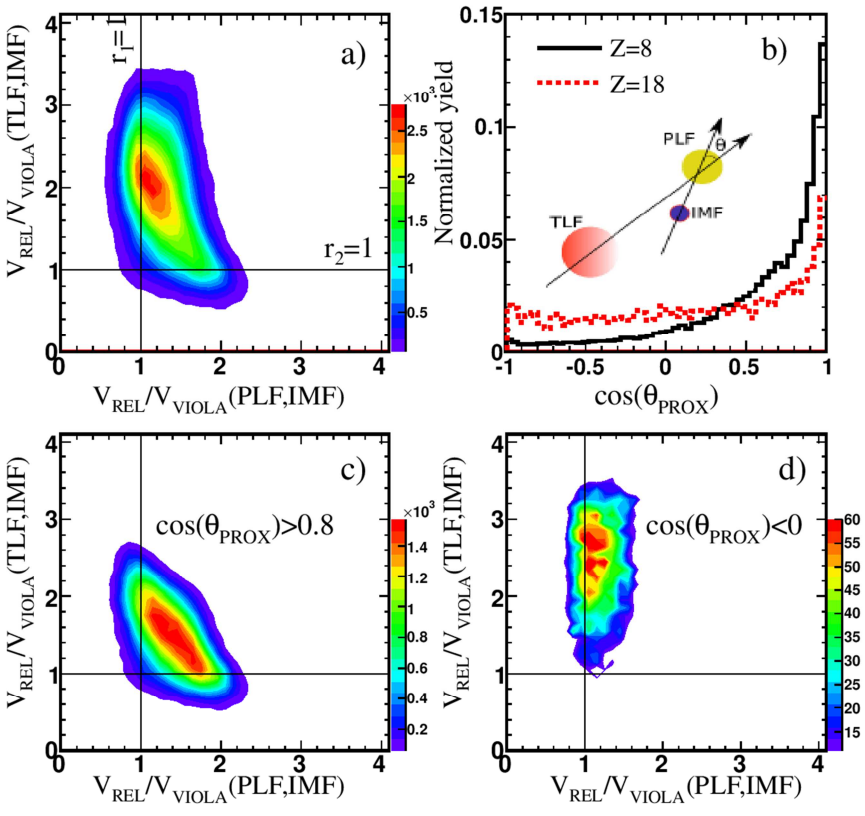

Figure 6: Dynamical and statistical evaluation adapted from [DEF14].

2.3.3 Central collisions

Central collisions in Heavy ion reactions, in particular at Fermi energy, are faced with the most violent reactions between two colliding heavy nuclei and they represent an unique way to investigate the properties of finite nuclear matter in conditions far from the ground states of the nuclei. Indeed, central collisions provide important information on the nuclear Equation Of State (EOS) [DAN01, BAR05] and have been indicated as a tool for exploring liquid-gas phase transition in finite nuclear system [POC95, HAU98, MIL98].

The most central collisions can lead to the formation of a unique source, characterized by excitation energy comparable with the average binding energy of nucleon inside the nucleus. This nuclear source of short mean life (10^{-22}s) can undergo several decay modes depending on its angular momentum, its transient density, its excitation energy.

At moderate excitation energy (< 3 MeV/nucleon) the dominant decay modes are particle evaporation leading to heavy residues, and statistical equilibrated fission [VAN73]. Some "pre-equilibrium emission" of light particles (n,p,..) is also present before full equilibrium is reached (10^{-16}s). Also, nuclear fission is relevant at low incident energy, where the projectile and target nuclei form a compound nucleus highly instable for fission into two nuclei of nearly equal mass: if the mass and charge of compound nucleus is critical for fission (compound nucleus of high facility

parameter), the spitting into two big fragments is an abundant decay channel. The two heavy nuclei produced share, according with their mass, excitation energy and undergo a complete de-excitation, following a statistical decay. The role of the intrinsic angular momentum is also important, because a high value of this quantity influences the height of the fission barrier (by lowering it, usually, due to the centrifugal component in the one body potential). At the increase of the excitation energy at value close to the binding energy, intermediate mass fragments emission takes place (as already above seen), indicating the onset of the so called multi-fragmentation [BOW93, SAN95, COR95, DAG96, POP98, BEA00].

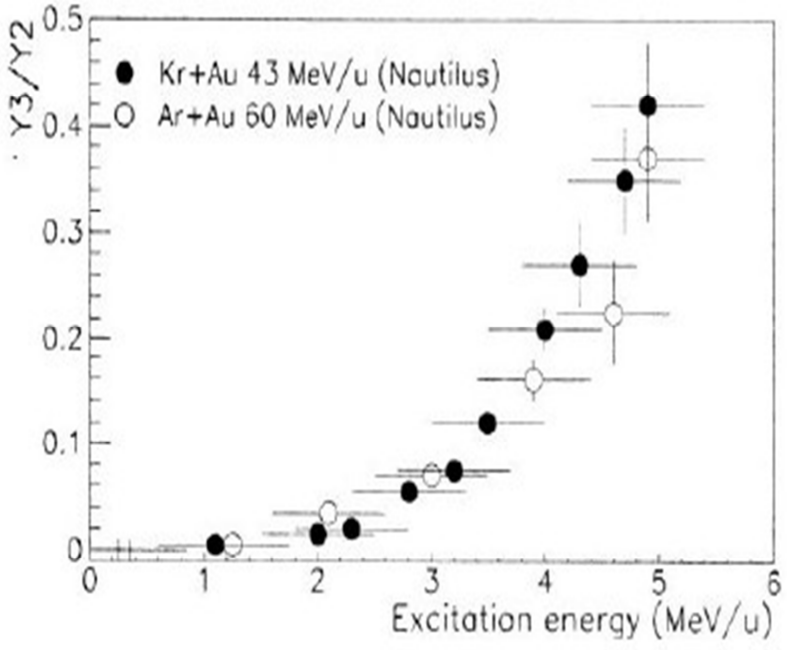

Figure 7: Evolution of the ratio between two and three body decays as function of the excitation energy of the ''composite'' system of mass in the range A = 200-220 amu from central and semi-central collisions. Adapted from [GER11].

The ratio between two body (mainly associated with fission) and three body decay (multi fragment emission, mainly associated with multi-fragmentation) is shown as function of the excitation energy in figure 7, notice that the contribution of three fragments become relevant at about excitation energy of E* ≈ 3 AMeV.

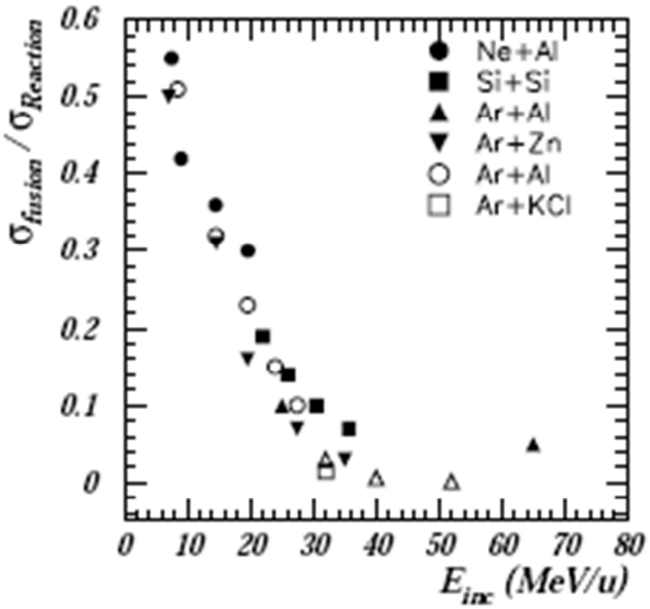

Figure 8: Evolution of the ratio of complete fusion cross section and reaction cross section as a function of the energy for six different systems [GER11].

Another important indication of the vanishing role of the compound nucleus decay is given in figure 8. In this figure, the authors (the same of the previous picture) show the ratio between the fusion cross section and the reaction cross section as a function of the incident energy for the six studied systems. The two pictures have consistently demonstrated the increasing importance of the multi-fragments emission at the increase of the incident energy end, consequently, of excitation energy.

2.3.4 Multifragmentation

Multi-fragmentation [BES88, BOW93, SAN95, COR95, DAG96, MORE97, POP98, BEA00], is the main decay channel of exited and compressed nuclear matter formed in central heavy ion collisions at Fermi energy (we have seen already some important features at the beginning of this chapter) , and it has received great attention by a large number of physicists around the word.

Beside clear signature of statistical multi-fragmentation from highly excited system, the role of the dynamics in the fragments formation is very important, as it was already evidenced from the beginning in describing the huge multiplicity of observed fragments [LYN95] by first generation 4pi detectors.

Experimental evidences

Multi-fragmentation of excited nuclei can be observed in central collisions or, alternatively, at high energy in HI collisions, as decay of spectators in semi-peripheral collisions [POC95].

In the Fermi energy regime, for very dissipative binary collisions, the outgoing PLF^* and TLF^* can be so much excited (E^* > 3-4 AMeV) to decay via multiple fragmentation emission: this process is characterized by a larger value of the cross section with respect to pure central collisions and by the presence of big residue of fragments in the mass region of the PLF and the TLF.

For central collisions, the multi-fragmentation cross section has a value of about 10-100 mbarn and even less: the fragments emission is

isotropic in the center of mass reference frame. In figure 9 it is shown the mean value of the IMFs multiplicity, as function of the periphericity (measured by b/bm, being bm the grazing impact parameter) for three different values of incident energy in the reaction Au + Au: the multi-fragmentation is favored in central collisions at about 100 AMeV (the upper part of Fermi energy regime) and in semi-peripheral collisions at higher energy.

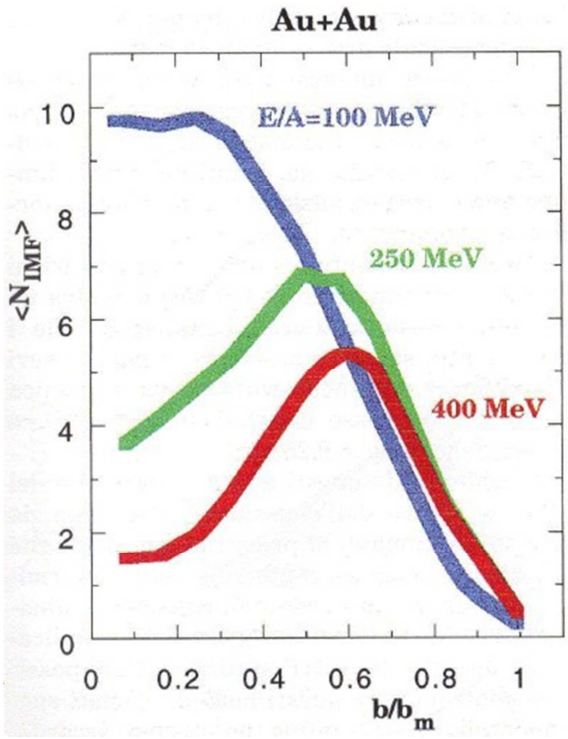

Figure 9: Mean IMFs multiplicity as a function of reduced impact parameter for four different incident energy from Aladin collaboration [GER11].

From an experimental point of view, the characteristics of multi-fragmentation can be explored measuring some useful quantities such as: the mass and the charge distributions, the dissipated energy in the collision, etc.

For both central and semi-peripheral collisions, such a IMFs production is observed as a sort of ‘’universal’’ mechanism, that is

independent of the nuclei involved. In particular, the multiplicity of fragments shows a maximum at $E^{*} \approx$ 8 -10 AMeV and then decreases, due to the beginning of the vaporization regime [BAC95, RIC01, RIV01, BON00, RIV96], i.e., the disintegration of the system in a large number of light particles (Z = 1,2) (see figure 10). This "rise and fall" of multi-fragmentation with the increase violence of the collision has been observed in experiments with both MINIBALL and ALADIN [OGI91] and, as already noticed above in the introduction, it has been evidenced for central collisions in the system ^{84}Kr + ^{197}Au collisions [LYN95].

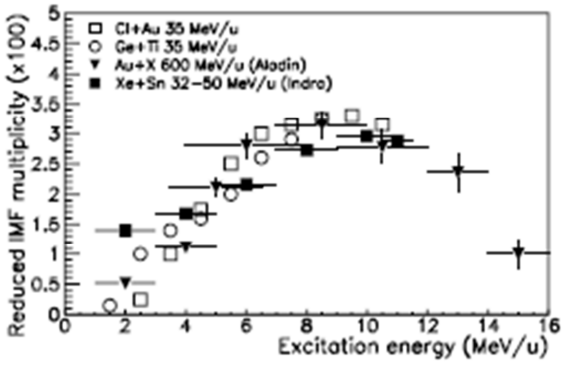

Figure 10: Rise and fall of multifragmentation (in terms of reduced IMF multiplicity vs excitation energy) as observed by Aladin and Indra collaborations [GER11].

The independence of such a mechanism on the projectile and target nuclei suggests that the system, that experiences multi-fragmentation, is thermally and chemically equilibrated. In this sense, multi-fragmentation statistical models (the most common are the Berlin model [GRO97] for a prompt multi-fragmentation and the SMM model of Copenhagen [BOND95] or the Friedmann [FRI90] one) well reproduce the experimental data assuming the system (namely the source of fragments) being in an equilibrium stage: the models consider a source at low nuclear density with respect to the saturation

density ($\rho \cong \frac{1}{3}\rho_0$) where the fragments are simultaneously produced and isotropic distributed in its volume. In this statistical framework the multi-fragmentation follows bulk instability, in contrast with mechanisms involving surface instability, such as the fragment emissions from neck region in peripheral and semi-peripheral collisions.

Several analyses carried out about the time scale related to the multi-fragmentation, by studying the velocity correlation functions (fragments interferometry) and following comparisons with theoretical simulations, show that such a process is a fast process: in particular, multi-fragmentation appears as a fast process in the early phase of the reaction, with typical associated time of about *100 fm/c* (see figure 11), comparable with time taken for the complete energy transfer and equilibration of internal degrees of freedom (and this is very important to support the equilibrium hypothesis), and an order of magnitude smaller than the time expected for the decay of the compound nucleus formed at low energies, where the fragment are sequentially emitted in a "multi-step" way.

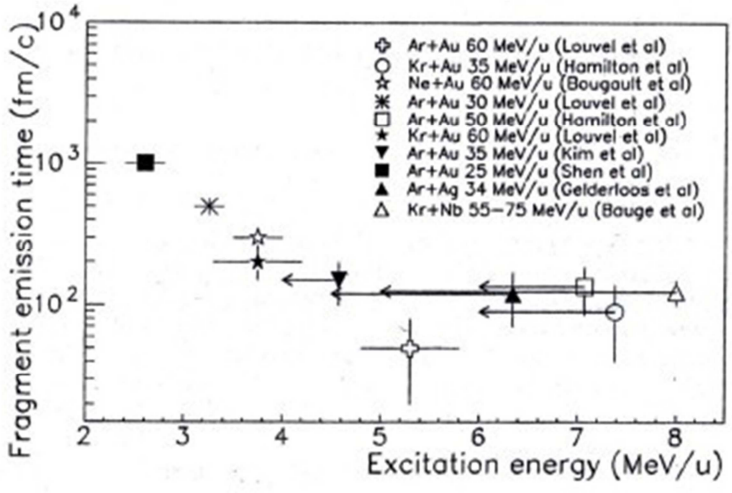

Figure 11: Fragment emission time vs. excitation energy evaluated for several systems: for E≥4-5 MeV it is possible to observe time saturation at about 100 fm/c [DUR01].*

Dynamics and thermodynamics

Usually, for a better understanding of the formation stage of such hot sources, it is useful to refer to dynamical models, which take into account several stages of the collisions from the very beginning up to the so called "freeze-out".

The similarity between effective nucleon-nucleon interaction (that shows a short range repulsive potential, and an attractive one at long range) and the Van der Waals molecular forces in fluid stimulated the research for a possible nuclear matter phase transition.

With respect to this, dynamical calculations in the framework of the transport theory predict a first stage of the nuclear collision, during about *50 fm/c*, characterized by a strong compression of the nuclear system.

In such a situation the density reaches values greater (ρ ~1-2 ρ_0) than the saturation one, consequently the system would experience an expansion, corresponding to a decreasing of the density, which brings it within the so called "coexistence region", a metastable region between a Fermi's liquid and a Boltzmann's gas phase of nuclear matter.

According to theoretical model calculations, by using mean field theory and parameterizing the nuclear interaction with the Skyrme forces, it is possible to obtain an equation of state (EOS) for infinite nuclear matter (this is an idealized matter consisting of protons and neutrons in an infinite volume where the Coulomb interactions are not present). The infinite volume implies no surface effects, so that finally

the binding energy for such a kind of matter is about 16 MeV per nucleon, that is in agreement with the first term of the nuclear mass formula. In this calculations it is predicted a critical point, at $T_C=16$ *MeV* below which (i.e. for lower values of temperatures, inside the metastable coexistence region) it is possible to distinguish a region called "spinodal region", characterized by density fluctuations. Such fluctuations can exponentially grow, so that the system would experience mechanical instabilities (negative values of the derivate of the pressure with respect to the density) that could disassemble the system in a prompt multi-fragmentation.

In particular, because of the short range of the nuclear forces and as a consequence of the quantum Heisenberg uncertainty principle such instabilities present a wave length [CHO94, CHO94b, GUA97] that favors the breaking of the system in equal size fragments [CHO08]. If the system survives to this instability, a heavy and hot source will be formed, that could de-excite statistically emitting both light particles and IMFs.

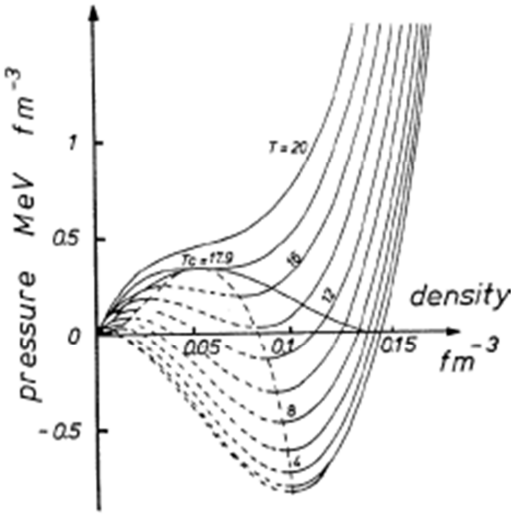

Figure 12: Isotherm curves in the pressure – density plane. In such representation the saturation point corresponds to the zero pressure point at finite density . The dashed lines correspond instead to the mechanical instabilities of the spinodal region [DUR01 and reference therein].

The situation is much more complicated when one wants to extend such concepts of equation of state, to finite nuclei: a nucleus is indeed a system with a finite number of components (nucleons) kept in a volume and, if excited, behaves as a transient hot system without an external pressure field that keeps it at values of volume and pressure fixed by the mean field.

In such a situation the definition of temperature is also delicate and it requires a strong hypothesis of thermalisation of the system: in the past decade there have been many attempts to test if a thermal equilibrium represents a reasonable approximate description of the multi-fragmenting sources [POC95, GUL97, TSA96, NAT02].

Experimentally, in searching for evidences for such a compression phase followed by an expansion one, the collective flow was a very useful observable: kinetic energy distributions for all emitted particle in several experiments have shown a contribution of collective energy that can be well reproduced assuming the existence of a common expansion velocity for all emitted fragments:

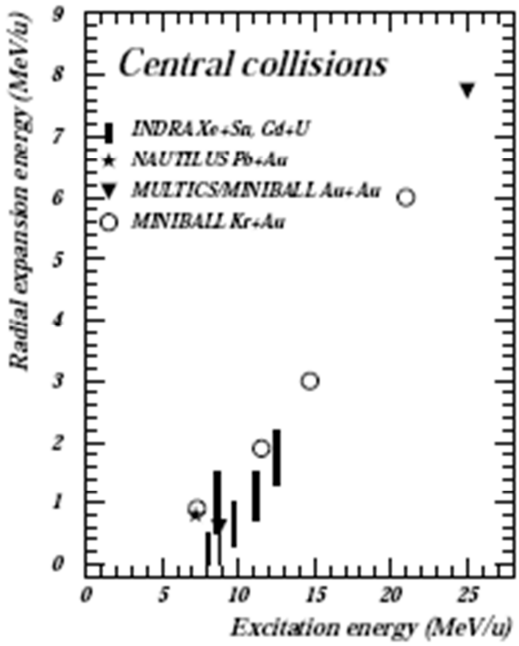

Figure 13: Systematic of the radial expansion energy as a function of excitation energy per nucleon in central collisions at Fermi energies [DUR01 and reference therein].

Since the expansion has not a favorite direction, but it's isotropic in space configuration, the radial collective flow is an important tool: this collective contribution to kinetic energy become relevant for incident energy over *30-40 AMeV*, corresponding to an excitation energy of about 5 MeV in central collisions (see figure 13) and reaches about the 30-50% of the total available energy for $E_{inc} \approx 100$ *AMeV*. The thermal contribution is very important for light particles, while the collective one is relevant for higher values of masses, so that *Ekin/A Vs A* (or *Z*) is a good variable to which one refers in order to distinguish the two components of the kinetic flow.

2.3.5 Liquid-gas phase transition

In the past decade many analyses have been performed in order to put in evidence the liquid-gas phase transition in nuclei [CHO94, CHO99, BON00].

Phase transitions are known to be related to critical behaviors and to be ruled by universal properties. In particular, at the critical point the system presents a fractal structure and so scaling laws [FIS67] should be hold: this leads for example to the famous power law shape of the fragment size distribution (figure 14) [DAG00, ELL00, CHO94, CHO99]. These critical behaviors have been identified in many nuclear reactions. The inferred critical exponents are in reasonable agreement with those expected for the liquid-gas phase transition.

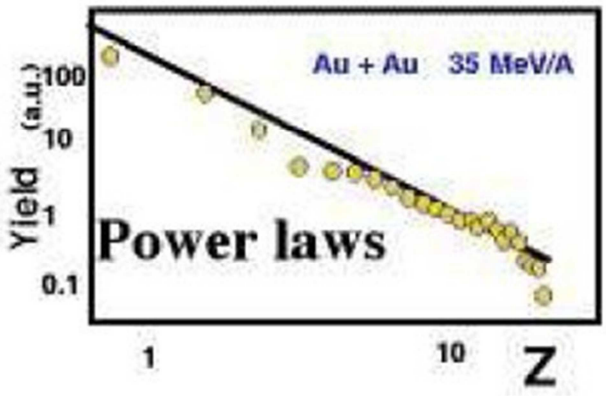

Figure 14: Typical fragment size distribution fitted by a power law. [CHO99].

The scaling is indeed based on the simple idea that a real gas of interacting particles can be considered as an ideal gas of clusters in chemical equilibrium and this can be seen as the basis of many multi-fragmentation models. In finite systems not only the fragments (gas) distribution can be studied but also the largest fragment (liquid)

distribution can be measured, and these may be considered, together with other several experimental evidences [CHO99], among the strongest signals for a liquid-gas phase transition of nuclear matter [BOT00]. Moreover, in order to get direct information about the nuclear phase diagram and the associated equation of state it is possible to define thermodynamic variables and to build, by studying their correlations, a caloric curve, usually presented as the variation of temperature as function of excitation energy (figures 15) [POC95, GUL97, MIL98, NAT02]. Indeed in the presence of a phase transition some ''plateau'' in the plane Temperature- Excitation energy is expected (see figure 15).

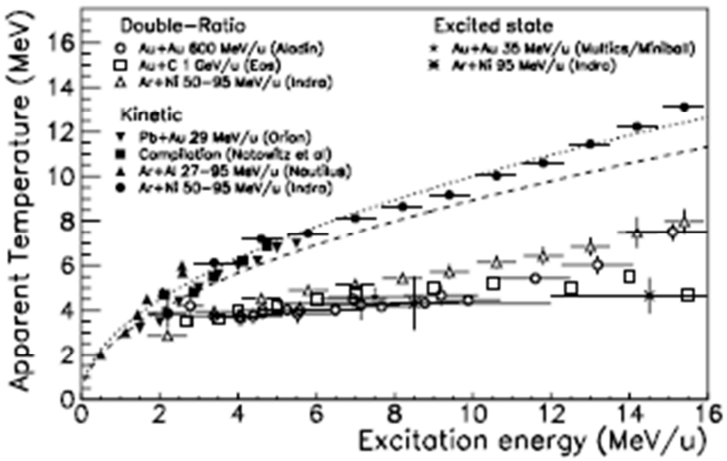

Figure 15: Systematic of measured nuclear temperatures with the three different methods briefly discussed in the following of the section [DUR01 and references therein].

The result highlighted in figure 15 evidences for a phase transition showing an almost constant temperature over a broad range of energies (“plateau”).

It has been shown that the mass of the fragmenting system has also an influence on the observed caloric curve [NAT02, NAT02b, NAT02c], i.e., the temperature of the observed plateau decreases

with such a value of mass.

Temperature measurements [ALB85, DAG00, DAG03, GER04, GER04b] (called "apparent" since they show differences among results taken from different methods) can be achieved by using different thermometers like the slope of the kinetic energy spectra ("kinetic temperature"), the ratio between excited states population ("internal temperature") and the double ratios of isotope yields ("chemical temperature").

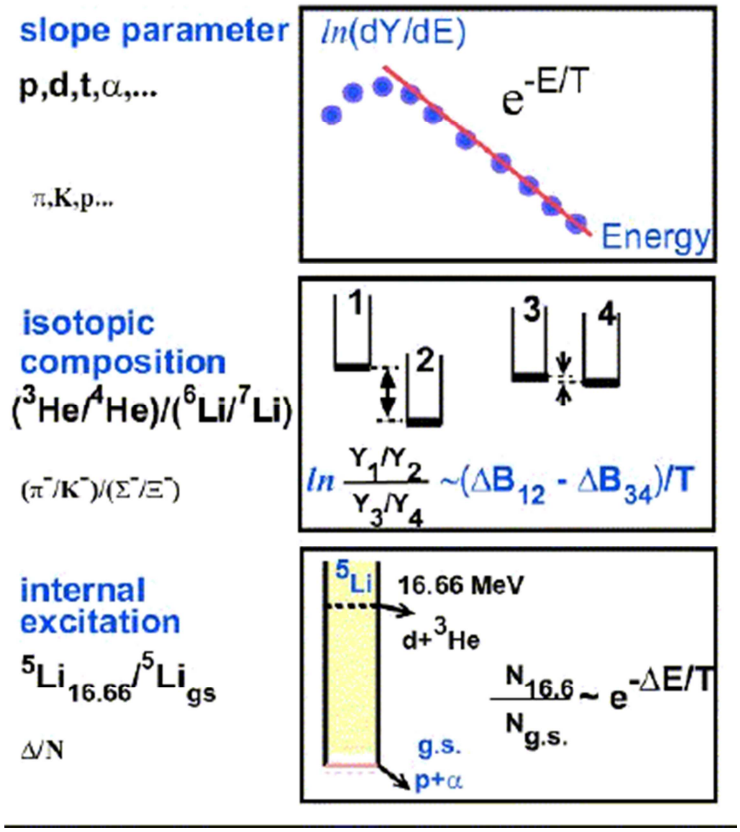

Figure 16: Schematic description of the three methods used in measuring temperature of emitting sources in nuclear collisions [GER11].

The definition of temperature for an excited nucleus is indeed not easy, first of all because of the difficulty in building a relation between temperature and excitation energy for a small system. Such a

problem, that theoretically is addressed either in terms of microcanonical or canonical approach, is experimentally overcome by looking at a collection of nuclei at the same time: in this way the cumulative effect due to the high number of observations reduces the limitations due to the small size of the primary studied system (the single emitting source). Moreover, another important issue is the fact that an excited emitting nucleus is an open system: in a statistical framework indeed it can exchange matter and energy with the outside.

From an experimental point of view, the genuine definition of the temperature is related with the probability of emission of a given particle with a precise kinetic energy. It is a ''low energy'' concept related to the density of states of the residue after evaporation, as a function of its excitation energy.

All the three above mentioned methods (see figure 16) are thus based on an experimental determination of the density of state of the decaying hot nucleus as a function of the excitation energy, differing by using several properties of emission products.

Briefly, the so called "kinetic" method is based on measuring the slope of kinetic distributions of evaporated particles and light fragments. In a first approximation the kinetic energy spectrum is addressed as a Maxwell-Boltzmann distribution, as coming from a surface sequential (evaporative) emission. An important issue in such approximation is the possibility that due to large excitation energy of the emitting system a prompt multi-fragmentation could occur. In the latter case indeed all the particles are emitted in a single step, coming from a bulk emission of the nuclear source and volume is the appropriate description.

The second method, that measures the so called “internal excitation” temperature, is instead performed by studying discrete state population ratios of selected nuclear species. It assumes that the relative probability to excite different states of a given cluster is directly linked to the density of states by means of a Boltzmann factor.

Finally, the method of double ratios of isotope yields, assuming the existence of a unique source for all used isotopes, the thermal and chemical equilibrium of such a source and the validity of the Maxwell-Boltzmann statistics for the system, has the aim to measure the temperature starting from the probability of formation of a given cluster, that depends on the chemical potential.

In the case of a hot source at density lower than the saturation one this purpose was reached by measuring the population ratio between two couples of nuclear species differing for a neutron or for a proton [ALB95].

2.4 Theory and phenomenology basics of two particle correlation in intensity interferometry scenario.

2.4.1 Historical introduction

From the historical point of view the interferometry measurement are known since the 1801 when Young with his experiment firmly established the wave nature of the light. These new waves were called electro-magnetic waves. At that time, in analogy to the mechanical waves that needs a medium into propagate through, scientists thought that should be a kind of universal medium, permeating every think and everywhere in the universe, through which massive body moves freely: it was called ether. To disprove the existence of the ether, in 1881 Michelson built a very sensitive interferometer. The history of that experiment is known [SHA55]: it was the end of the classical ether concept. Finally with the advent of quantum mechanics different experiments were performed in order to show that particles had duality and waves-like behavior. The cases mentioned above are all examples of amplitude interferometry. In amplitude interferometry the waves, as in the case of the Young experiment, or particles like electrons in quantum experiments, are emitted by a Source O and are split in two slits. The waves (or the particles) are collected in a screen where in a point D there is a detector. The probability amplitude in a given detections point D, determinate by the coordinate x and θ, is the sum of the amplitudes associated with the two paths O-S_1-D and O-S_2-D. In a Young-like experiment, performed with coherent and monochromatic waves, the light that comes from the two slits S_1 and S_2 will produce interference fringes on the point D of the screen. The brightest fringes (intensity maxima), called constructive interference, corresponding to the difference in the path $\delta = d\sin\theta$ is equal to an

even integer number of wavelength, i.e. $d\sin\theta = m\lambda\,(m = 0, \pm1, \pm2, \ldots)$. The darkest ones, called destructive interference, correspond to the difference in the path $d\sin\theta = \left(m + \frac{1}{2}\right)\lambda\,(m = 0, \pm1, \pm2, \ldots)$. If in a generic x position of the screen, it is possible to collect for an enough relatively long time the average intensity I(x) of the wave and if in the same time (called coherent time) the difference path of the two waves O-S_1-D and O-S_2-D remain constant, knowing the wavelength, it will be possible to study the fringes in order to extract information on the size of the emitting source (the separation distance d in the Fig 17, where the amplitude intensity is very simple schematized).

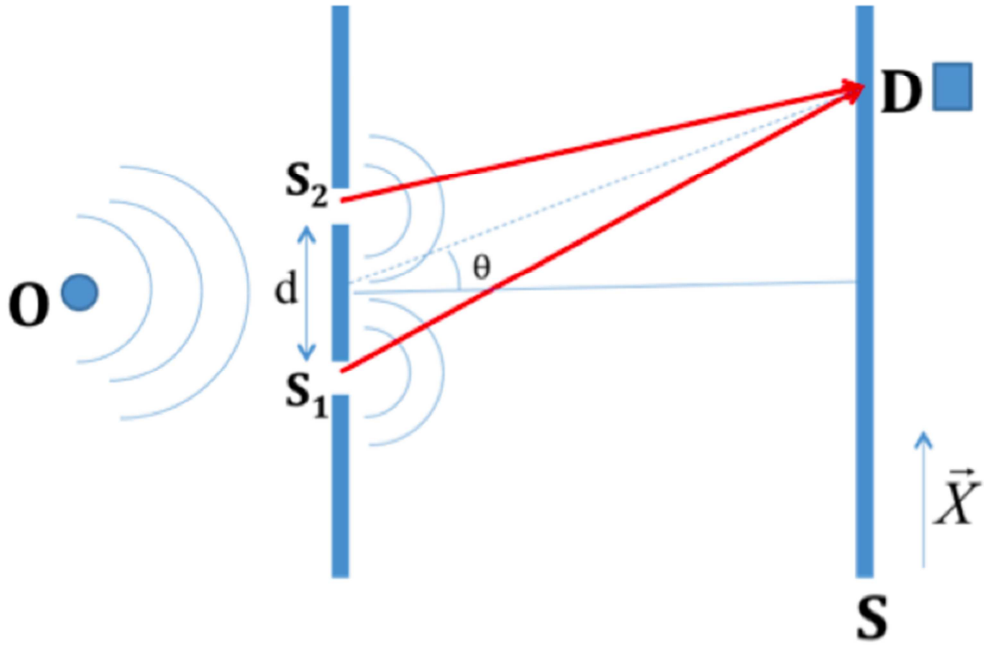

Figure 17: Schematic picture of an amplitude (Michelson) interferometer that measures the single-body detection probability [EVP12].

A so-called Michelson interferometer may be based on this principle to measure the stellar sizes. In 1920, the angular diameter of the red giant Betelgeuse in the shoulder of Orion was measured with such a technique [SWE87]. However, measurement of significantly smaller

size sources proved to be difficult with the Michelson interferometer. In fact, improving the resolving power meant the increase of the baseline until to distance of the order of 100 Km or more. More important, the line path of the waves through the terrestrial atmospheric produced relatively random phase shift, destroying the interference signal. In response to this problem Hanbury-Brown and Twiss (HBT) proposed and interferometer that operated on a different principle, see figure 18.

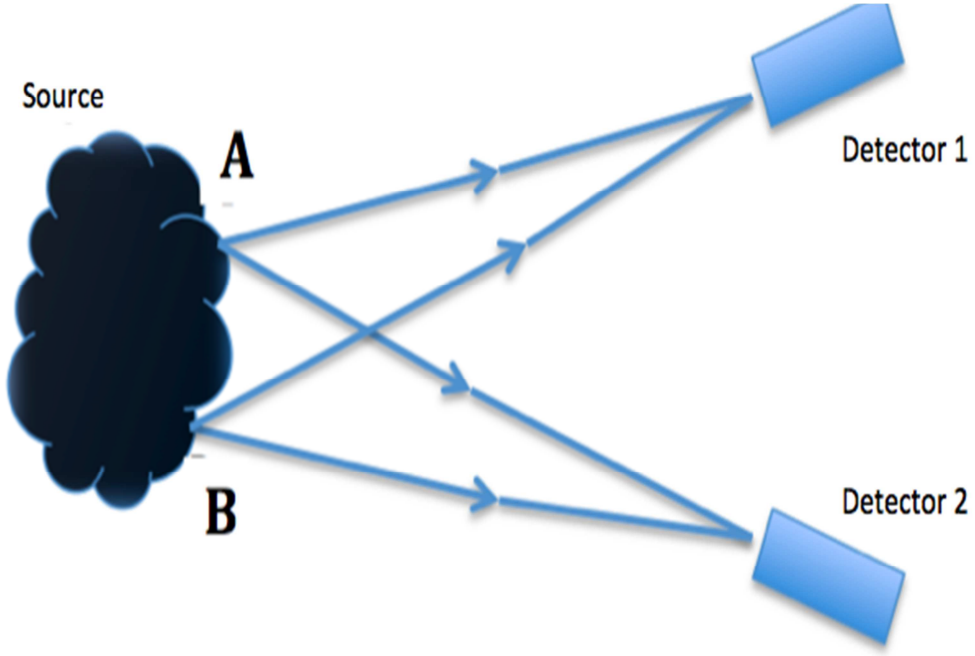

Figure 18: Schematic picture of intensity interferometer (HBT) which measures the two-particle yields [EVP12].

As opposed to the amplitude interferometer (Michelson like), which measure the single-particle detection probability, the intensity interferometer (HBT) records the two-particle probability. Information about the relative phase of wave fronts impinging on Detectors 1 and 2 is lost (and is unnecessary), but the time structure of the measurement probability at each detector is recorded. The two-particle coincidence yields $\overline{N_{12}}$and the single-particle yields $\overline{N_1}$and $\overline{N_2}$are recorder during the time ΔT.

The correlation function is constructed according to:

$$(1 + R) = C \frac{\overline{N_{12}}}{\overline{N_1} \cdot \overline{N_2}}$$

In analogy of the amplitude interferometry also in intensity interferometry (HBT) it is possible to extract source size information from the two-particle correlation. With this effect Hanbury-Brown and Twiss measured in their experiment performed between ’54 and ’56 [HBT54, HBT56a, HBT56b], the angular radius of the Sirio star. In fact for photon emitted by a source (the star in their case) measurement, such a correlation arises due to their bosonic nature. The presence of one photon in a particular momentum state increases the likelihood that another will be emitted into the same state. The strength of such correlation depends on the average space-time separation of the photon emission point that represent the source size.

2.4.2 Correlation in nuclear physics

In a nuclear physic experiment, in particular at intermediate energies, it is common to have a beam of a certain intensity I that collide on a target with a certain number of atom on square centimeters ξ and some detectors at a distance d from the target. In Fig. 19 is schematically represented this scenario with only two detectors.

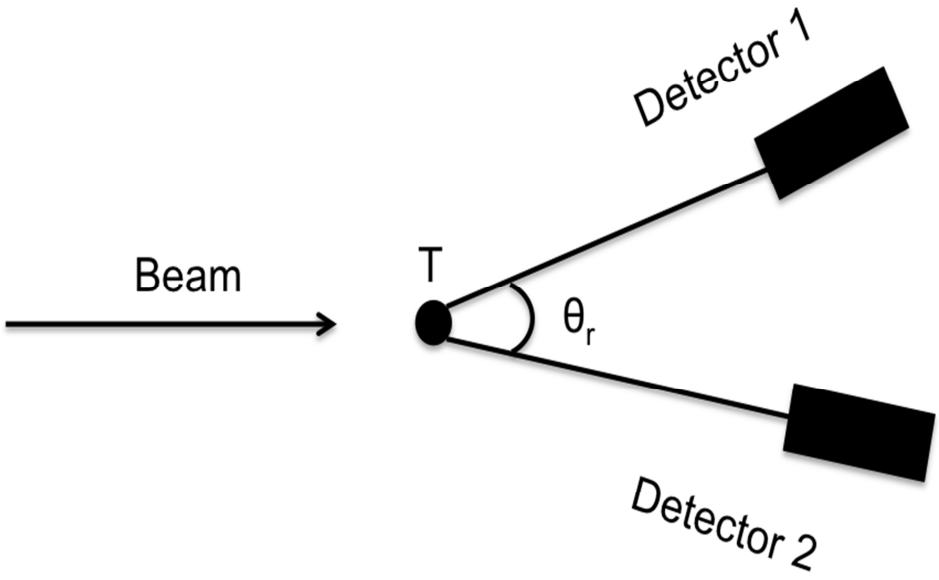

Figure19: Schematic representation of a nuclear experiment.

Classically the probability to detect the two particle in coincidence in both the detectors 1 and 2 is the cross section:

$$\frac{1}{\sigma_r}\cdot\frac{d\sigma}{d\Omega_1 d\Omega_2}=\frac{1}{\sigma_r}\cdot\frac{\overline{N_{12}}\cdot\Delta T}{\bar{I}\cdot\Delta T\cdot\xi\cdot\Delta\Omega_1\cdot\Delta\Omega_2} \quad (1)$$

where

- $\overline{N_{12}}$ is the mean number of the two particle detected in coincidence in both detectors in the time ΔT;
- σ_r is the reaction cross section;
- ΔT is the acquisition time of the experiment;

- $\bar{I}$ is the mean beam intensity;
- ξ is the atoms number on square centimeters of the target;
- $\Delta\Omega_1$ is the solid angle covered by the detector 1;
- $\Delta\Omega_2$ is the solid angle covered by the detector 2.

The cross sections to detect particles in the detector 1 and 2 (in single) are:

$$\frac{1}{\sigma_r}\cdot\frac{d\sigma}{d\Omega_1}=\frac{1}{\sigma_r}\cdot\frac{\overline{N_1}*\Delta T}{\bar{I}*\Delta T*\xi*\Delta\Omega_1}\ (2)\quad \frac{1}{\sigma_r}\cdot\frac{d\sigma}{d\Omega_2}=\frac{1}{\sigma_r}\cdot\frac{\overline{N_2}*\Delta T}{\bar{I}*\Delta T*\xi*\Delta\Omega_2}\ (3)$$

where $\overline{N_1}$ and $\overline{N_2}$ are the mean number of the particles, respectively, detected in the two detectors in the time ΔT respectively.

The relation among the equation (1), (2) and (3) is:

$$\frac{1}{\sigma_r}\cdot\frac{d\sigma}{d\Omega_1 d\Omega_2}=(1+R)\cdot\frac{1}{\sigma_r^2}\cdot\frac{d\sigma}{d\Omega_1}\cdot\frac{d\sigma}{d\Omega_2}\ (4)$$

and replacing the equation (1), (2) and (3) in to the (4):

$$\frac{1}{\sigma_r}\cdot\frac{\overline{N_{12}}*\Delta T}{\bar{I}*\Delta T*\xi*\Delta\Omega_1\Delta\Omega_2}$$
$$=(1+R)\cdot\frac{1}{\sigma_r^2}\cdot\frac{\overline{N_1}*\Delta T}{\bar{I}*\Delta T*\xi*\Delta\Omega_1}\cdot\frac{\overline{N_2}*\Delta T}{\bar{I}*\Delta T*\xi*\Delta\Omega_2}$$

and after some very simple calculations, it is obtained:

$$(1+R)=(\bar{I}\xi\sigma_r)\cdot\frac{\overline{N_{12}}}{\overline{N_1}\cdot\overline{N_2}}\ (5)$$

and putting $I\xi\sigma_r=C$ because the product $I\xi\sigma_r$ is constant we obtain:

$$(1+R)=C\frac{\overline{N_{12}}}{\overline{N_1}\cdot\overline{N_2}}\ (6)$$

that is the common correlation function.

Any observed deviation of equation (6) from the unity are due to correlation (R>0) or anti-correlation (R<0) for a given pair of particles in a given reaction.

Moving the relative distance between the two detectors θ_r it is possible to build the correlation function versus θ_r. In this case it is possible to talk about angular correlation function. It is also very common to determine the constant C of the equation (6) imposing that R(x) = 0 for reasonable values of the independent variable (i.e. considering the conservation law, etc.). These studies were performed in the beginning of the '80s [VDR81] in order to disentangle sequential ejectile decays and uncorrelated breakup processes in some nuclear reaction at the Coulomb energy.

Pioneering study of particle-particle correlation in nuclear physics started since the '50-'60s at higher energies using pions [FERMI51]. In fact a first experiment was performed to study angular correlation of pions produced in the annihilation of antiproton-proton at the energy of 1 GeV [GOL59]. These experiments performed by Goldhaber, Goldhaber, Lee e Pais (GGLP effect) [GGLP60], that were devoted to study angular distribution of pions showed that emission probability of identical pions taken in coincident was very high, is due to the bosonic nature of the pions. Figure 4 shows an example of two pions correlation function in function of relative momentum Q, measured in a more recent experiment with respect to the GGLP ones. In this case the reaction studied was Au+Au at E/A=10.8 GeV and it was performed at AGS Laboratory of Brookhaven [BARR 97].

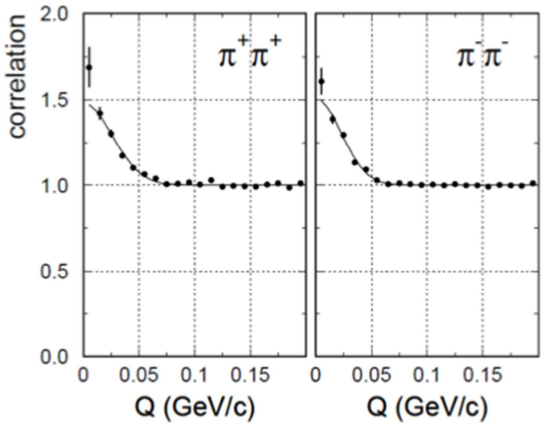

Fig. 20:Correlation function π^+-π^+ (left panel) and π^--π^- measured in Au+Au at E/A=10.8 GeV from E877 collaboration at AGS laboratory of Brookhaven [EVP12, BARR97].

The peak at small values of relative momentum (Q ≈ 0 GeV/c), as shown in figure 20, and observed also in GGLP experiment at the end of '50s, is due to the Bose-Einstein statistic where the symmetrisation of the wave function imposes that the presence of a pion in an particular momentum state increases the emission probability of another pion in the same momentum state. The intensity of this correlation depends on the space-time separation of the emission point of the two pions. In the case of figure 20 the peak's width at Q ≈ 0 is connected with the size of the emitting source. GGLP was able to estimate a source radius of the order of 5 fm. This kind of measurement stimulated a lot of work in the scientific community and later on 1973 Shuryak [SHU74] described such effect in term of "HBT effect" or "Intensity Interferometry". Of course, even if the principle of application of HBT is substantially unchanged, the physical basis of correlation among particles in nuclear physics is very different from the astrophysics case. In fact the size of a star is practically stable during the emission time, instead in the case of nuclear source there is an important time evolution of the emitting source. Furthermore the particle-particle size isn't only determined by a geometrical size but it is also sensitive to space and time of the

initial points of emission of the two particles. In fact it was soon clear that in the case of a nuclear physic source its mean life assumes an important meaning. The evolution time, for a nuclear source, is of the order of 10^{-22}-10^{-18}s, a very short time with respect to the characteristic gate time necessary (of the order of 10^{-6}s) to measure single yields and coincident yields in an experiment. Today pions correlations are very common tools to probe space-time properties of emitting source in high energy physics community and also to try to study properties of matter near to the liquid-gas phase transition studying the so called "Quark-Gluon Plasma". Experiments in the last decade were performed in Relativistic Heavy-Ion Collisions (RHIC) and Large Hadron Collider (LHC) communities [LIS05].

2.4.3 Theory and phenomenological basis of two-proton correlation function

One of the most important contributions to the theoretical formalism development of the two-particle correlation function, in particular the proton-proton correlation function, was given by Koonin in 1977. Koonin, considering that correlation between two particles, in particular π-π, was an useful tool, at relativistic high-energy, to access at space time information of the collision volume, proposed the use of proton correlations as a means of studying intermediate-energy nuclear reaction, in a similar way of the high-energy one. Koonin in its formalism [KOO77] considered two protons, which undergo simultaneous final scattering with other hadrons before leaving the system. Let, for simplicity, the two scattering sites be separated by a distance **r** and let the momenta of the protons just after being equal to **p**, and orthogonal to **r**. In the most probable spin-triplet state, the anti-symmetry of the spatial wave function induces an anti-correlation of a range of a relative p-p momenta $\Delta p \approx \hbar/r$ and hence an angular anti-correlation over an interval $\Delta\Phi \approx \hbar/rp$. An additional anti-correlation is due to the proton's mutual Coulomb repulsion, which causes them to follow divergent trajectories as they leave the system and ultimately each one imparts with a momentum orthogonal to **p** of magnitude $\sim\sqrt{me^2/r}$ where m and e are the mass and the charge of the proton, respectively. A more precise estimation of the expected small-angle p-p correlation can be obtained within the context of the non-relativistic quantum mechanics. Let D(**r**t,**p**) be the impact parameter-averaged space-time distribution of the final scattering which produces a proton of momentum **p** during an heavy-ion collision. Since it is impossible to specify simultaneously and

precisely both **p** and **r**, D can be interpreted in term of wave packets centered around these mean values. It is convenient to normalize D so that its integral over all space-time is $\sigma^{-1}\, d\sigma/d\boldsymbol{p}$ where the $d\sigma/d\boldsymbol{p}$ and $\sigma = \int d\boldsymbol{p}\, d\sigma/d\boldsymbol{p}$ are respectively the differential and the total proton inclusive cross section. Let the two protons to be emitted independently with equal momentum **p** from space-time points ($\mathbf{r}_1$,t_1) and ($\mathbf{r}_2$,t_2), where $t_2 \geq t_1$. The joint probability of observing protons with momenta $\mathbf{p}_1$ and $\mathbf{p}_2$ (both approximately equal to **p**) is then given by the square of the overlap between the single-particle wave packets centered at $(\boldsymbol{r}_1', \boldsymbol{r}_2)$ where $\boldsymbol{r}_1' = \boldsymbol{r}_1 + \boldsymbol{V}(t_2 - t_1)$, and $\boldsymbol{V} \approx \boldsymbol{p}/\boldsymbol{m} = (\boldsymbol{p}_1 + \boldsymbol{p}_2)/2m$ is the laboratory velocity of the p-p center of mass. After additional reasonable theoretical assumption, the double two proton differential inclusive cross section has been approximated as it follows:

$$\frac{1}{\sigma}\frac{d\sigma}{d\boldsymbol{p}_1 d\boldsymbol{p}_2} =$$

$$\int_{-\infty}^{+\infty} dt_1 dt_2 \int d\boldsymbol{r}_1 d\boldsymbol{r}_2 D(\boldsymbol{r}_1 t_1, \boldsymbol{p}) D(\boldsymbol{r}_2 t_2, \boldsymbol{p}) \times$$

$$\left\{\tfrac{1}{4}\left|{}^1\psi_{\boldsymbol{p}_1\boldsymbol{p}_2}(\boldsymbol{r}_1', \boldsymbol{r}_2)\right|^2 + \tfrac{3}{4}\left|{}^1\psi_{\boldsymbol{p}_1\boldsymbol{p}_2}(\boldsymbol{r}_1', \boldsymbol{r}_2)\right|^2\right\} \qquad (7)$$

The single and triplet proton-proton wave functions for protons of momenta $\mathbf{p}_1$ and $\mathbf{p}_2$ are respectively ${}^1\Psi$ and ${}^2\Psi$. They are respectively symmetric and anti-symmetric under the interchange of their spatial or momentum argument and satisfy the two-body proton-proton Schroedinger equation containing both the nuclear and Coulomb potential. In the formula (7) it is neglected the influence of the nuclear mean field on the single particle trajectories and the final state wave function. As result Ψ is the product of a plane wave in the p-p center of mass coordinate, and is φ, the wave function of the relative p-p motion (see formula 8b). This latter function depends only upon the

relative p-p momentum $\mathbf{q}=\mu\mathbf{v}_{rel}=\mu(\frac{\boldsymbol{p_1}}{m_1}-\frac{\boldsymbol{p_2}}{m_2})$ where μ is the reduced mass and $\mathbf{v}_{rel}$ is the relative velocity of the two protons at the separation distance **r**. If the masses are the same (like in the present case): $\mathbf{q}=(\frac{\boldsymbol{p}_1-\boldsymbol{p}_2}{2})$. Furthermore, as the correlation mechanism is effective only over a small region of Δ**p,** it was neglected the spatial variation in Ψ over the width of the single-particle wave packets and it was assumed that both protons have the same momentum, **p,** immediately after their final scattering. It was also taken the proton spin distribution to be statistical. In order to explore the dependence of the two-proton correlation function upon the space-time distribution of final scatterings, it is convenient to parameterize D as:

$$D(\boldsymbol{rt},\boldsymbol{p})=\frac{1}{\sigma}\frac{d\sigma}{d\boldsymbol{p}}\left(\frac{1}{\pi^{\frac{3}{2}}r_0^3}e^{-(\boldsymbol{r}-\boldsymbol{V_0}t)^2/r_0^2}\right)\left(\frac{1}{\pi^{\frac{1}{2}}\tau}e^{-\frac{t^2}{\tau^2}}\right) \quad (8)$$

where the parameter r_0 and τ are the measurements of the spatial and temporal extent of the region producing protons of momentum **p**, while $\boldsymbol{V_0}$ is the laboratory velocity of this region, taken to lie along with the beam axis. When the equation (8) is inserted in the equation (7) after some simple mathematical manipulations the double differential cross-section may be written in terms of the two-proton correlation function $R(\boldsymbol{p_1},\boldsymbol{p_2})$:

$$\frac{1}{\sigma}\frac{d\sigma}{d\boldsymbol{p}_1 d\boldsymbol{p}_2}=\left(\frac{1}{\sigma}\frac{d\sigma}{d\boldsymbol{p}}\right)^2\left(R(\boldsymbol{p_1},\boldsymbol{p_2})+1\right) \quad (8a)$$

where:

$$R(\boldsymbol{p_1},\boldsymbol{p_2})=$$

$$\frac{1}{(2\pi)^{\frac{3}{2}}r_0^2\rho}\int d\boldsymbol{r}\; e^{\{-[r^2-(\boldsymbol{r}\cdot\boldsymbol{V'}\tau/\rho)^2]/2r_0^2\}}\times\left\{\tfrac{1}{4}\left|{}^1\psi_{\Delta\boldsymbol{p}}(\boldsymbol{r})\right|^2+\tfrac{3}{4}\left|{}^3\psi_{\Delta\boldsymbol{p}}(\boldsymbol{r})\right|^2-1\right\} \quad (8b)$$

Here $\boldsymbol{V'} = V - V_0$ and the distance $\rho = \sqrt{r_0^2 + (V'\tau)^2}$ [KOO77].

Very often the theoretical two-proton correlation function is given by the so-called Koonin-Pratt (KP) integral equation [PRA84]:

$$1 + R(\boldsymbol{q}) = 1 + \int dr\, K(\boldsymbol{r}, \boldsymbol{q})\, S(\boldsymbol{r}) \quad (9)$$

in this integral equation $K(\boldsymbol{r}, \boldsymbol{q})$ is the kernel and it is basically the solution of the Schrödinger equation for the quantum proton-proton scattering that takes in to account, in the nuclear potential, only the $^1S_0$ channel, neglecting all the others. $S(\boldsymbol{r})$ is called source function and its physical interpretation gives the probability to find two protons at distance **r**, that is calculated when the second proton is emitted.

To calculate the source function two approaches have been used so far. The first is the one that assumes a Gaussian functional shape as it follow:

$$S(\boldsymbol{r}) = \frac{1}{(2\pi)^{\frac{3}{2}} r_0^3} e^{-\left(\frac{r^2}{2r_0^2}\right)} \quad (10)$$

within this approach in the literature it is possible to find many papers that made characterizations of the emitting protons source as the ones illustrated as examples in figure 21.

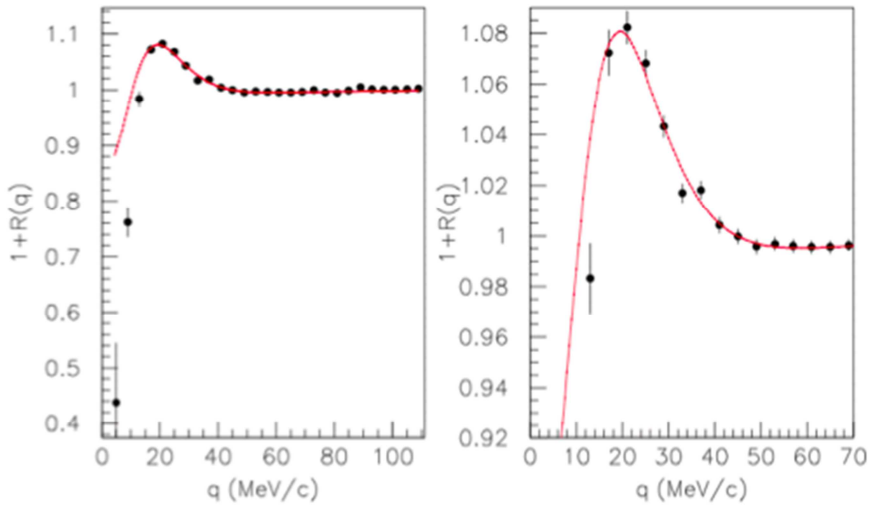

Figure 21: Space-time characterization of an emitting source using a p-p correlation function with the Gaussian approach [EVP12, EVP13, EVP13b, EVP14].

Thanks to the fit it is possible to estimate the r_0 parameter giving the spatial extension of the source.

The second approach is the so-called imaging technique [BRO97, BRO01, VER02], it consists in a numerical inversion of the KP integral equation and to evaluate the $S(\boldsymbol{r})$ without any assumption on its functional form.

In figure 22 is shown the reconstructed correlation function with the imaging technique and in figure 23 the evaluated relative source function. Of course in this latter case it isn't a size parameter to determine (like in the Gaussian fit approach) the size; so, it is common to indicate as "size of the source" the FWHM of the $S(\boldsymbol{r})$ distribution.

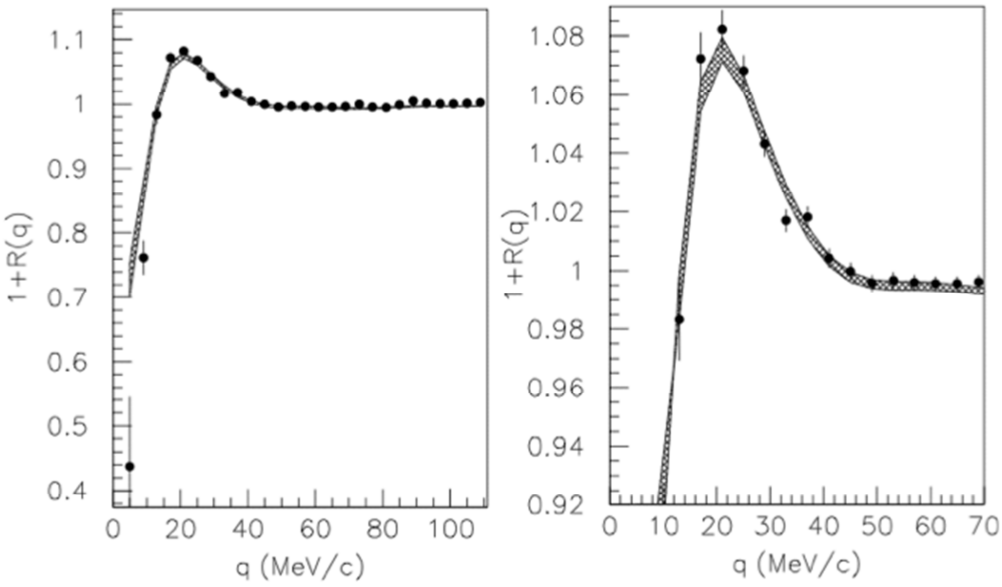

Figure 22: Imaging reconstructed p-p correlation function [EVP12, EVP13, EVP13b, EVP14].

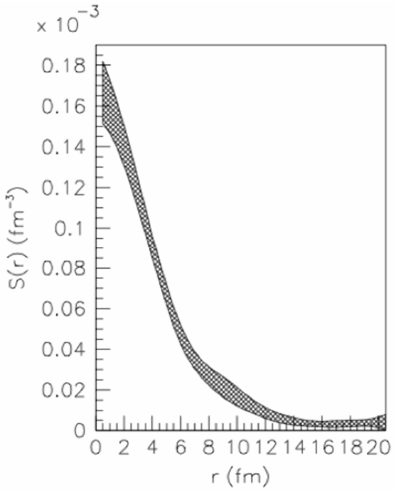

Figure 23: Imaging evaluated source function [EVP12, EVP13, EVP13b, EVP14].

For a more exhaustive description of the two techniques, refer to the reference [EVP12, EVP13, EVP13b, EVP14].

As already noticed, in the theoretical correlation function there is also a temporal component τ that is related to the half-life of the emitting source. The finite half-life τ of the emitting source leads to the so-called space-time ambiguities. Those ambiguities can be schematized using the following figure:

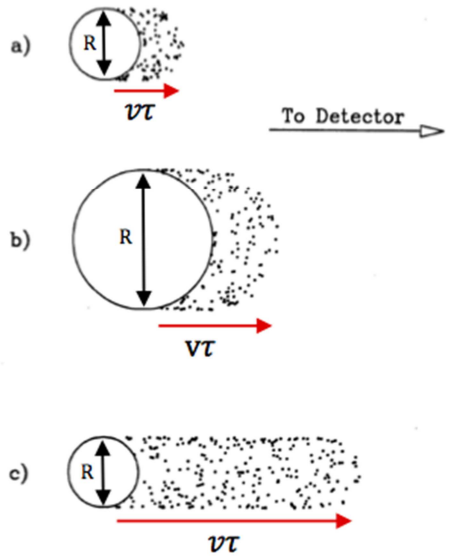

Figure 24: Finite half-time effect on the source size [EVP12].

The label a) in figure 24 is the case in which there is a small size source whit a short half-life, the case with the label b) indicates a bigger short-lived source size and in the case c) there is a small size with a very long half-life. As it is intuitive the ambiguity is related in the distinction between the case b) and the c) i.e. to separate the two cases in which there is a big size and short-lived source from the one with a small size and long-lived emitting source.

In the literature it is possible to find some works that had the purpose to eliminate this space-time ambiguity [LIS93]. Generally, the suggestions of the authors of these works were to study the "directional" proton-proton correlation function. Indeed, the correlation functions explained until now belong to the family of "angle-averaged" correlation function, and they are calculated without any constraints in the angle between the total momentum of the pairs $\mathbf{P_{tot}}$ and the relative momentum $\mathbf{q}$. In the case of the ''directional'' correlation function, the further constraint is to use only the parallel

component of the relative momentum on the total momentum $q_{\parallel} on\, P_{tot}$, or, alternatively, the transverse correlation functions is contracted by putting the constraint on the perpendicular component of the relative momentum on the total momentum $q_{\perp} on\, P_{tot}$.

The sensitivity of the directional correlation function on finite half-life and on the volume of the emitting source have stimulated interesting research activities. As an example, we can discuss some results achieved in the literature.

In figure 25, the comparison between the parallel and the transverse two-proton correlation function measured in the case of central collision in Ar + Sc reaction at the energy of 80 AMeV [LIS93, HAN94] is shown.

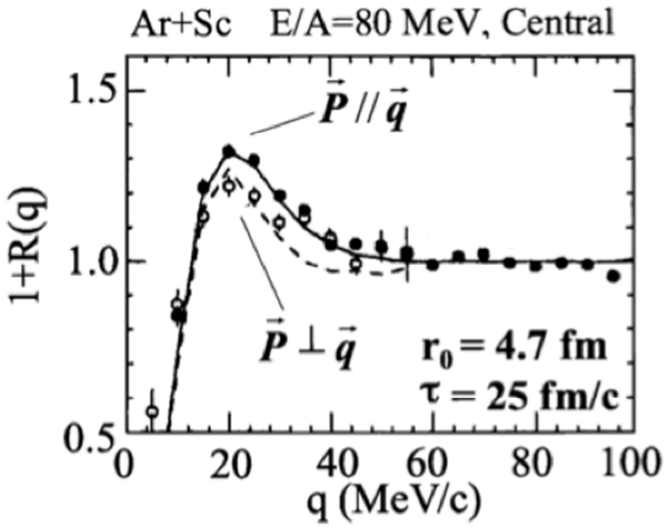

Figure 25: Directional p-p correlation functions measured in central collisions of Ar+Sc at 80 AMeV. Full circle: parallel correlation function; Open circle: transverse correlation function [LIS93, HAN94].

The full circles represent the parallel correlation function, the open ones represent the transverse correlation function. In the transverse correlation function there is a suppression of the intensity that is due to the Pauli effect. This suppression is considered by the authors as a

first experimental evidence of the effects due to the finite half-life of the emitting source.

This experimental correlation function was also studied by using the Gaussian approach with explicit half-life dependence as the following formula:

$$S(r,t) \propto e^{-\frac{r}{2r_0^2}} \cdot e^{-\frac{t}{\tau}} \quad (11)$$

The simultaneous best fit of the two correlation functions (parallel and transverse) using the source function in equation (11), estimates a source size $r_0 = 4.5 \div 4.8\ fm$ and an half-life of $\tau = 10 \div 30\ fm/c$. Both results are in good agreement with the transport model BUU that is, yet at the moment, the most reliable approach to describe the pre-equilibrium step of the reaction, having a time scale of the order of 5-100 fm/c.

2.4.4 The case of the IMF-IMF correlation function

IMF is the acronyms to indicate the Intermediate Mass Fragment, i.e. particles having atomic number Z between $3 \leq Z \leq 30$. As just seen, the study of the emission of the IMFs assumes critical importance in the dynamical evolution of a nuclear reaction, in its time scale and in the nuclear reaction mechanism.

Is the KP formula still valid in the case of IMF-IMF correlation functions?

To answer this question we have to analyze the most important assumption made in the KP approximation.

Assumption 1) the nuclear interaction, that is not explicitly considered in the KP formulation, should be negligible. This assumption implies that there are no interactions with the source after the emission and, furthermore, particles contributing to the one-particle probability propagate freely. The one-particle probability does not change with time.

Assumption 2) Galilei invariance.

Assumption 3) after the emission the two particles scatter elastically.

Assumption 4) $|q| \ll |P_{tot}|$ it means small angle between the two particles.

Assumption 5) there is no substantial correlation in the source among the particles. Then the two-particle phase-space distribution at emission separates into a product of single-particle phase-space distributions.

So fare in the treatment we are considering only identical particles. To describe a two-particle correlation function for non-identical particles in the KP formalism one must take into account the mass and charge dependence explicitly. The reference [KIM92b] presents a classical approximation to the kernel in the KP equation (9) assuming Coulomb scattering. The authors get:

$$K(\boldsymbol{r},\boldsymbol{q}) = \left|\Phi_{m_1 Z_1 m_2 Z_2(\boldsymbol{r},\boldsymbol{q})}\right|^2 \xrightarrow{class.app.} \sqrt{1 - 2\mu Z_1 Z_2 e^2/q^2 r} \quad (12)$$

With $\mu = \frac{m_1 m_2}{m_1 + m_2}$ is the reduced mass.

With this classical approximation the KP formula (9) is used also in the case of multifragmentation that occur in central HI collisions at intermediate energies. We want to discuss its validity in that case.

The derivation of the KP equation, seems, indeed, well justified for the physics case for that was originally designed for. This is, for example, the treatment of the proton emission in relativistic nuclear collisions [KOO77, PRA84, PRA87, GON91], where the particles considered are very fast, have a small charge and small relatively angle. If one goes at lower energies and heavy particles, neglecting the interaction with the source (Assumption 1) becomes incorrect. This is especially relevant for the intermediate energies where the IMFs are emitted. Assumption 5 ignores the correlation inside the source. This is also not justified for small systems like excited nuclei when the observed particles are a substantial part of the whole system.

The simple derivation of the equation (9) also implies that the source does not change during the time of the emission of the two particles. In fact Assumption 5 means in this frame that the emission of the first particles does not change the source (the assumption could be valid

for central collision for the emission at the freeze-out). There is also another assumption:

Assumption 6) the difference of the two particle emission times is small.

This assumption is also a priori not well justified for the decay of a finite hot nuclear system into intermediate mass fragments because of the presence of several nuclear mechanics that are contributing in the reactions. It is also important to note that for the case of time-dependent emission the information of relative initial distance cannot be separated from the information on emission time [SCHA94]. We can conclude that the KP formula (9) is not valid for the IMFs emission. In particular KP formulation does not satisfy the three main hypotheses:

- There is no interaction with the source after the emission;
- The interaction between particles that are not considered explicitly is negligible;
- There is no correlation in the source.

Indeed in this work we conclude that the IMF-IMF correlation function is sensitive to important physic aspects which are ignored when the KP formula is applied [SCHA94].

So how to get space-time information from the IMF-IMF correlation functions?

Concerning central collisions, in the literature, it is possible to find some works that had analyze correlation functions using the KP formula (9) using as a kernel equation (12) [KIM92, KIM92b]. According to the authors of references [KIM92, KIM92b] the classical

approximation of the KP equation (9) is in good agreements with Coulomb trajectory calculations but just in case of small IMFs having $4 \leq Z \leq 9$, emitted from an heavy system and having high kinetic energies. In intermediate energies, the scenario of the reference [KIM92, KIM92b] is consistent only with central collisions and the nuclear multifragmentation process assumed at the freeze-out configuration.

Others approaches were proposed by the authors of reference [SCHA94, SCHA94b]. They studied the behavior of the IMF-IMF correlation function as a function of the excitation energy of the emitting system. They concluded that the shape of the correlation function is certainly sensible to the space-time of the emitting source but also to the nuclear mechanism that has produced those IMFs. In that works the author used the theoretical approach of the microcanonical statistical multifragmentation model of Gross et al. [GRO90, GRO93].

Other authors, like in the case of reference [PAL95], studied the shape of the correlation function as a function of the nuclear mechanism that can produce the IMFs [PAL95] as, for examples, function of Sequential Fission (SF), Prompt Multifragmentation (MP) and Sequential Evaporation.

In this thesis work, as it follows in the next chapter, we use the theoretical frame of the Constrain Molecular Dynamic model [PAP01, PAP07] in order to estimate the time scale of the reaction in the physic case of the projectile-like dynamical fission and to try to describe the experimental data.

3. Signals of dynamical and statistical processes from IMF-IMF correlation function in the production of heavy fragments in PLF decay

Two and multi-particle correlations relevant to an intensity interferometry in a nuclear reaction at Fermi energy are useful tools in order to extract space-time information about the different emission processes [HEN12]. As it was seen in the chapter 2 using light particles, in particular protons, it is possible to obtain a kind of snapshots of the different stages of the reaction. In fact protons are particles emitted in every stage of the reaction from the pre-equilibrium to the statistical secondary decay. If the will is to access at space-time information of the Intermediate Mass Fragments (IMF) production source/mechanism, it was shown the possibility to investigate it by using the IMF-IMF correlation function method [EVP16]. The chronology of IMF emission in ternary events in non-central collision was extensively studied from CHIMERA group by using relative velocity correlations scatter plots [DEF05, WIL05, RUS10]. In particular these studies came from the analysis of the REVERSE experiment, in which two inverse kinematic reactions ^{124}Sn+^{64}Ni and ^{112}Sn+^{58}Ni, neutron rich and neutron poor respectively, both at E_{lab}(^{112,124}Sn) 35 A.MeV were studied. In this thesis work the analysis refers only to the neutron rich system.

Ternary event where defined as event with contemporary detection of 3 heavy particles (the TLF, the PLF and 1 IMF having Z≥3), satisfying conditions $Z_1+ Z_2+ Z_3>60$ and $P_{par1} + P_{par2} + P_{par3} >$

0.7 P_{proj} where P_{par} is the projection of the momentum of the particle in to the beam axis.

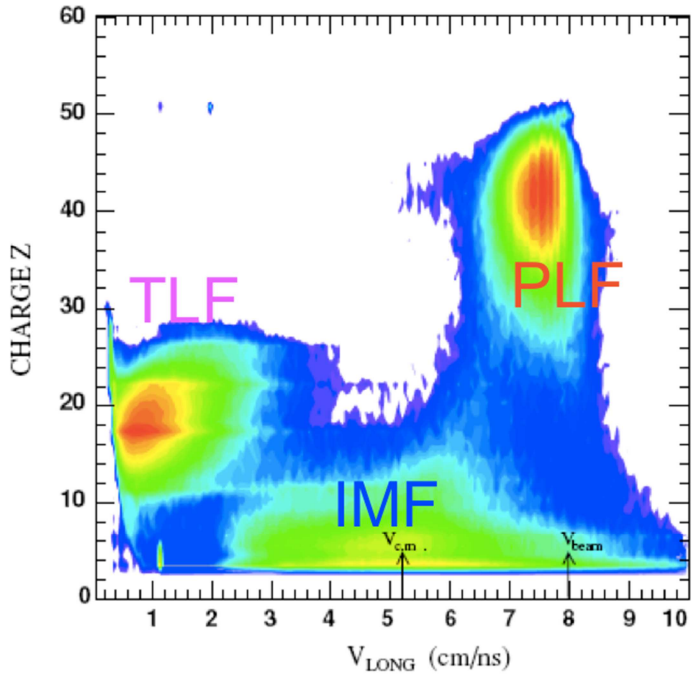

Figure 1: The charge vs the parallel velocity of the detected particles in the experiment.

In that experiment it was shown that an important cross-section, in non-central collisions, was associated with ternary reactions in which Projectile-like (PLF) and Target-like (TLF) residues were accompanied by IMFs emission. Figure 1 shows the charge of particles detected in REVERSE experiment selected for ternary events as a function of their velocity evaluated along with the beam axis in the laboratory system of reference. It is possible to distinguish slow moving Target-Like Fragments (TLFs), fast moving Projectile-Like Fragments (PLFs) and IMFs (of atomic numbers ≤ 20) located in a region between the velocity of the TLF (V < 2cm/ns) and the one of the PLF (V ~ 8cm/ns), called mid-rapidity region. Notice that in the figure light particles having atomic number 1≤Z≤2 are not reported

because in the REVERSE experiment they were not calibrated in energy.

In summary, it was shown that Light IMFs (Z≤9) are preferentially emitted in the Neck fragmentation channel at the mid-rapidity region (see chapter 2 figure 5). The interaction overlapping zone generated between the PLF* and TLF* primary fragments during the collision undergoes the most interesting dynamical evolution: in the early stage of the reaction it absorbs most of the heat generated by nucleon-nucleon collisions, and later, during the process of separation, it may evolve into a transient neck like structure located between both PLF* and TLF* nuclei.

It was shown that the IMFs are produced either in short time scales, in particular in a prompt rupture of the neck system or in longer ones, in the sequential fission-like/binary breakup decay of the PLF or the TLF [DEF05b]. Studying the isotopic composition of the IMFs emitted from neck region and by comparisons with SBNV [BAR05] models, basic transport properties in the medium of the symmetry energy of the nuclear matter (EOS) at low baryonic density, i.e., $\rho < \rho_0 \approx 0.17\ Nuc/fm^3$, have been successful pin down [DEF12]: light IMFs are formed in the the mid-rapidity diluted region, with respect to the normal PLF/TLF density and they are found to be neutron rich clusters. The symmetry energy drives neutrons to the neck region and protons to the opposite direction (isospin migration effects) and the magnitude of neutron enrichment of IMFs is strongly dependent on the slope of the symmetry energy below the saturation density.

We remind here that the equation of state of the nuclear matter (EOS) is a relation between energy, density, temperature, pressure and

isospin asymmetry ($I = \frac{N-Z}{N+Z}$) for infinite nuclear matter. For finite nuclear matter (nuclei) in its ground state (T=0), the EOS should be in agreement with the binding energy of cold nuclear matter as given by the formula of Bethe-Weizsacker or semi-empirical mass formula [WEI35]:

$$E_{Bind} = a_V A - a_S A^{2/3} - a_C \frac{z(z-1)}{A^{1/3}} - a_A \frac{(A-2Z)^2}{A} + \delta(A,Z) \quad (1)$$

where a_V is the volume's term, a_S is the surface one, a_C is the Coulomb term, a_A is the asymmetric one and $\delta(A,Z)$ is the pairing term. Their values obtained by fitting a very huge number of experimental data are respectively: 15.8 MeV, 18.3 MeV, 23.2 MeV, 0.714 MeV. For the case of the pairing term, its value depends on the number of protons and neutrons in the nucleus in such a way that, even-even: $\frac{+12}{A^{1/2}}$, odd-odd: $\frac{-12}{A^{1/2}}$, even-odd or odd-even: 0.

Evidently in a reaction the density of matter is dynamically changing during the collision and effect of both volume compression-expansion and diffusion-migration of nucleons in the medium dramatically influence the yield of the produced fragments and their isotopic composition [SUN10]. In particular, also triggered by the growing interest in exotic nuclei [CHO03], the symmetry energy of EOS in the last decade has become one of the most important objects of study and interest for the community of nuclear physicists [FUC06].

The difficulty to extract information on the EOS from HI reactions lies in the fact that the colliding system is over a large time span of the reaction out of global and even local equilibrium. At Intermediate energies the relaxation time needed to equilibrate coincides more or less with the high-density phase of the reaction (~100fm/c). The

theoretical basis for the description of the collision dynamics (practically up to 500-600 fm/c) at energies ranging from the Fermi regime up to 1-2 GeV/nucleon is the hadronic non-equilibrium quantum transport theory [BOTE90]. In practice, one applies different approximations in order to solve the complex approach in the so-called Kinetic equation. The most important are the Boltzmann-type Kinetic equations and, alternatively, the Quantum molecular Dynamics (QMD). The Boltzmann-type transport equation is known as the Boltzmann-Uehling-Uhlenbeck (BUU) Equation [BERT88]. In extreme synthesis, BUU describes the phase space evolution of the 1-particle distribution under the influence of the mean field and binary collisions. Final-State Pauli blocking is accounted. The physical ingredients entering into the model are the mean field, i.e., the nuclear EOS, and elementary cross-sections for 2-particle scattering processes. Thus, one tests the density behaviour of the EOS and the in-medium modifications of cross-sections, and so, the stopping properties of the colliding system. An alternative approach to BUU is the quantum molecular dynamics model (QMD) [AIC91, HAR98, BAS98, JAE92]. QMD is an ab-initio N-body approach which simulates HI reactions on an event-by-event basis taking fluctuations and correlations into account. The QMD equations are derived from the assumption that the N-Body wave function can be represented as the direct product of single coherent states, each one described by Gaussian wave packets (see below for details regarding the CoMD model used in this work). Generally the two-body interaction, V_{ij} , for example, can be taken from local Skyrme forces which are supplemented by empirical momentum dependence of the nucleon-nucleon optical potential.

Reaction studies, as the ones addressed in this thesis, have constrained [MDT10] the theoretical description of transport models in several aspects. As an example, neck fragmentation data, coming from different experiments and laboratories, have supported the idea that prompt emission of light IMFs is taking place from a dilute density region with respect to the normal saturation density. An important achievement in neck emission studies was the clear evidence of time hierarchy of the emission fragments as a function of the sizes. In fact as already shown in chapter two,

time scale evaluation has been accomplished in CHIMERA by studying the evolution of the relative velocity correlation plots of sub systems PLF-IMF and TLF-IMF in the case of ternary reactions. In chapter two attentions was put in the gross features of the light fragments ($4 \leq Z \leq 10$) emission. It was shown that these fragments were emitted either in a prompt time scale (~40fm/c) for the neck region or in a sequential decay at longer time scale (120fm/c) from a PLF^{*} and TLF* systems. In figure 2 relative velocity plots normalized to the Viola systematic for pure Coulomb repulsion [VIO85] similar to the one already shown in figure 5 of chapter 2., are shown for different atomic numbers in the range from Z=4 to Z=18. In figure 2 the normalised relative velocity for IMF-PLF sub system is plotted in X axis and the normalised relative velocity for the IMF-TLF subsystem is plotted in Y axis. The interpretation of the plots of figure 2 is the following (as already mentioned in chapter 2.): points close to the unity of the ratio indicates splitting of IMF either from PLF or from TLF due to pure two body Coulomb repulsion (with no influence of the third body, i.e., the target, in the case of PLF emission, or alternatively the projectile, in the case of TLF emission). This location does not indicate any deviation from the Viola systematic (pure

Coulomb repulsion, i.e., location X=1 and Y=1 in figure 2). Simple Coulomb trajectory calculations indicate that the IMF is emitted either from PLF or TLF at about 120 fm/c after the separation (t=0) of the primary PLF* from the primary TLF* or later. In contrast, for points that belong to the bisector a strong deviation from the pure Coulomb two body repulsion is noticed. It suggests that the IMF is emitted in a close and collinear configuration between TLF and PLF. In this case, the two IMFs relative velocity (respectively, the one with respect to the PLF and the one with respect to the TLF) are strongly influenced by the mutual influence of the field of both TLF and PLF and their emission time (evaluated in the same way, assuming collinear one dimensional Coulomb trajectory) is very short, i.e., a prompt neck rapture emission is observed at a time of about 40 fm/c (location 1 in the figure 2).

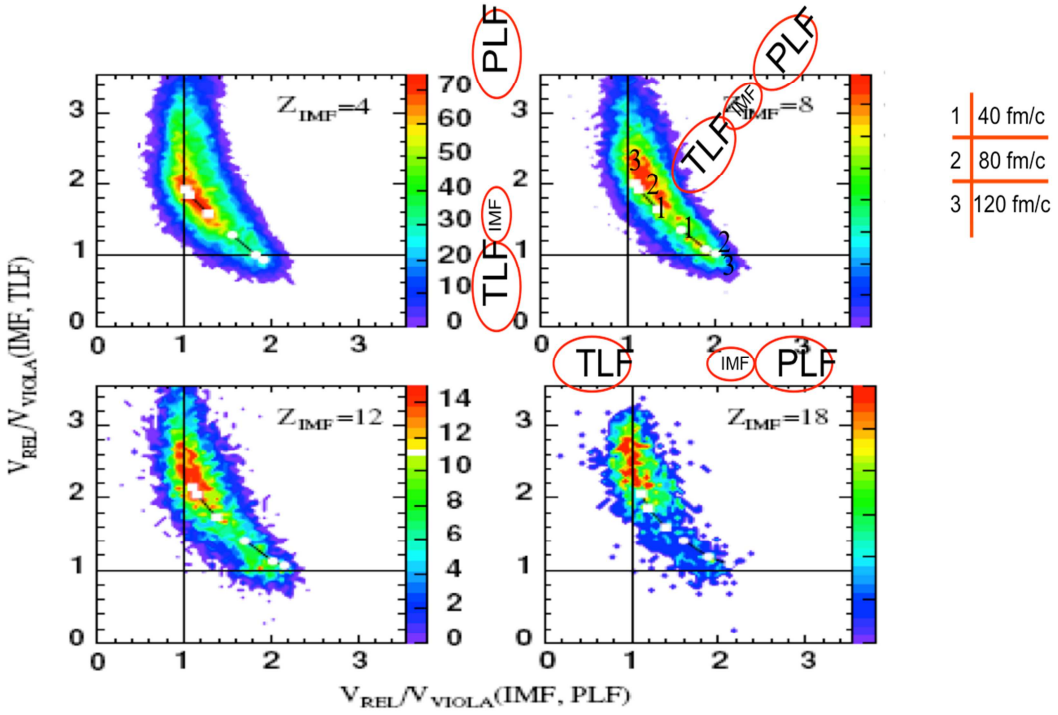

Figure 2: Correlation between the relative velocity of IMF and TLF (Y axis) and IMF and PLF (X axis) (normalized to the Viola velocity) for different charge of IMF (4, 8, 12, 18) [VIO85].

In figure 2 locations 1, 2 and 3 indicate IMFs emitted either form PLF (above first bisector) or from TLF (below first bisector) at the time of about 40, 80 and 120 fm/c.

Also, in figure 2 a clear chronology of the IMFs emission is shown as a function of their atomic numbers: with the increase of Z a clear depletion of the region located close to the diagonal of the plot is seen. With the increase of the atomic number of IMFs the pattern displays locations of the relative velocities that is progressively moving (as the Z increases) towards the unity value of the X axis, indicating emission from the PLF with negligible influence of the Coulomb field of the TLF. This picture indicates that heavy IMFs (Z>8) are emitted at later stage of the neck expansion process. This phenomenon is similar to an asymmetric mass splitting of the PLF^{*} within a time scale of ~200 fm/c after the separation (t=0) of the two primary PLF^{*} and TLF^{*} partners. The phenomenon was indicated as due to dynamical fission [RUS10] [4], in order to distinguish it from a pure sequential statistical fission decay of the PLF^{*} that appear at longer time scales (thousands of fm/c) and populates the same region of the relative velocity correlation plots.

The goal of the analysis developed in this thesis is to test and, consequently, evaluate the IMF-IMF correlation function in the physics case of both statistical and dynamical PLF splitting in two massive “heavy” fragments. In particular the basic idea is to provide a time-scale calibration of the IMF-IMF correlation function (intensity and full shape) in a specific physic case that was extensively studied by the CHIMERA apparatus that is an ideal detected to be coupled with FARCOS.

In the present analysis particles having atomic number between 3 and 25 ($3 \leq Z \leq 25$), are indicated as Intermediate Mass Fragments (IMFs). In order to study the PLF fission-like/binary breakup, we restrict the analysis to events in which the IMFs multiplicity is equal to two ($Mult_{IMFs}=2$). In agreement with previous studies [DEF05, RUS10] a constraint on IMFs velocity, requiring that both the two fragments had the parallel velocity (i.e. projection along with to the beam axis) greater than 5 cm/ns was implemented. Notice that the centre of mass velocity of the investigated system $^{124}Sn+^{64}Ni$ at 35 AMeV in the laboratory frame is equal to $V_{CM}=5.16$ cm/ns and the one of the projectile is equal to $V_{Proj}=8$ cm/ns.

As it is common in the CHIMERA multi-detector analysis, almost PLF complete events are characterized by a total detected parallel momentum larger than 60% of the projectile one and a total detected charge, Z_{tot}, for each event, larger than 40. These constraints let us to assume that the PLF is almost completely detected.

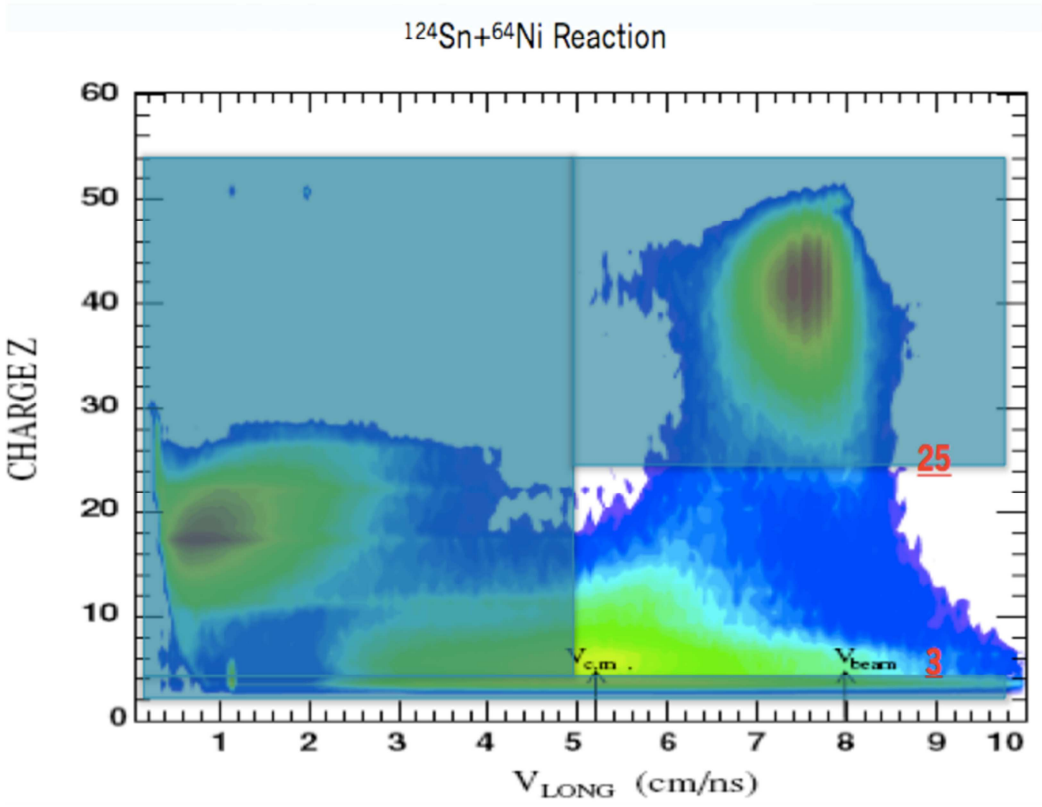

Figure 3: Charge vs parallel (to the beam axis) velocity for all charged particles detected in the experiment; the particles of interest in this analysis (see text) are those in the not hatched region [EVP16].

In figure 3, the detected atomic number of the particles vs parallel (along to the beam axis) velocity is shown for complete ternary events. The particles of interest of this analysis (see text) are located in the not hatched region of the figure 3.

In order to characterize the space and time properties of the IMF-IMF correlation function the selected set of IMFs was decomposed in other three sets as functions of the charge asymmetry (Z_{Asy}) of the two IMFs. The asymmetry variable is defined by the ratio $Z_{Asy} = \frac{Z_H}{Z_L}$ where Z_H and Z_L are the atomic number of the heavy IMF and the light one, respectively. The three sub-set are respectively labelled by: $1 \leq Z_{Asy} \leq 2$, $2 < Z_{Asy} \leq 4$ and $Z_{Asy} > 4$. In other to select IMFs

emitted from a PLF source an additional constrain was inserted in the sum of the atomic number of the two IMFs, such as: $25 \leq Z_H + Z_L \leq 50$. With these basic constraints, the analysis in correlation function was performed.

The experimental correlation function is defined by the formula (1), in case of the reduced relative velocity variable (see below):

$$1 + R(\boldsymbol{V}_{red}) = C_{12} \cdot \frac{Y_{coinc(\boldsymbol{V}_{red})}}{Y_{uncor(\boldsymbol{V}_{red})}} \qquad (1)$$

Basically, formula (1) gives the ratio between collected pairs of IMFs in coincidence in the same event and the uncorrelated ones. The denominator $Y_{uncor}(\boldsymbol{V}_{red})$ is evaluated with the event mixing technique [LIS91]. This latter technique consists into taking into account two particles, in this case two IMFs, coming from two different events and to evaluate the $\mathbf{V_{red}}$ variable of interest paying attention to take into account different events of the reaction (i.e., uncorrelated for definition) that satisfy the same global conditions of the numerator Y_{coinc} (V_{red}) true coincidences, i. e., having the same total charged particle multiplicity, the same reaction plane, the same total atomic number of particles, etc.

For the purpose of the present work the IMF-IMF correlation function was evaluated as function of the reduced velocity $\boldsymbol{V}_{red}$ (see eq.2) in order to increase the statistical significance of the analysis by adding together couples of particles having different atomic number [KIM92]:

$$\boldsymbol{V}_{red} = \frac{\boldsymbol{V}_1 - \boldsymbol{V}_2}{\sqrt{Z_1 + Z_2}} \qquad (2)$$

In the Figure 4 the three IMF-IMF correlation functions in the three different Z_{Asy} gated are shown. The variable $\boldsymbol{V}_{red}$ values is given in 10^{-3} c units.

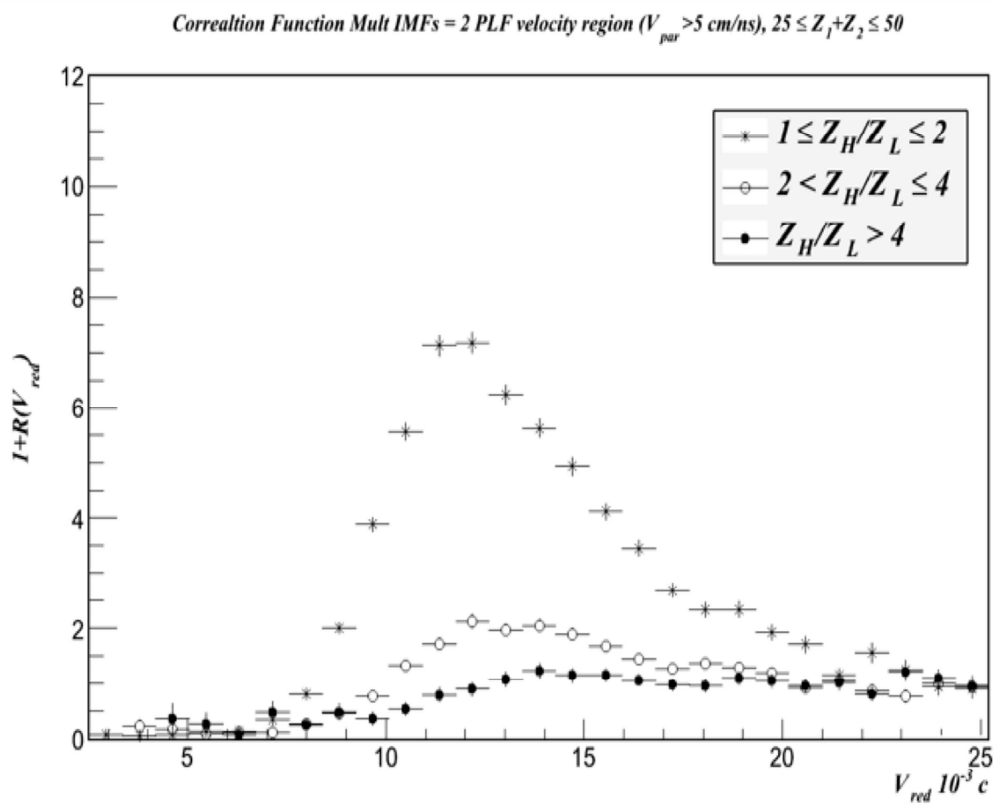

Figure 4: IMF-IMF correlation function for $25 \leq Z_H + Z_L \leq 50$ gated by different Z_{Asy} [EVP16].

The three IMF-IMF correlation functions, for the three ranges of charge asymmetry show very different shapes. It is possible to distinguish different parts in the shape of the correlation functions. In the first part, within about $\boldsymbol{V}_{red} < 7 \cdot 10^{-3}c$, a strong anti-correlation (suppression effect) due to the Coulomb repulsion between the two IMFs is clearly noticed: the space-time configurations of the two outgoing coincident IMFs are not allowed for so small reduced velocity. For value of $\boldsymbol{V}_{red} > 7 \cdot 10^{-3}c$ the correlation signal of the three correlation functions shows a steady increase up to a maximum

whose value depends on the asymmetry. It is worth to notice that the well-defined bump observed for $1 \leq Z_{Asy} \leq 2$ is centered at a value of reduced relative velocity corresponding to a binary spitting, which is in agreement with the Viola systematics for fission decay [VIO85]. The width of this latter distribution is about $5 \cdot 10^{-3}c$ and it displays an asymmetric tail extending to a reduced velocity of about $20 \cdot 10^{-3}c$. In the $2 < Z_{Asy} \leq 4$ asymmetry range it is possible also to observe an asymmetric correlation bump extending in the range of values $7 < \boldsymbol{V}_{red} < 17 \cdot 10^{-3}c$ of relative velocity. In the case of the last range of the asymmetry no correlation bump is observed and the correlation signals saturate to the unity at about $\boldsymbol{V}_{red} \approx 14 \cdot 10^{-3}c$. Of course, the correlation functions for the three asymmetries saturate to a flat shape after $\boldsymbol{V}_{red} \approx 22 \cdot 10^{-3}c$. For this reason the range between $22 < \boldsymbol{V}_{red} < 24 \cdot 10^{-3}c$ was chosen as the proper range for the normalization (see coefficient C_{12} in formula 1.) to the unity for the three range of the asymmetry variable.

The question is why we observe this large and impressive difference of the correlation function in the three regions of the Z_{Asy}?

As we expect from previous studies, the correlation function provides information on the space configuration of the emitting process and on its time scale. So, what is the origin of these changes in the intensity and shapes?

Is the size of the emitting source responsible of these changes, or is the different timescale of the reaction mechanisms of the emitted fragments? Or both of them are contributing?

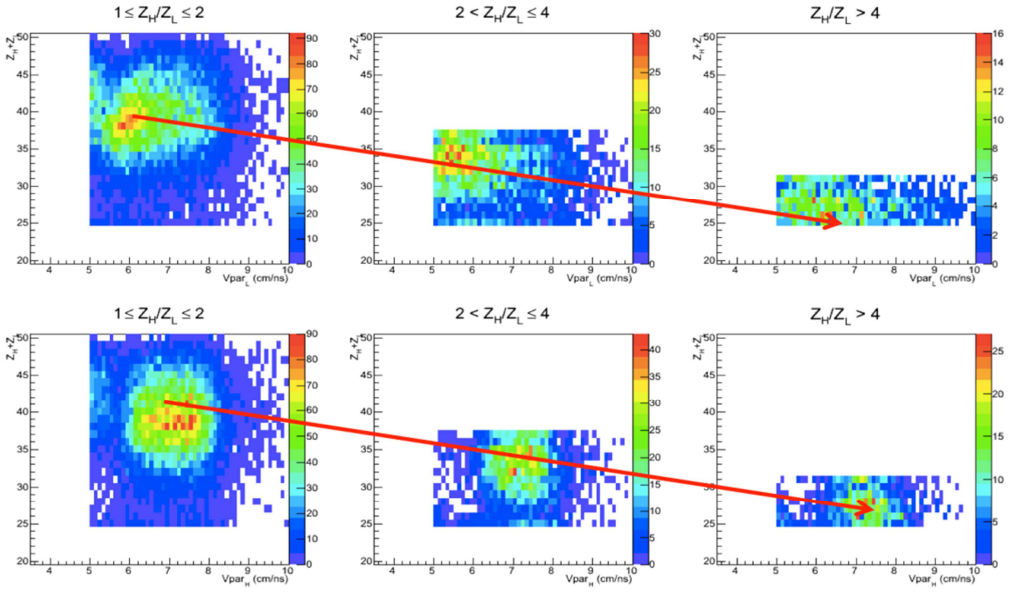

Figure 5: $Z_H + Z_L$ as a function of both the parallel velocity of the light IMF (top panel) and the parallel velocity of the heavy one (bottom panel) in the three ranges of Z_{Asy} ($25 \leq Z_H+Z_L \leq 50$) [EVP16].

To understand better the origin of the IMFs involved in the three regions of charge asymmetry, we investigated their total charges as a function of the parallel velocity of the two correlated IMFs. The figure 5 shows the sum of $Z_H + Z_L$ (the charge of the heavy IMF and the light one) as a function of the parallel velocity of the light IMF (top panel), and of the heavy one (bottom panel). The figure 5 clearly shows the tendency of the sum $Z_H + Z_L$ to steady decreases with the increase of the charge asymmetry of the two IMFs, indicating an increasing of the energy dissipation by increasing the charge asymmetry Assuming that the sum $Z_H + Z_L$ is an indication of the size of the emitting system, it is argued that the shape evolution of the correlation functions shown in figure 4 is very poorly constrained with respect to both dissipation and size of the sources. In fact a clearly indication on the energy dissipation window in the three ranges of Z_{Asy} could be observed by inspecting the figure 6 (left panel) where

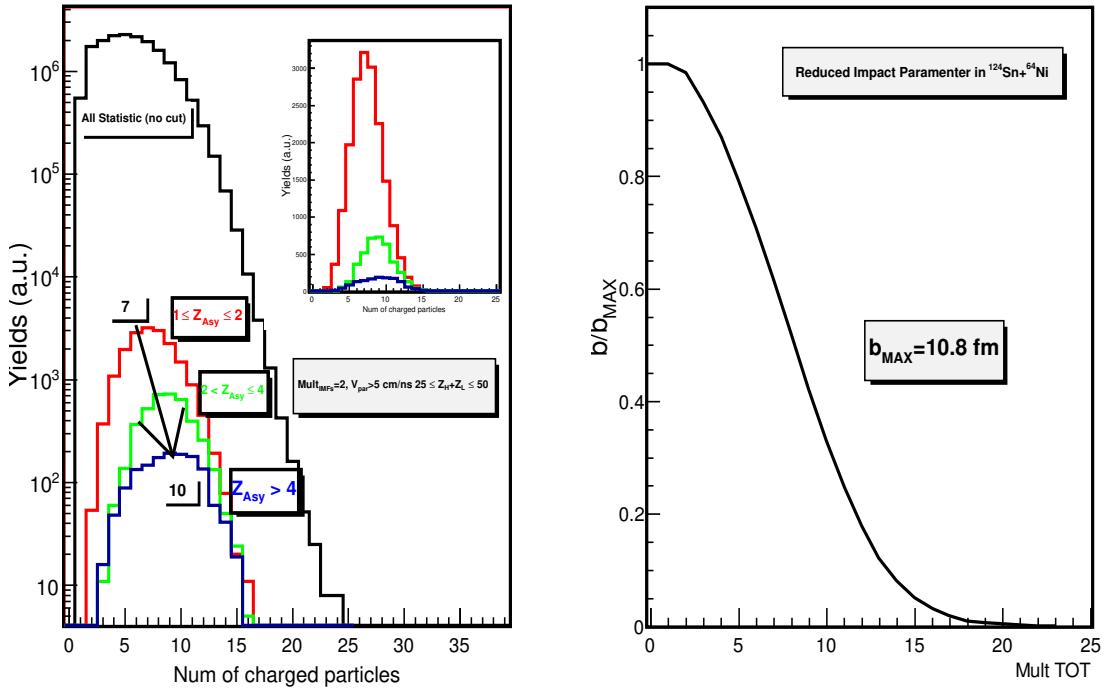

Figure 6: Left. Total charged particles multiplicity (black line) and IMFs multiplicity for the three range of Z_{Asy}. In the top-right figure the same spectrum in linear scale to empathize the cross section differences. Right. The reduced impact parameter estimation according to Cavata method [CAV90].

the total charged particles multiplicity distribution (i.e. light particles and fragments) detected in the experiment (black line) and the same distribution in the case of $Mult_{IMFs}$=2, and with velocity greater than 5 cm/ns is reported. The latter is shown for the three cases: $1 \leq Z_{Asy} \leq 2$ red line, $2 < Z_{Asy} \leq 4$ green line and $Z_{Asy} > 4$ blue line. Also in the Figure 6 (right panel), the reduced impact parameter of the collision as a function of the total charged particles multiplicity, as it is evaluated according to the Cavata method [CAV90, DEF14] is shown. As it is clear from the Figure 6, in the case of the most symmetric value $1 \leq Z_{Asy} \leq 2$ the mean value of the total charged value multiplicity is about 7 and the value increases up to 10 for the most asymmetric set of IMFs pairs. This observation suggests that the violence of the collision, and, consequently the energy dissipation

window, increases by increasing the charge asymmetry of the two IMFs. It is argued that, in the most symmetric case, we are faced with gentle peripheral collisions located at large impact parameters, and consequently, the overlapping zone between projectile and target is much smaller than in the case of the asymmetric splitting that is associated with more violent collisions located at smaller impact parameters. In this dissipative reaction a mid-rapidity region is generated by a substantially large overlapping zone between projectile and target.

Evidently, the strong differences observed in the Figure 4 are due either to effects related to the reducing size of the emitting system and to the different time scales occurring in the three ranges of asymmetry.

So, in order to achieve a more careful understanding of the different shapes observed as a function of the asymmetry, it is important to compare the correlation functions by additional constrains on the size of the emitting system by constraining the range of the energy dissipation. Consequently, we have considered two complementary narrow bins of the sum $Z_H + Z_L$, i.e., one bin was defined according to the range $25 \leq Z_H + Z_L \leq 35$ and the other one with $35 \leq Z_H + Z_L \leq 50$. The goal is to fix the same dissipative window in each of the two subsets of the sum $Z_H + Z_L$(and consequently to consider the size of the emitting system fixed within the subset). The figure 7 shows the dissipative window, in term of the total charged particles multiplicity, in each one of the two bins of sum $Z_H + Z_L$. A sizeable difference (about 3 charged particles) in the average multiplicity between the two sub-set is observed. Assuming as a crude approximation, that the particle multiplicity is a reasonable indicator of the energy dissipation, Figure 7 indicates that the three charge asymmetries ($1 \leq Z_{Asy} \leq 2$,

$2 < Z_{Asy} \leq 4$ and $Z_{Asy} > 4$) associated to a given value of $Z_H + Z_L$ (i.e., separately of each one) experience quite similar energy dissipation.

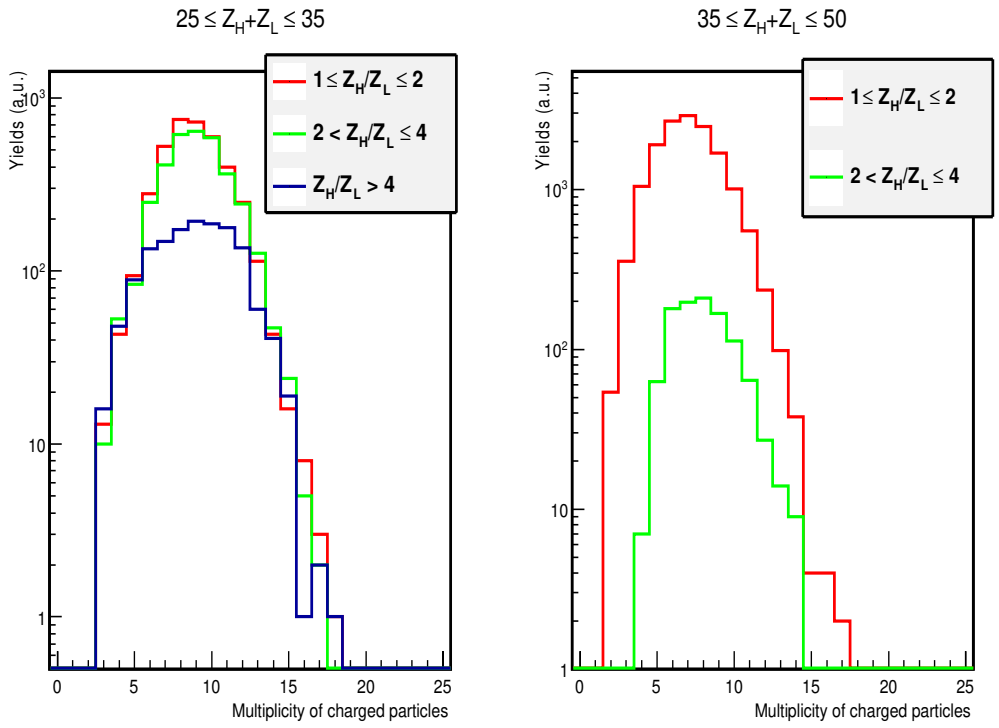

Figure 7: Total charged multiplicity for different $Z_{Asy,}$ selected ranges are $25 \leq Z_H + Z_L \leq 35$ (left panel) and $35 \leq Z_H + Z_L \leq 50$ (right panel) [EVP16].

Describing the Figure 7 in more details, and remembering the constraints used, that are, the $Mult_{IMF}$=2 and both IMFs having parallel velocity greater than 5 cm/ns (from PLF velocity region), it is possible to observe that (left panel) the total charged particles multiplicity in the three ranges of asymmetry for $25 \leq Z_H + Z_L \leq 35$ assumes nearly the same distribution with similar shapes and the same maximum around the value of 10. Practically, it is possible to observe the same in the case of $35 \leq Z_H + Z_L \leq 50$(right panel). In this case the maximum around a value of 7 indicates less dissipation in the

reaction channel. However, in this range of sizes, large values of asymmetry ($Z_{Asy} \geq 4$) are inhibited by charge conservation effects due to the constraint of the bigger size as it is required by the condition $35 \leq Z_H + Z_L \leq 50$. So we can conclude that when the sum is between $25 \leq Z_H + Z_L \leq 35$ we observe the greater dissipation but it is the same, for the three range of the charge asymmetry. In summary, it is argued that, in the case of the bin in which the sum of the charge of the two IMFs is between $35 \leq Z_H + Z_L \leq 50$ there is less dissipation, which means more peripheral events, but, also in this case, there is the same dissipation in both the two ranges of $Z_{Asy.}$ In term of size we are allowed to say that in the two bins of total charge, two different sizes of emitting source are selected (with a broad distribution that is linked to the total multiplicity spectrum).

This is also confirmed by inspecting Figure 8 and 9 that show the sum of $Z_H + Z_L$ as a function of the parallel velocity of the light IMF in the top panel, and of the heavy one in the bottom panel.

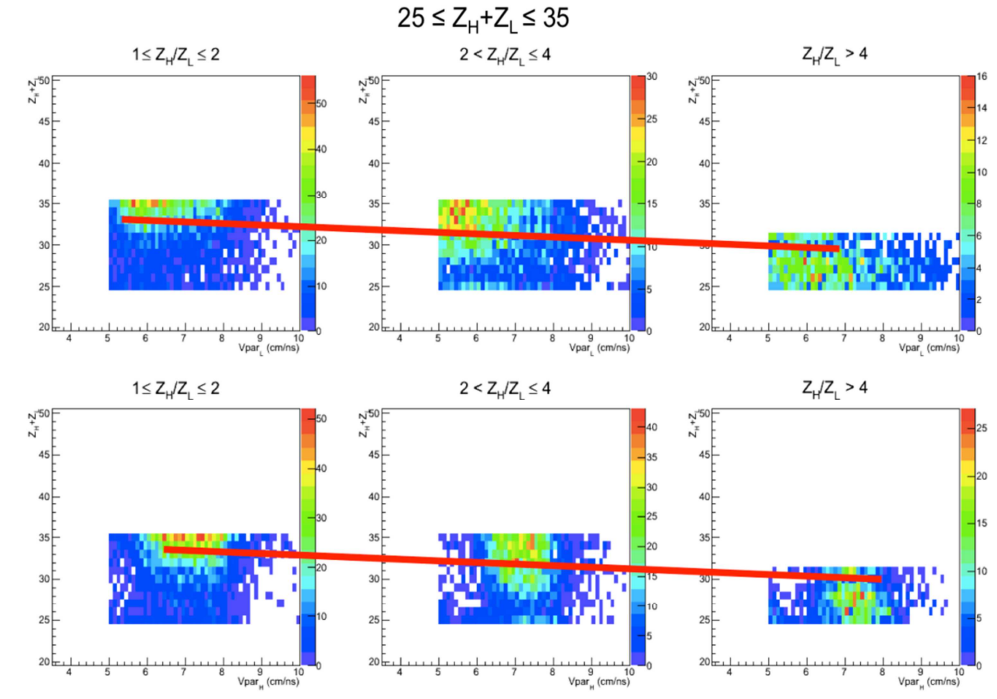

Figure 8: $Z_H + Z_L$ as a function of both the parallel velocity of the light IMF (top panel) and the parallel velocity of the heavy one (bottom panel) in the three ranges of Z_{Asy} in the most dissipative bin of sum $25 \leq Z_H + Z_L \leq 35$.

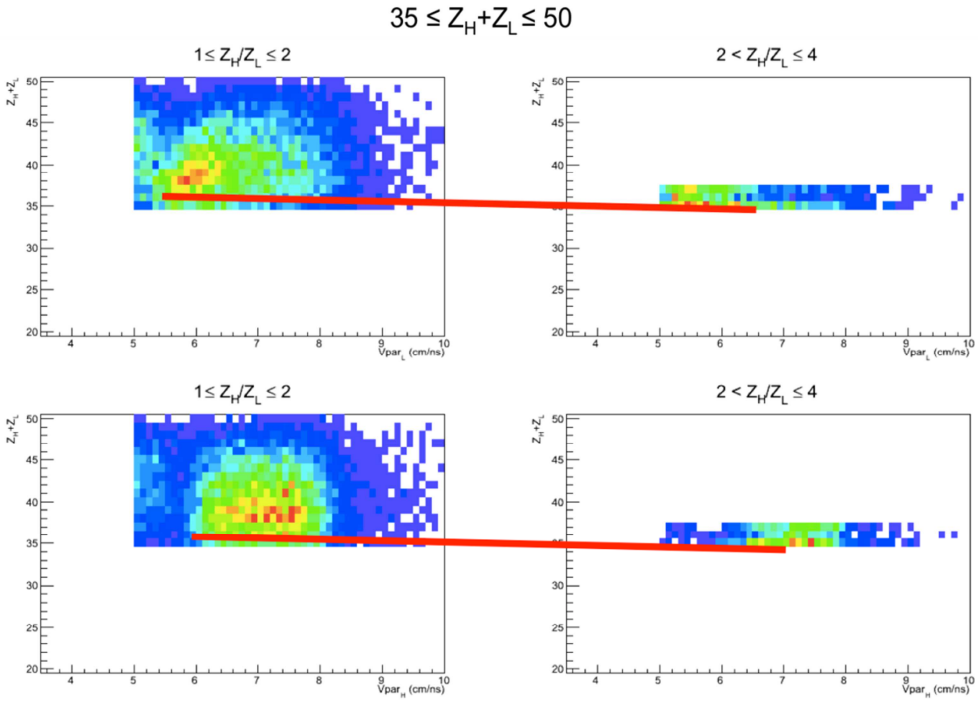

Figure 9: $Z_H + Z_L$ as a function of both the parallel velocity of the light IMF (top panel) and the parallel velocity of the heavy one (bottom panel) in the three ranges of Z_{Asy} in the less dissipative bin of sum $35 \leq Z_H + Z_L \leq 50$.

Once, the constraints in size and dissipation are used in constructing the correlation function, one obtains the results shown in the figure 10.

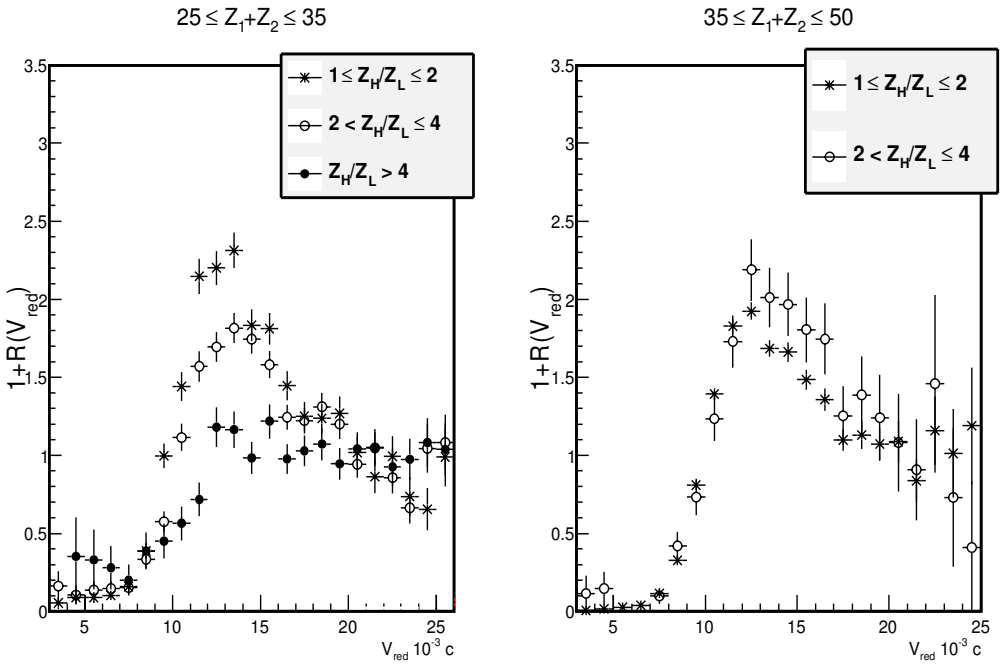

Figure 10: IMF-IMF correlation functions for different Z_{Asy}, left panel $25 \leq Z_H + Z_L \leq 35$ and $35 \leq Z_H + Z_L \leq 50$ right panel [EVP16].

In the left panel the IMF-IMF correlation functions for $25 \leq Z_H + Z_L \leq 35$ as a function of the three ranges of charge asymmetry is shown. It is clear that in this case the correlation functions preserves a kind of hierarchy as a function of Z_{Asy}: by increasing the asymmetry the intensity of the correlation is reducing and its shape is dramatically broadened, out of the experimental statistical errors bars, for the highest asymmetry. It means that in the three ranges of charge asymmetry the correlations functions highlight differences in the space-time configuration of the emitting systems. As already seen, the size and energy dissipation have been reasonable fixed (within a narrow range of charges and multiplicity distribution). So it is argued that the correlation functions are showing a genuine signature of the evolution of different time scales in the different ranges of Z_{Asy}. The present analysis, when it is compared with the results of neck and dynamical fission already published by CHIMERA group [DEF05, DEF12, RUS10, and references therein] allows to assign a time-scale

calibration of the correlation function: the lowest asymmetry is associated with fission process appearing in the later stage of the neck expansion process, i.e., time scale of about $\geq$ 120 fm/c or more, with the tendency toward an equilibrated process of symmetric fission; In contrast, the higher asymmetry is associated to an asymmetric dynamical fission component having strong similarity with the neck process reactions appearing at short time scales of about $\leq$ 100fm/c. In this respect we have probed here, in unique way by IMF-IMF correlation studies, the dynamical evolution of the neck fragmentation process of the PLF from the most prompt phenomena to the sequential equilibrated ones. In this respect, probably, the fission channel (if any) is a promising probe for time scale determination.

In the case of the right panel of the figure 7 it is shown a different effect. In fact, in contrast, for the sum $35 \leq Z_H + Z_L \leq 50$, where the smaller dissipation is observed, so associated to more peripheral collisions, no significant differences have been observed within the experimental error bars. This suggests that in this latter subset with biggest size of the source, no difference in the time scale of the IMFs involved are seen.

In order to be sure that we are looking a binary breakup/fission of the PLF the ratio between the relative IMF velocity and the one corresponding to the Viola systematic for fission decay is investigated in more details. In the case of the sum of the two atomic numbers of the IMFs in the range between $25 \leq Z_H + Z_L \leq 35$, this ratio for the three range of the Z_{Asy} is shown in Figure 11. As it is possible to observe, mostly of the IMFs pairs display a ratio very close to the unity, i.e., $\frac{\boldsymbol{V}_{rel}}{\boldsymbol{V}_{Viola}} = 1.1 \pm 0.25\ (FWHM)$ in the three spectra. The shape of the distribution is slight asymmetric with a tail toward larger

values of the ratio and extending up to the value ~2. It is argued that mostly of the IMF couples undergo a decay dominated by a pure two body Coulomb repulsion. This is a strong indication that the fission process occurs far from the reminder of the target in longer time scale as typically observed for neck emission process, where TLF-IMF-PLF are in close configuration and linked by the neck.

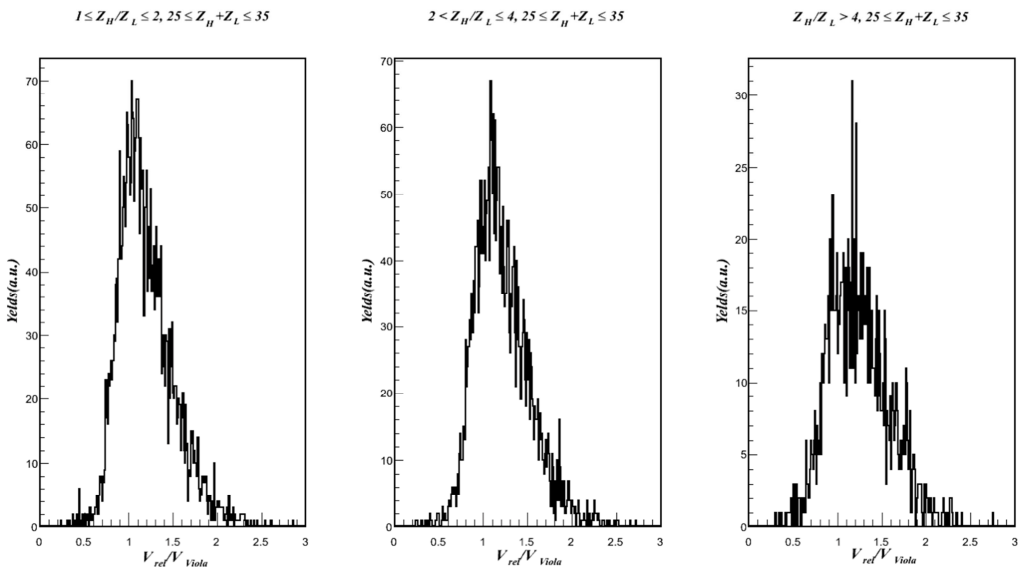

Figure 11: Ratio between the relative velocity of the two IMFs and the Viola velocity of the two IMFs for $25 \leq Z_H + Z_L \leq 35$ in the three ranges of charge asymmetry.

However, the observed deviations (tails) from pure Coulomb repulsion suggest that still a large fraction of PLF decay (~20-30 % as indication) suffers the influence of the expanding mid-rapidity zone created in the first stage of the collision; so, the fission /breakup of the PLF occurs within a shorter time scale. No sharp transition in the time scale is seen in the decay process. Similar qualitative observation are still valuable for the largest sum $35 \leq Z_H + Z_L \leq 50$, as it is possible to see in Figure 12.

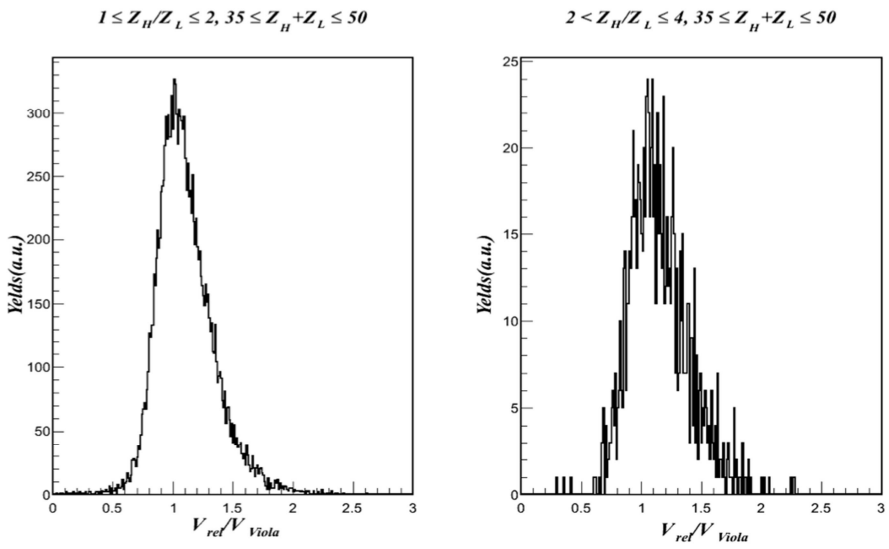

Figure 12: Ratio between the relative velocity of the two IMFs and the Viola velocity of the two IMFs for $35 \leq Z_H + Z_L \leq 50$ in the two (see text) ranges of charge asymmetry.

However, in this latter case, deviation from Viola systematics are much less pronounced and the distribution is nearly symmetric.

Consistently with the lower energy dissipation with respect to the one observed in the case of smaller size of the emitting source, it is argued that in the case of the most peripheral collisions no sizeable overlap of nuclear matter between the two interacting ions (the PLF* and the TLF*) is generated during the collision time.

So, the observed result is an agreement with the fact that the IMF-IMF correlation function does not show difference (within the experimental accuracy) in this case (see right panel of Figure 10 and see text). Notice that, for this subset, almost all of the events, belong to the most symmetric range of Z_{Asy}, in fact more than the 90% of IMFs pair observed in this subset $35 \leq Z_H + Z_L \leq 50$ show $1 \leq Z_{Asy} \leq 2$ charge asymmetry.

According to this analysis IMF-IMF correlation function is thus sensitive to the time scale of the reaction. What is still a question is how its shape changes as a function of the time scale of the reaction.

Another test of the above described result is done by investigating an additional experimental variable, the theta proximity angle, $\cos(\theta_{Prox})$. This variable is defined as the angle between the direction of the emitted PLF (centre of mass of the light (L) and heavy (H) fragments) and the fission/breakup axis (relative velocity between heavy an light fragments) [BOC00] and it is schematic represented in Figure 13.

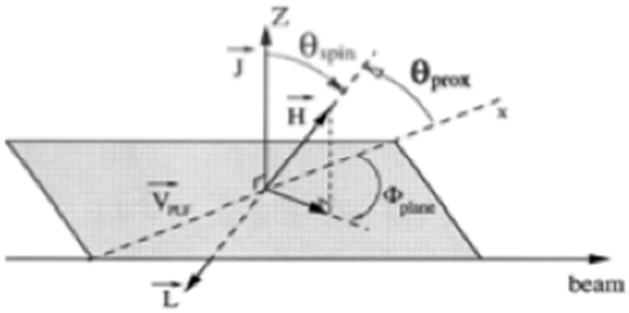

Figure 13: Schematic representation of the cosine of theta proximity angle.

The sensitivity of $\cos(\theta_{Prox})$to distinguish the dynamical emission component from the statistical one was proved, for this reaction in reference [DEF12] as already seen in figure 6 of chapter 2.

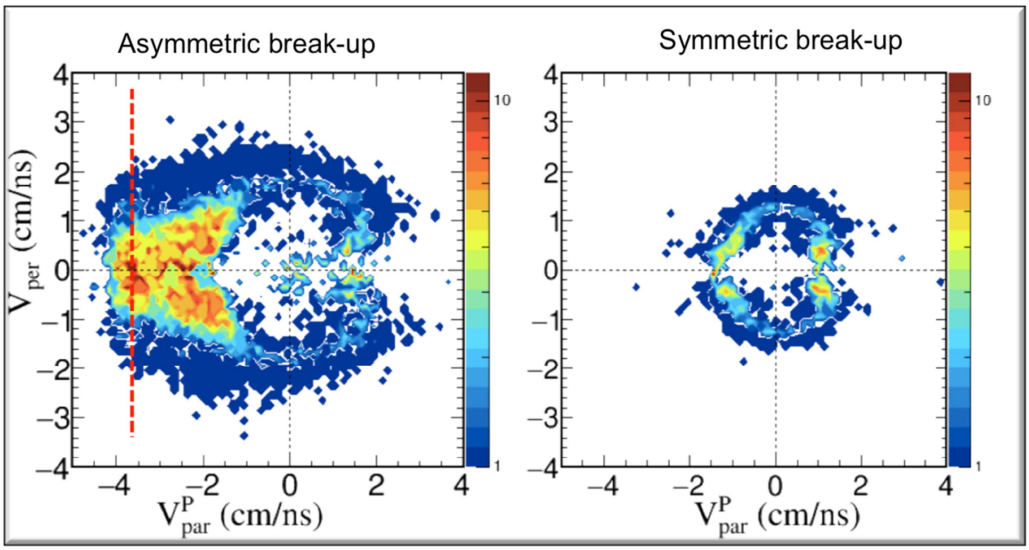

Figure 14: Invariant cross section in the case of asymmetric breakup (left) and symmetric one (right) [DEF16b].

In order to elucidate this concept, two typical invariant cross sections $\frac{d^2\sigma}{|V_{per}|\,dV_{par}\,dV_{per}}$ for asymmetric splitting (right panel) and symmetric splitting (left panel) of massive PLF (Sn-like PLF) decay in the same reaction at 35 MeV/nucleon, in a bidirectional plot $\mathbf{V}_{par}$ vs $\mathbf{V}_{per.}$ is plotted in figure 14. In the left panel it is clear that the emission is anisotropic, with a clear dominance of fragments emitted dynamically at the mid-rapidity region in a short time scale (< 300fm/c). In contrast in the right panel of the Figure 14 it is observed an isotropic emission (back-forward symmetric) of the IMF (in PLF frame). This latter plot represents a genuine evidence of a statistical equilibrated IMFs emission at longer time scale (> 300fm/c). Such patterns of both isotropy and anisotropy are reflected in the cosine of theta proximity angle, that should show either a symmetric distribution (with respect to 90° in the PLF frame, see figure 13) in the case of Fission-like/binary breakup symmetric emission (left panel in figure 14) or an isotropic distribution in the case of Fission-like/binary breakup asymmetric emission (right panel of figure 14). These further

observations are in perfect agreement with the observed behaviour of the correlation function as a function of the asymmetry. So by looking at its distribution it is possible to select the dynamical component of the emission just inspecting the behaviour of the distribution close to, $\cos(\theta_{Prox}) = 1$.

To test in a more quantitative way the sensitivity of the correlation function to the dynamical component, we chose to select a set of those events where the decay is dominated by the statistical emission, but where it is not excluded the presence of a small dynamical component. The set of our interest for this evaluation was the one having the largest sum $25 \leq Z_H + Z_L \leq 50$ and the smallest asymmetry, i.e., between $1 \leq Z_{Asy} \leq 2$.

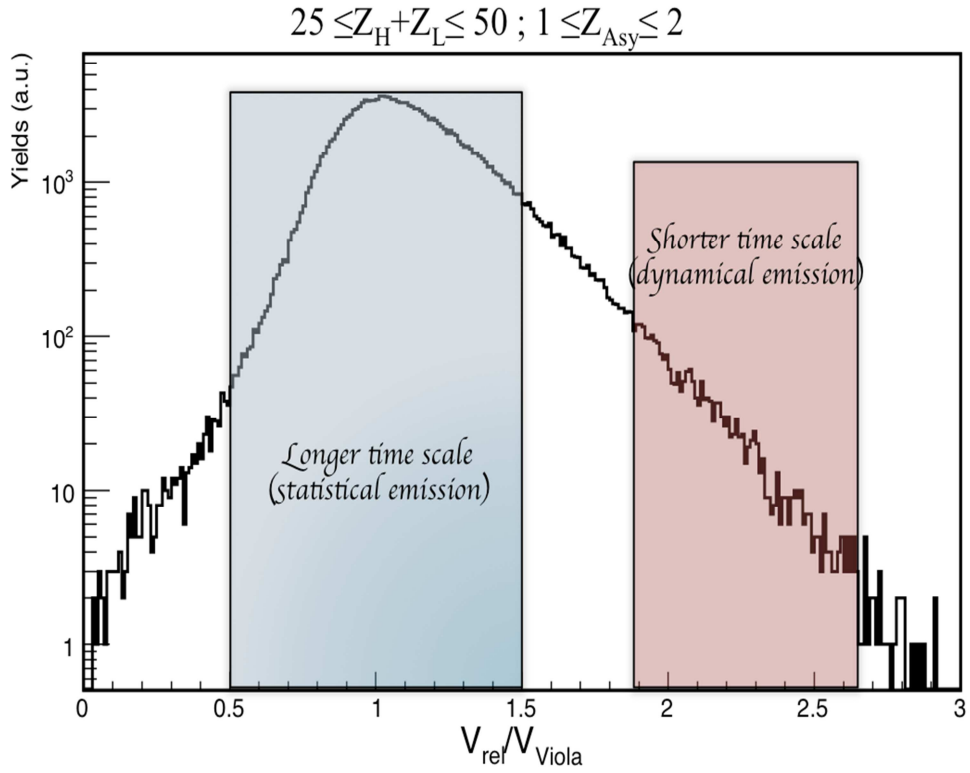

Figure 15: Ratio between relative velocity and the Viola velocity for the two IMFs.

The Figure 15 shows, in log scale, the ratio between the relative velocity and the Viola velocity in the interesting set of emission. In the figure, schematically, it is evidenced in the two rectangular regions the one, in blue colour, associated predominantly to longer emissions and the one, in red colour, where highest is the probability associated to dynamical emission.

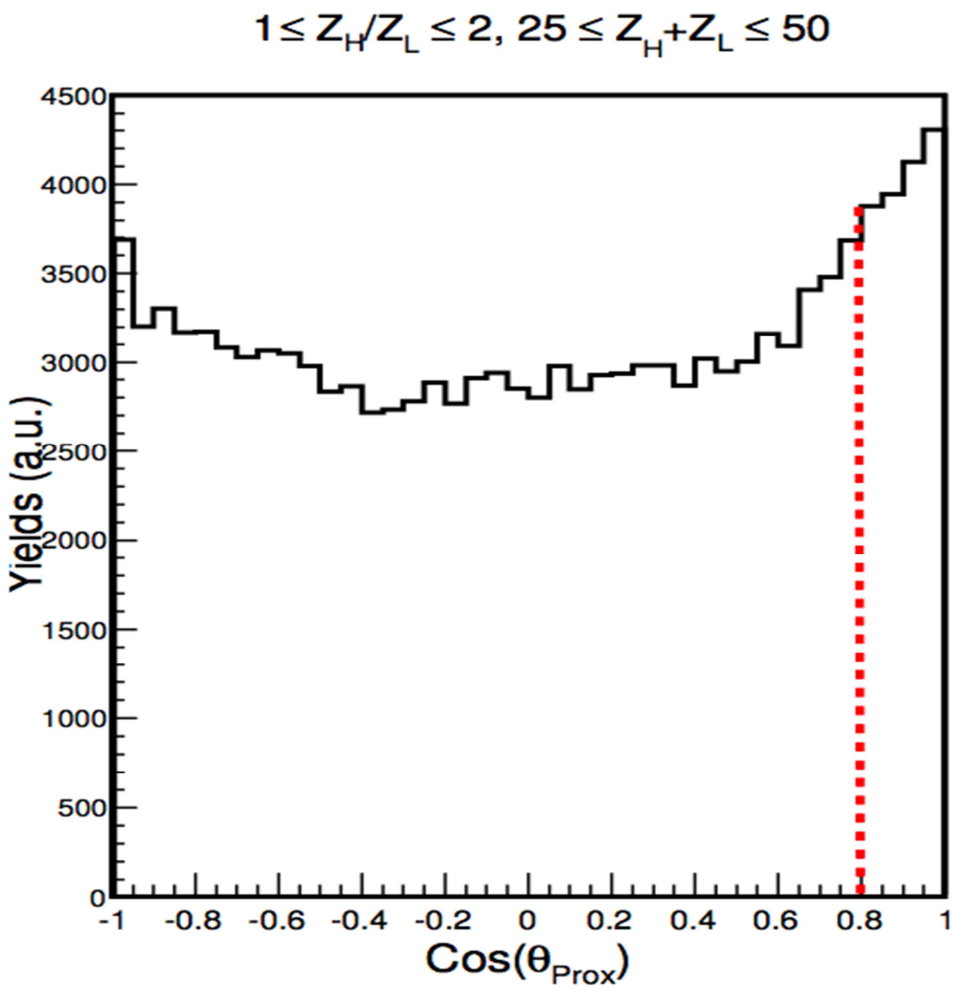

Figure 16: Distribution of the cosine of theta proximity for the most symmetric IMFs ZAsy and for $25 \leq Z_H+Z_L \leq 50$ [EVP16].

In the Figure 16 is shown the distribution of the cosine of theta proximity for the considered subset of IMFs pairs. In this distribution it is possible to observe the larger symmetric component due to the

statistical emission, and also, an asymmetric component, associated to dynamical emission. In particular, forward-backward asymmetry with respect to 90° as it is seen at $\cos(\theta_{Prox}) \geq 0.8$ is a signature of dynamical emission that is superimposed to a well-shaped symmetric distribution. Now it is important to see the IMF-IMF correlation function constrained by the $\cos(\theta_{Prox})$ and how it changes. The Figure 17 shows the evaluated experimental IMF correlation function with and without the constraint on the cosine of theta proximity greater than 0.8 (we follow the constrain for dynamical emission as it was discussed in reference [DEF16b]).

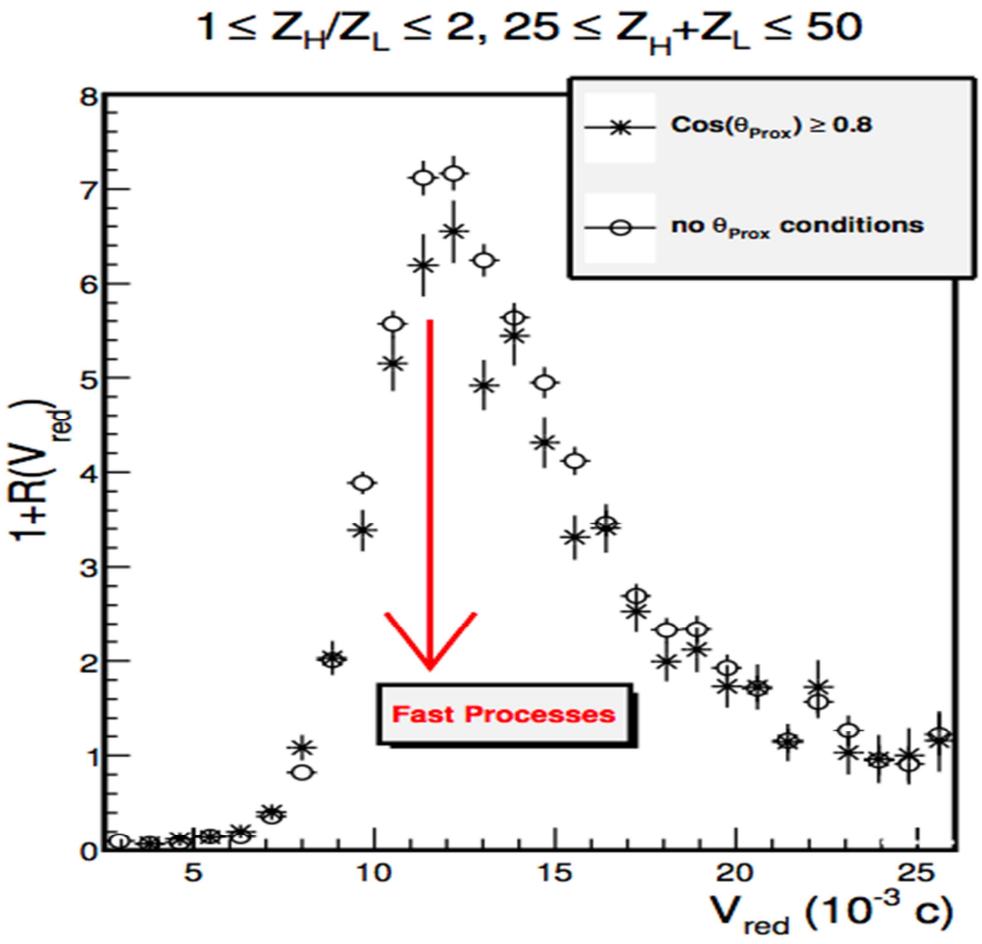

Figure 17: The IMF-IMF correlation function gated in the cosine of theta proximity(black stars) and without conditions (white circle) [EVP16].

As it is clear from the figure 17 the correlation function gated in the cosine of theta proximity angle > 0.8, black stars in the figure, changes its shape with respect to the one without that constraint, represented with white circles in the figure 17. In the two correlation functions in figure 17 no significant differences have been observed within the experimental error bars for $V_{red} \leq 9 \cdot 10^{-3}c$, where the Coulomb repulsion is the dominating physical effect. For larger values of the reduced velocity it is possible to observe differences in the shape of the two IMF-IMF correlation functions. In the range of reduced velocity $10 \cdot 10^{-3}c \leq V_{red} \leq 17 \cdot 10^{-3}c$ a clear reduction of the intensity of the correlation is observed. For values of reduce velocity $V_{red} \geq 17 \cdot 10^{-3}c$ both the two correlation functions decrease rapidly in intensity until reaching the flat shape to the unity value of the ratio.

According to this analysis [EPV16] the faster process (prompt emission) is associated to a correlation function with less intense shape, as it is schematically indicated in the Figure 17.

It is also interesting to see what happens in the ratio $\frac{\boldsymbol{V_{rel}}}{\boldsymbol{V_{Viola}}}$ when the ratio is gated also with the $\cos\theta_{Prox} \geq 0.8$ in an event-by-event analysis.

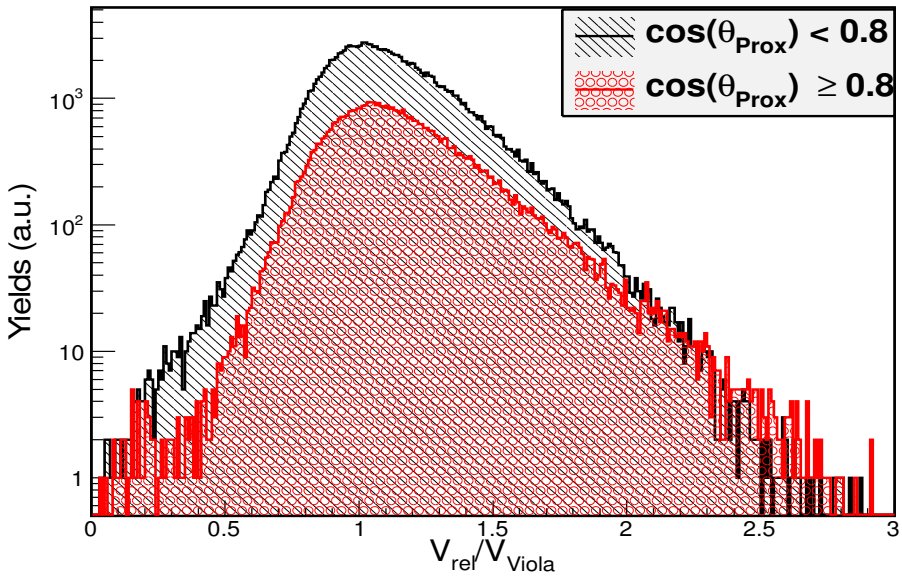

Figure 18: Ratio V_{rel}/V_{Viola} for $\cos\theta_{Prox} < 0.8$ *(black spectrum) and for* $\cos\theta_{Prox} \geq 0.8$ *(red spectrum).*

Figure 18 shows spectra of the ratio between the relative velocity and the Viola velocity for the interval of IMFs charge sum between $25 \leq Z_H + Z_L \leq 50$ and for charge asymmetry $1 \leq Z_{Asy} \leq 2$. The black spectrum is evaluated putting as constrain $\cos(\theta_{Prox}) < 0.8$ and the red one is evaluated with the condition that $\cos(\theta_{Prox}) \geq 0.8$. The black one, as it is expected, has a higher yield with respect to the red spectrum. It is important to put our attention in the part of the spectrum for value larger than 1.5 of the ratio. In this part, the ratio between the two spectra is progressively reduced up to crossing for value about $\frac{V_{rel}}{V_{Viola}} \approx 2$ where no differences are more observed (within the experimental errors). Furthermore for values larger than 2, the red spectrum has a tendency to show a larger yield. Notice that, for sure, the constraint of $\cos\theta_{Prox} \geq 0.8$ event-by-event, does not suppress the statistical component (always superimposed) but the dynamical emission becomes more important for values of V_{rel} strongly violating the Viola systematics ($\frac{V_{rel}}{V_{Viola}} > 2$)

In the Figure 18 the logarithmic scale was chosen in order to emphasize the above descripted result.

3.1 Theoretical comparisons

In order to pin down some quantitative information about the timescale of the dynamical process we made comparisons between the experimental data and the CoMDII model calculations [PAP01, PAP07].

Heavy ion collisions at Fermi energies have been described in a large variety of semi-classical approaches that are faced with the many-body problem. The one-body semi-classical transport models like the Boltzmann-Nordheim-Vlasov (BNV) and the Vlasov-Uehling-Uhlenbeck (VUU) models are not well suited to describe process in which a large number of final fragments are produced. This is due to the fact that the correlation treated in the one-body approach is not able (in the present status) to describe the large fluctuations which develop in a multifragmentation process and in which a larger number of IMFs in the final state are produced. This difficulty can be solved by adopting more suitable treatments of the N-body problem like molecular dynamics in which the N-body wave function is expressed through a direct product of wave packets, each one satisfies the minimum uncertainty $\sigma_r \sigma_p = \frac{\hbar}{2}$ where σ_r and σ_p are the dispersion of the corresponding Wigner transform in configuration and momentum space, respectively.

In this work, simulated events are calculated with the Constrained Molecular Dynamics-II (CoMD-II) model calculations for the production of primary products generated after a sufficient long time of dynamical evolution. At the freeze-out configuration the time of computation is stopped and the final fragment distribution was obtained by using the statistical decay code Gemini for sequential

decay [CHA10]. (CoMD-II) model was introduced in order to describe the fermionic nature of the N-body system with more general condition of QMD, and its implementations, and to realize a model for which the computational time is short enough to allow the study of the heaviest systems. For more precisely description of the CoMD-II model we refer to the papers [PAP01, PAP07].

In Figure 19 a detailed comparison between the main experimental observables used in this analysis and the ones obtained in the frame of the simulations is shown. A good agreement between experiment and simulation is observed for all the investigated quantities.

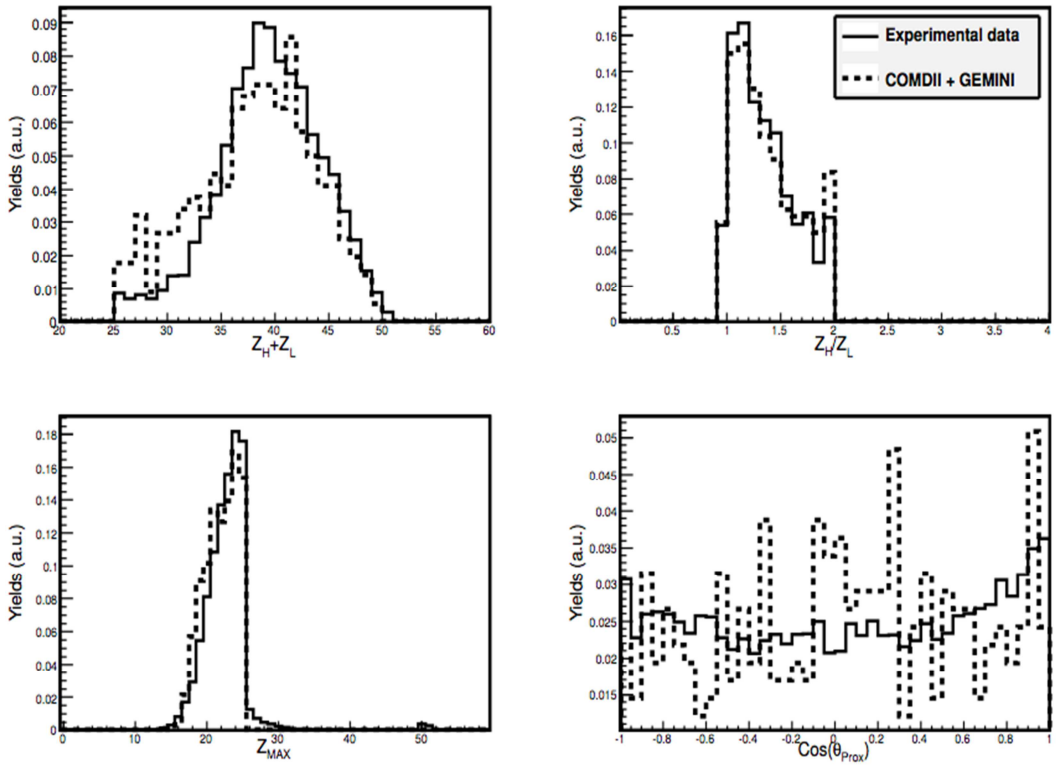

Figure 19: Comparisons between experimental (full lines) and simulate variable (dashed lines) [EVP16].

Notice that, the comparisons between experimental and simulated quantities are made by imposing in the calculated data the same

constrains assumed in the experimental analysis. These constrains are: the almost completely reconstruction of the PLF emitting fragments, in term of total charge detected, the almost completely PLF momentum reconstruction in one event, and the further requirements of a IMFs multiplicity equal to two and IMF velocity (for each one of the two fragments ≥ 5cm/ns in the lab system of reference). The other constrains both in the experimental ensemble and calculated one, are the sum of the atomic number of the two IMFs ranging between $25 \leq Z_H + Z_L \leq 50$ (i.e., the full charge distribution observed in the PLF decay channel). Besides, due to the fact that the obtained statistic of the simulation was not large enough to cover all the experimental charge asymmetries (described above) with reasonable statistical accuracy (comparable to the one obtained in the experimental data), only the lowest value of the smallest asymmetry, i.e. $1 \leq Z_{Asy} \leq 2$ was considered. So further calculations have been envisaged to overcome the present limitation.

In the top-left side of the figure 19 the comparison between the distribution of the sum of the atomic number of the two IMFs, the experimental (full line) and the calculated one (dashed line) is shown. As it possible to observe there are no differences between 35 and 42 charge units within the statistical accuracy; essentially at the lowest values of the sum between 25 and 35 charge units, similar rising shapes are observed in the two distributions with a clear tendency of the simulated spectra to show more abundant productions. However, as it is shown in the top-right part of the Figure 19, the ratio $\frac{Z_H}{Z_L}$ is predicted with good agreement.

The same kind of agreement is observed by comparing the two spectra (see bottom-left part of the Figure 19) relative to the experimental and

simulated distributions of the maximum charge (Z_{MAX}) observed in one event. Similar good agreement (within the experimental accuracy) is achieved in the cosine of theta proximity distribution that is shown in the bottom-right part of the Figure 19.

Applying to the simulations the constraints that have been used for the experimental data, result in the selection of the range of impact parameters about $2 \leq b \leq 7$ fm (shown in the Figure 20) that is consistent with the experimental ones, as deduced by using the Cavata method [DEF14, CAV90]. The experimental estimation of the impact parameter estimation was already given in Figure 6 (see insert in the bottom-right part of the figure).

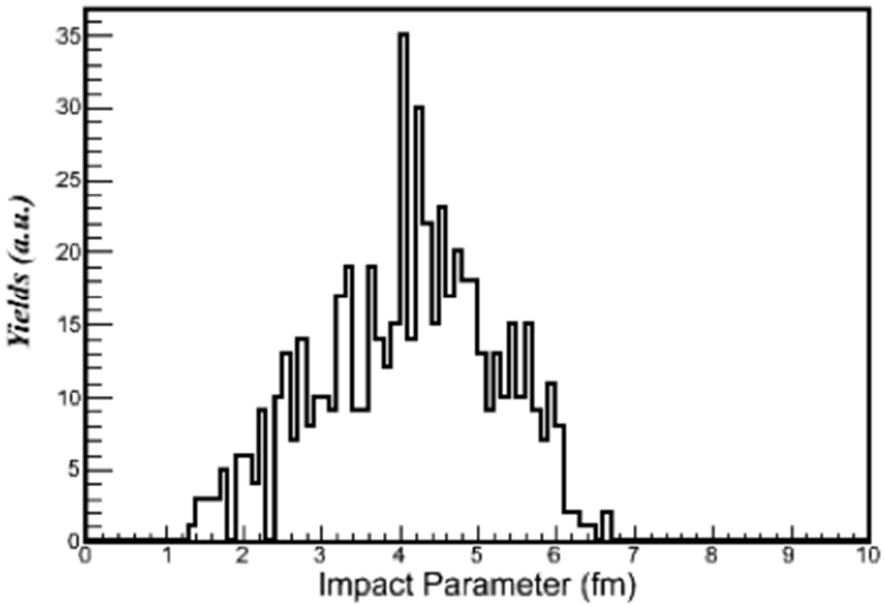

Figure 20: Calculated impact parameter distribution after the constrains.

The above comparisons were mandatory steps of the analysis in order to assure that by putting the same constrains in the experimental data and in the simulation we were selecting the same class of semi-peripheral evens.

Now we can compare the experimental correlation function with the one obtained in the constrained simulations.

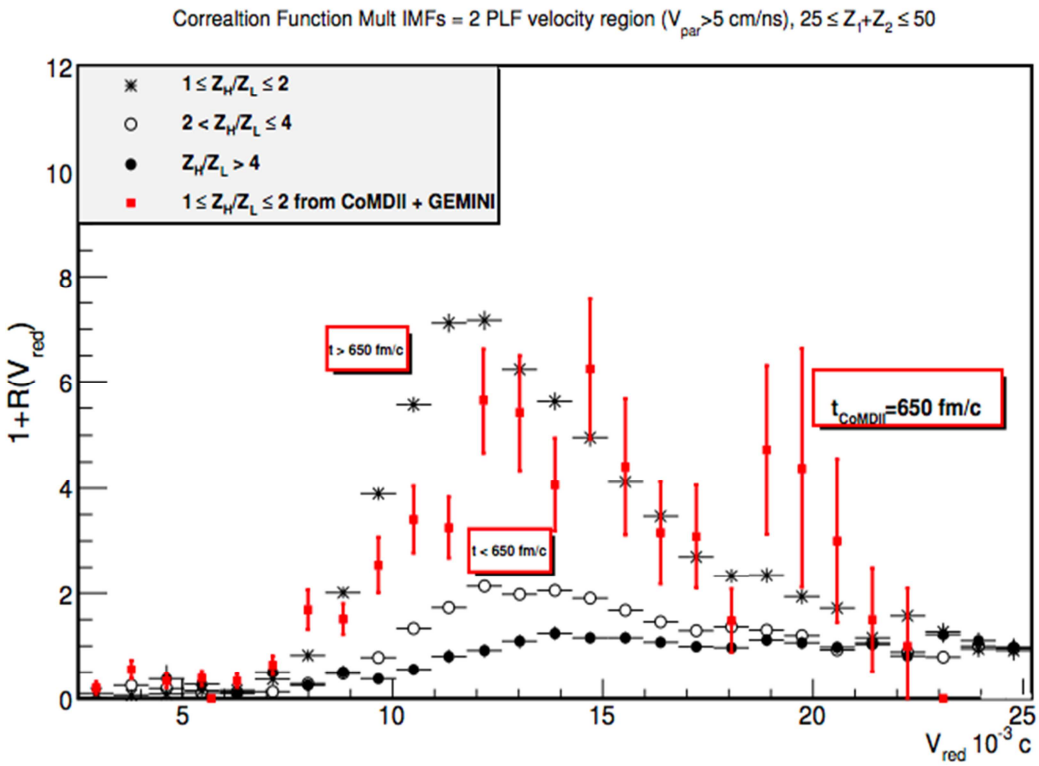

Figure 21:Comparison between experimental (black points) and simulated (red points) correlation functions.

The comparison is shown in Figure 21 where the red square points are the simulated correlation function and the black points are the experimental ones. As already said, the comparison is made only for the largest asymmetry (see top left insert). However, for simplicity the three experimental charge asymmetry correlations are also shown. In that simulation the calculation was stopped at 650 fm/c in order to cover the full dynamics. Notice that, due the limited statistics obtained by the simulation (after including all the above mentioned constraint on the generated ensemble), the error bars of the calculated correlation function are large. Anyway, within the limitation of the present accuracy a good agreement between data and simulations is observed

for the most symmetric splitting. According with the present experimental analysis we can conclude that the IMF-IMF experimental correlation function evaluated for the most symmetric range of particles is well accounted by the CoMD code + Gemini within the range of dynamics of 650 fm/c. Unfortunately, at the present, due to the severe limitation of the statistics obtained in the simulations, experimental correlation functions evaluated in the range of mid-asymmetry and large asymmetric of the two IMFs partners, that are produced at very short time scale (see analysis discussed above) where the dynamical emission is dominating, are not compared with simulations. We propose, as prospective, to produce additional simulations and to study the correlation functions as a function of time formations of the IMFs, (primary fragments) and to compare with the experimental data also the primary distribution obtained before the Gemini statistical decay (secondary fragments). Furthermore, it is also envisaged to compare the data with other transport models (like for example, the Stochastic BNV code [MDT10]) in order to obtain new information on the basic transport properties of the mechanism and in medium interactions and related time scales, that are as much as possible ‘’model invariant ’’.

4. FARCOS, Femtostope ARray For COrrelations and Spectroscopy

4.1 Introduction

As already described in the previous chapters (see, for example the introduction) studying the equation of state (EoS) of asymmetric nuclear matter represents one of the main goals in modern nuclear physics research [NSE14]. The EoS is determined by the properties of the in-medium nucleon-nucleon nuclear interaction and it plays a key role in determining the properties of astrophysical objects, such as neutron stars and supernovae explosions [STEI15]. Accessing information on the effective interaction in hot nuclear environment with baryonic density similar to the one existing in stars and stellar object, such as neutron star, is however difficult. Experimental observations rely on measurements coming from astrophysical observations and Heavy-Ion nuclear reactions, the last ones studied at accelerator facilities. A wide number of investigations performed in heavy ion collision researches are based on two- and multi-particle correlation measurements and require the use of multi detector systems of high detection qualities. These measurements require high angular and energy resolution, especially focused on the detection of light particles abundantly produced during the overall dynamical evolution of exited nuclear systems of short life time (~10^{-20}s) and far from normal density, in central and peripheral impact parameters. The present introduction highlights some of the motivations leading to the design of the FARCOS array.

FARCOS array can be used to perform particle-particle correlation measurements in heavy-ion collisions at medium (E/A<1 GeV), and

relativistic energies providing important tools to explore space-time properties of nuclear reactions with links to the nuclear EoS and the effective interaction in the nuclear medium. The Silicon and CsI(Tl) detectors thickness envisaged in the device and, consequently, the energy and timing resolutions that will be obtained (and already partially tested in a small number of beam experiments) are similar to the ones of previously used correlations instruments in different laboratories in the Fermi energy regime. Among them we mention the LASSA Silicon strip and Caesium Iodide array [DAV01] used at the NSCL of MSU for particle-particle correlations at beam energies E/A=40-120 MeV.

The FARCOS array will be characterized by a very high angular and energy resolution, profiting also from the experience and technical advances achieved with the realization of the CHIMERA [PAG04] multi-detector, thus, by coupling FARCOS with CHIMERA the overall performances of the ensemble is increased. Furthermore large solid angle coverage (achievable with a sufficiently high number of FARCOS telescopes) is mandatory in order to simultaneously explore correlations among particles emitted in different source velocity regions (such as emission from quasi-projectile/quasi-target as well from the mid-velocity region source). Different sources are indeed characterized by different space-time and thermal properties that need to be accessed in a extensive way in order to better understand the underlying emission mechanisms and in order to explore phenomena occurring over different both baryonic density- and time-scales.

FARCOS consists of a new array that is designed and constructed in the frame of INFN - NEWCHIM experiment and supported by the INFN-Commissione Nazionale Scientifica III from 2015 to 2019. The

original idea, driving the construction of the prototype of FARCOS during the years 2013-2014 [ACO12, VER13, QUA14, EVP15], has been developed in the frame of the CHIMERA/EXOCHIM collaboration with researchers and technical staff from the INFN - Sezione of Catania & Catania University, LNS, Milano INFN divisions & Milano University, and Napoli & Napoli University, and including the participation of researchers from France, Spain, USA and Mexico Institutions. FARCOS will be a compact and relatively small-solid angle detection system of order of magnitude ~200msr characterized by both high angular and energy resolution, modularity and having the peculiarity to be movable in a rather simple way to be coupled to different detector systems in laboratories around the world.

In fact, it will be possible to use FARCOS together with the 4π configuration of the CHIMERA detector []PAG04] by covering different angular regions, depending on the physics case to be addressed and on the beam energy and kinematics of the reaction.

The coupling of FARCOS with a 4π detector array is mandatory in order to measure global variables of the events such as the total charged particles multiplicity, the reaction plane orientation, the total momentum, ecc.

The use of FARCOS array in coincidence with detectors of large solid angle acceptance, including focal detection planes of magnetic spectrometers (as for example MAGNEX [CUN02] working in Catania) represents important progresses not only for typical studies on isospin physics, already covered in the framework of the CHIMERA experiments [DEF14 and references therein], but also in studies of heavy-ion collisions where two- and multi-particle correlations play a fundamental role in both dynamics and

spectroscopy studies. In summary, new perspectives will be opened in nuclear physics with both stable and radioactive beams working with the CHIMERA-FARCOS system at INFN - LNS, or coupling FARCOS with other detectors in national and international laboratories (as for example SPES-LNL, GANIL, GSI).

4.2 Description

In particle-particle correlation studies, a good reconstruction of the relative both linear momentum and energy depends on angular and energy resolution of the detector. High energy resolution is also required in spectroscopy studies where it is very important in order to separate single unbound states with good resolution.

FARCOS is a modular arrays of telescopes each one consisting of three detection stages. The first two stages are two Double Sided Silicon Strip Detectors (DSSSD) with 32 vertical strips in the front side and 32 horizontal strips in the back side. For both sides the area is 6.4×6.4 cm^2. The first stage is 300 μm thick and the second one is 1500 μm thick. The last stage consists of four CsI(Tl) crystals of 6 cm of thickness read by a photodiode, of area 18×18mm^2. The Fig. 1 shows the three stages of a single cluster of FARCOS (left side) and their typical close assembling (right side). It is important to note that each cluster has been designed to be equipped with 132 independent read-out electronics channels.

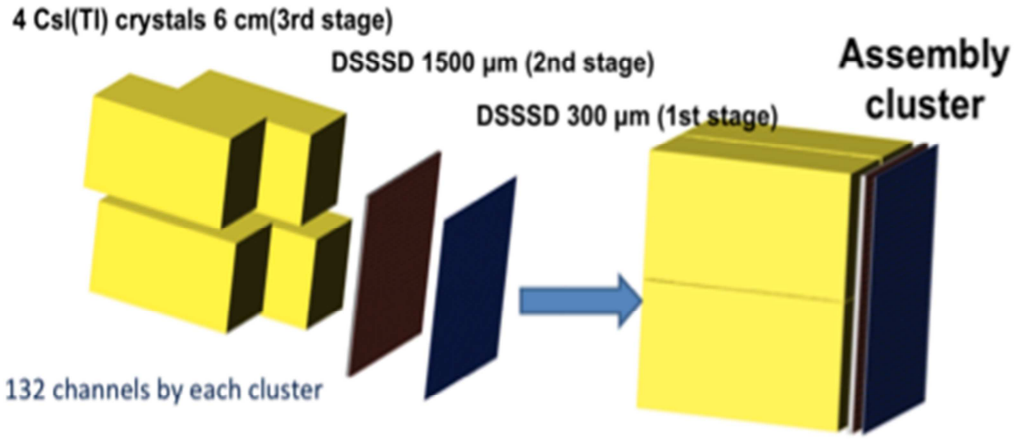

Figure 1: Schematic view of a cluster of FARCOS.

Particle identification techniques in FARCOS are performed, such as in the CHIMERA multi-detector, by ΔE-E technique adopted in the first two stages of DSSSD for particles that are stopped in the second DSSSD and in the second and third stages, by using the 1500 µm of DSSSD-silicon strip for ΔE and the CsI(Tl) for the residual energy loss of the particle, that are full stopped in the crystal.

Additional, however also important, identification techniques will be the pulse shape technique (PSD) performed in the CsI(Tl) crystals and also we plan to perform PSD in the first step of 300µm of DSSSD (as it is in the CHIMERA detection system) in order to decrease the energy detection threshold and moreover we also plan to take into account the Time of Flight (TOF) method. This latter method, is very useful not only for direct velocity measurement with accuracy of the order of 5%, but also, what is even more important, to measure the time coincidence spectra that in correlation study could be decisive information to remove, efficiently, spurious counting rates, depending, of course on the specific experiment to be performed (intensity of the beam impinging on the target, environmental background due to re-scattering effects, etc.). Beside, the innovative design, portability and

modularity are important characteristics making feasible the easy coupling with 4π detectors or other kind of correlators and/or magnetic spectrometers. We plan also to move and use FARCOS not only at INFN-LNS but also in other laboratories; in particular our research group has already submitted a letter of intent for the new facility for radioactive ion beam, SPES, under construction in the National Laboratory of Legnaro (LNL) of INFN and/or the future FRIBs project planned to be upgraded (with respect to the present version) in connection with the high intensity beam (two order of magnitudes larger than in the present facility) expected for the new version of the LNS-cyclotron in order to satisfy the experimental necessities of the NUMEN project [NSE14]. Both project (the one in LNL and the other in LNS) involve the use of FARCOS in its activity research plan. It is planned that in its final configuration FARCOS will have completely integrated and reconfigurable and digitalized electronics. In particular using the ASICs technology, it is under testing a final prototype of the first ASIC preamplifier designed by collaborators of NEWCHIM experiment of Politecnico and INFN of Milano.

4.3 First test with radioactive sources and beam during InKiIsSy experiment

Several tests were performed in order to characterize the surface light uniformity response of the CsI(Tl) crystals made by using radioactive alpha particle source. A good uniformity (~ 1%) was achieved in the light response of the crystal under irradiation of alpha source; the figure 2 shows this good result.

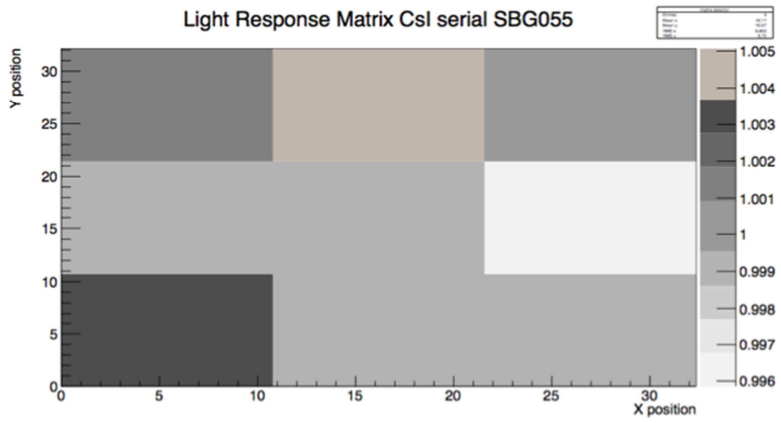

Figure 2: Typical matrix of uniformity gradient of a CsI(Tl) [EVP12][QUA14].

The CsI(Tl) crystals, that are produced by the Scionix are Thallium doped, to improve the identification capability with the PSD method (in particular for the ~1μs decay time emission component of the light).

The thallium is incorporated into the lattice of CsI(Tl) detector of FARCOS in molar concentrations of the order 1200-1500 ppm during crystal growth [SCH90]. The light output depends on thallium doping concentration, the temperature and, possibly, other chemical or physical properties of the crystal. Evidently, for this reason such tests were very important. In fact, the observations of local non-uniformities in light output [WAG01] have been often attributed to non-uniformities in Tl doping concentration. For a more detailed description about the tests we reminds references [EVP12, FTDR, QUA14, ACO16].

CsI(Tl) properties have been analysed also in the contest of the work of this PhD thesis, however essential results have been already shown and/or published. So, in order to optimize this presentation, particular emphasis is done for test identification procedures of the silicon detector performed with in beam experiments, that represents a so

large and time consuming background activity of this PHD work.

A FARCOS prototype made by 4 telescopes was tested and coupled for the first time with the 4π CHIMERA detector with beam during the Inverse Kinematic Isobaric System (InKiIsSy) experiment performed on April 2013, where a ^{124}Xe beam at 35 AMeV delivered by the LNS-INFN of Catania Super-Conductor facility (CSC). In that experiment, FARCOS covered the range of polar and azimuthal opening $\theta_{lab} \approx 16° \div 44°$ and $\Delta\Phi \approx 75°$, respectively, corresponding to a solid angle coverage of ≈ 262msr; in Figures 3 two pictures of the experimental setup are shown. As a consequence, a portion of CHIMERA was shielded by FARCOS telescopes, thus giving the opportunity to investigate also about detection of neutrons in CsI(Tl) [AUD15].

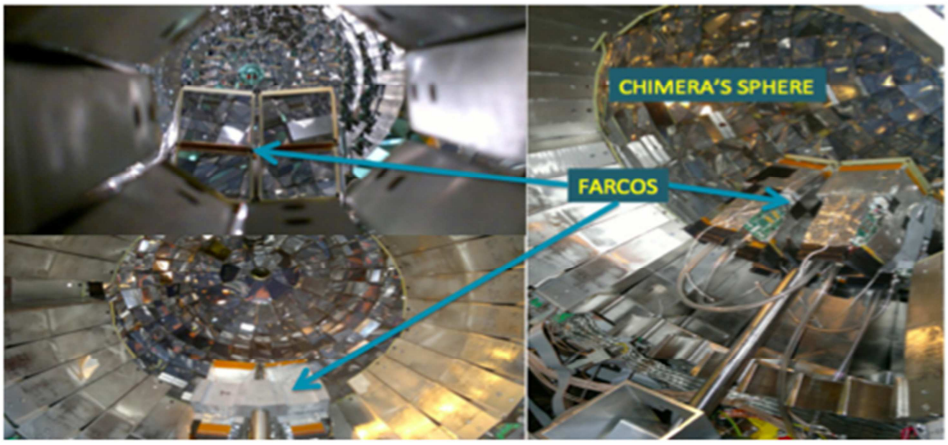

Figure 3: The InKiIsSy experimental setup. ^{124}Xe+^{64}Ni @ 35 AMeV was the studied reaction [EVP16b].

In that experiment as preliminary prototypes, we used an improved versions of CHIMERA-like standard preamplifiers (PAC) for both

CsI(Tl) crystals and silicon detectors already developed to match with the necessity of low electronics noise and TOF performances as required in CHIMERA detector [BOI04]. As first step of the R&D activity, the read-out of 32 silicon strips was performed by a compact housing, 86x80x10 mm (NPA-16FL/E), allocating 32-channels Charge Preamplifiers (PACs) with pseudo-differential signal output of low power consumption (<900 mW for 32 channels) [KNO00](see Figure 4).

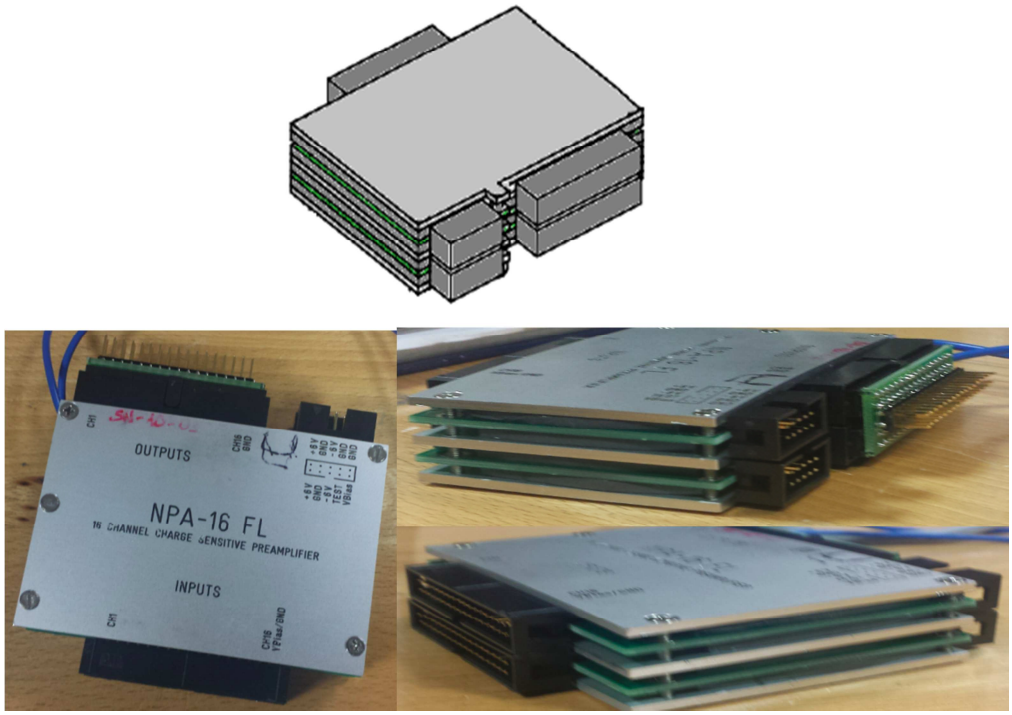

Figure 4: Schematic view of the prototype of the PAC of FARCOS (top of the figure). Picture of the PAC (bottom).

Occasionally, this preamplifier (PAC) was used for first characterization of the FARCOS array composed by 4 modules and it was used to read out the signals coming from the two stages of DSSSDs. In the InKiIsSy experiment, only the second stage of Silicon strips, the one of 1500μm of thickness, was read in the full

configuration for the all 64 channels (32 from the front side and 32 form the back side), in the case of the first stage of silicon strips only the 32 front channels were indeed processed.

For simplicity, the characterization the DSSSD is mostly illustrated by starting with the performances of the first telescope, among the four, and indicated in the following, as telescope number one.

Figure 5 shows picture as it follows: in top panel the total hits multiplicity of the first step of 300μm of DSSSD, in bottom-left the same spectra for the 1500μm font side and in bottom-right for the 1500μm back side.

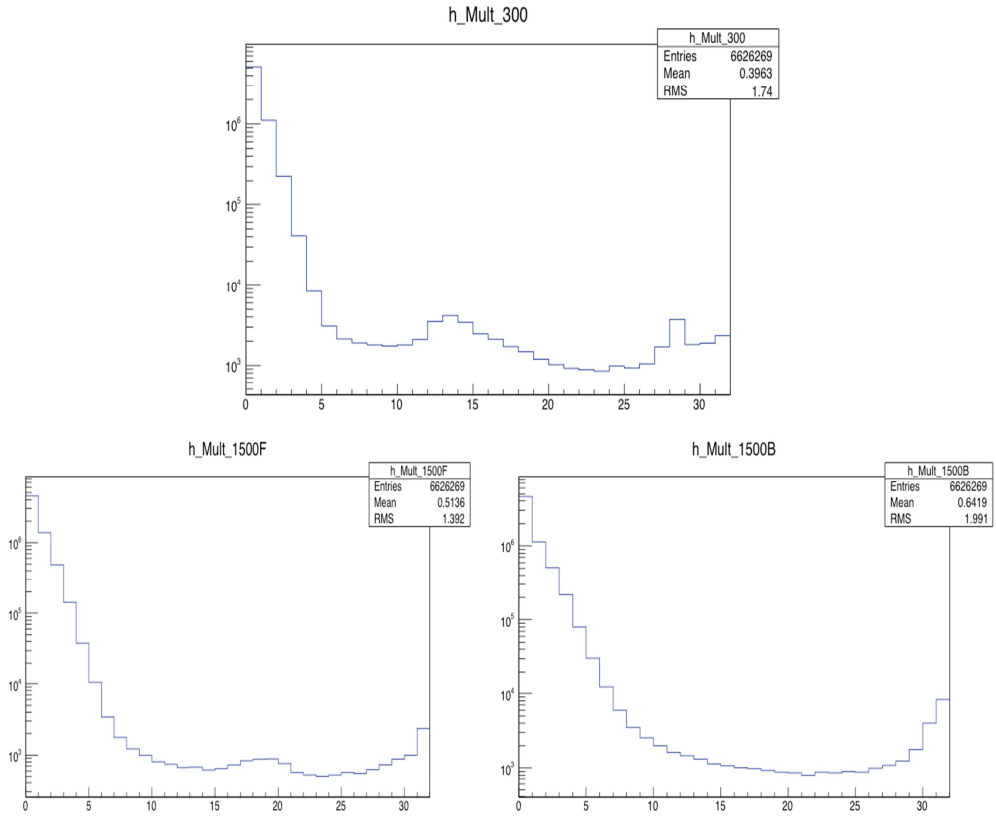

Figure 5: Total hits multiplicity for the first front stage of DSSSD (top) and for the second stage front (bottom-left) and back (bottom-right).

In the horizontal axis of the spectra in figure 5 the multiplicity of hits of the events is reported. In the vertical axis the corresponding yield is reported. As it is clear from an inspection of figure 5, there are different issues in the spectra. First of all, in the three cases a peak for multiplicity hit equal to zero is found. This is due to the fact that the FARCOS array in the InKiIsSy experiment was in slave with respect of the master trigger. In other words the hit multiplicity equal to zero means that the acquisition system was triggered by the telescopes of CHIMERA multi-detector without any signal in FARCOS. Another

issue is related to the very high hit multiplicity registered, it reaches value as high as 32. That means that there were events where 32 hits were registered by the 32 strips of the telescope number 1. It is evident that it is physically impossible that 32 particles fired the detector in the same event. Evidently, it simply means that hits corresponding to cross-talk, associated with electronics. In fact after the observation of this strange phenomenon we investigate the ΔE-E matrixes between the strips of the first 300μm DSSSD stage and the corresponding strips of the second one of 1500μm in thickness. After hard studies in the analysis, our conclusion was that the best way to cut out of the spectra the spurious hits were to adopt in software off-line analysis, for all of three stages (300μm front, 1500μm front and the 1500μm back), the condition that the total hits multiplicity should be limited to the value: is $1 \leq Mult_{Hits} \leq 8$. These constraints are shown in figure 6.

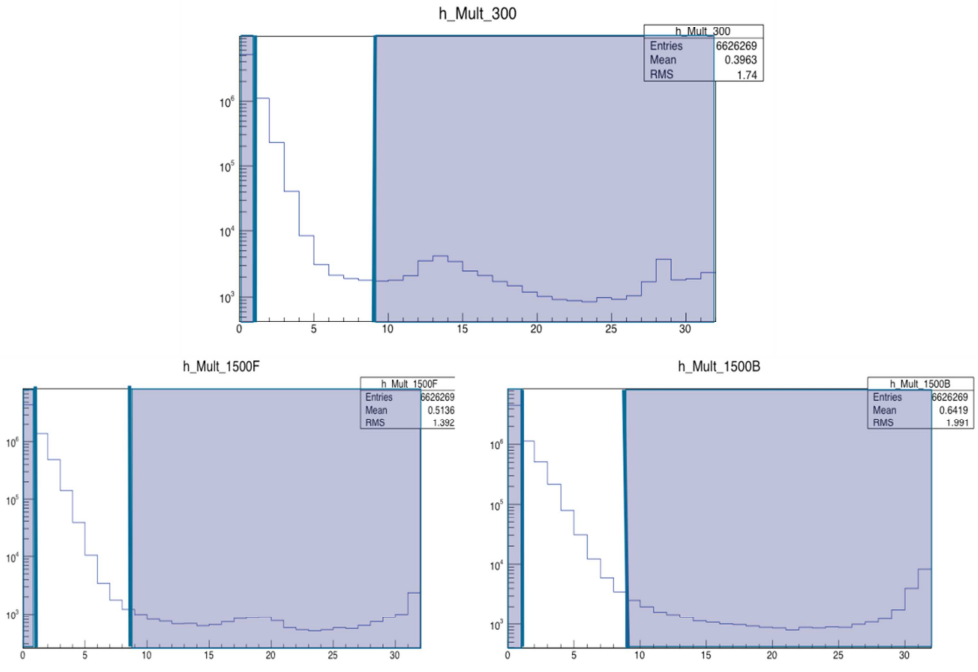

Figure 6: Constrained spectra (see Figure 5).

In the figure 6 the hatched part is the one rejected by our constraints. The rejected events are not of physical interest and are produced by electronic noise that affected the multiple-line prototype of PAC used to read oud the signals coming out of the detectors (see figure 4).

One proof that with these conditions only electric noise is removed and nothing related to the real physical signals can be seen by inspecting the figures 7, 8, 9, showing the energy spectra of the detected particles.

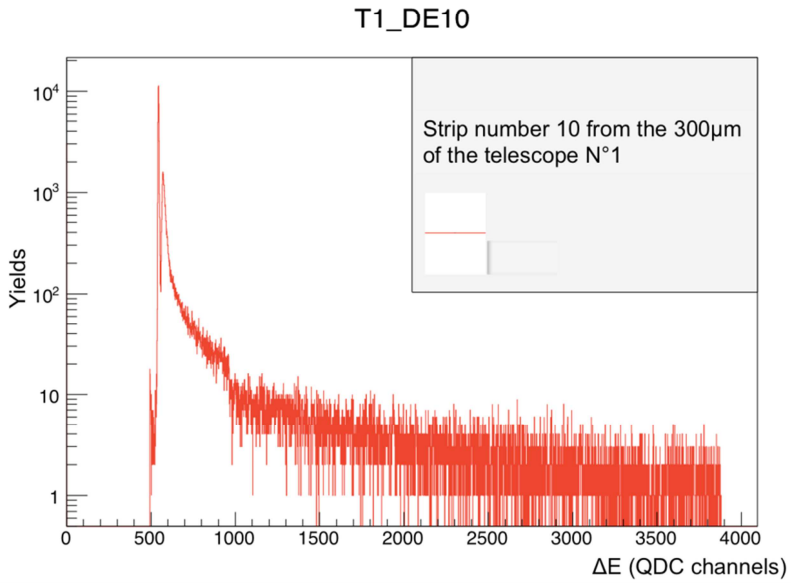

Figure 7: Energy spectra in QDC channels the strip number 10 of the 300µm DSSSD of the telescope N°1 (no cut).

Figure 7 shows the strip energy spectra, in QDC channels, in the case of the strip N°10 for the 300µm DSSSD of the first telescope of the FARCOS array. In the figure there are two peaks at lower channels (corresponding to lower energies), the first peak is around the channel

Ch≈580 and it is much higher than the second peak (Ch≈600) of about a factor 10. This first peak is consistent with the electronic noise introduced by the PAC, in fact, as it shown in figure 8, by selecting events having hit multiplicity greater than 8, $Mult_{Hits} > 8$, practically, the whole spectrum is not suppressed, except the first peak.

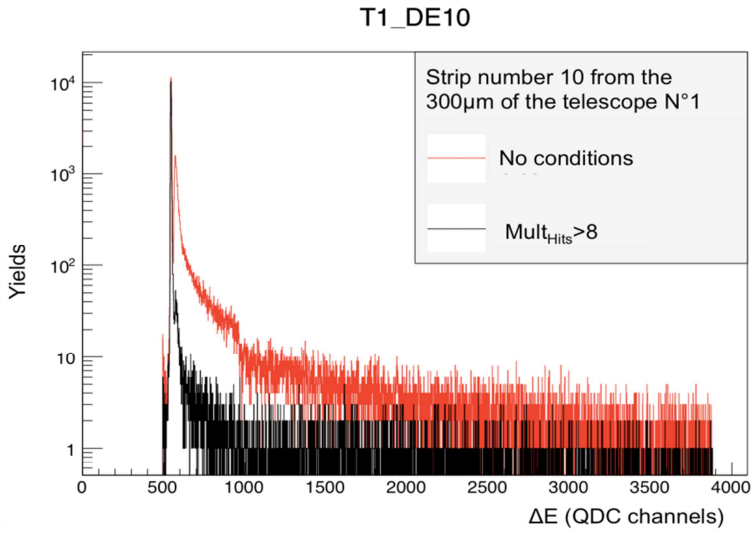

Figure 8: Red spectrum like figure 7, the black one have the condition of $Mult_{Hits}>8$.

In contrast events having $1 \leq Mult_{Hits} \leq 8$, show spectra without the strong low channels peak component. It is important to note that the two set, $1 \leq Mult_{Hits} \leq 8$ and $Mult_{Hits} > 8$ are not complementary because in both of them the condition $Mult_{Hits} = 0$ is missing. In figure 9, the comparison among the three spectra it is shown. Notice that the adopted constrain $1 \leq Mult_{Hits} \leq 8$ is a good condition in order to suppress the high electronic noise of the PAC. The same analysis was done with the 1500µm DSSSD front side and it was observed exactly same phenomenon.

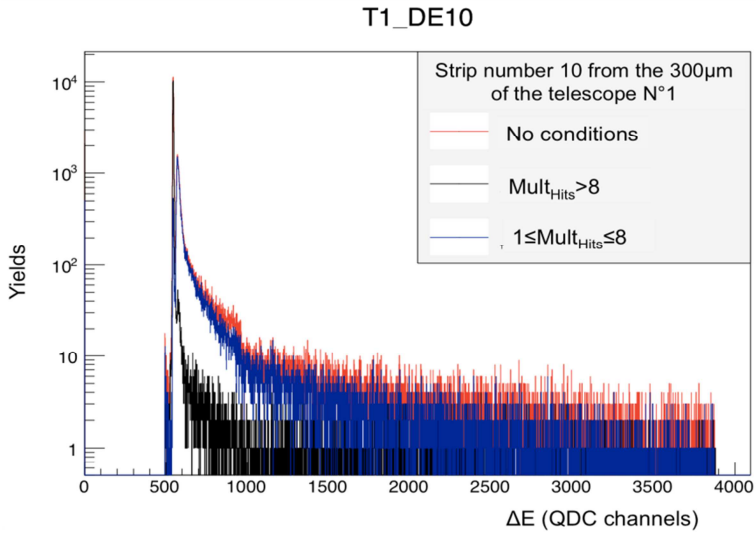

Figure 9: Comparison among the three spectra without cut (red) and with the two conditions $Mult_{Hits}>8$ (black) and $1\leq Mult_{Hits}\leq 8$ (blue).

Another proof of the goodness of the condition $1 \leq Mult_{Hits} \leq 8$ is obtained analysing the ΔE-E identification matrixes. The following figure 10, 11, 12 show identification ΔE-E Matrix obtained by correlated energy losses in the first 300µm DSSSD detector (in particular the strip number 5 working in transmission for the impinging particles), and in the second stage of 1500µm DSSSD, working as stopping detector (the corresponding strip number 26). In the two axes the energy loss of the particle is in QDC channels. The two correlated strips are, of course, aligned in such a way that the first one is followed by the second one; in fact the numbers 5 and 26 for the first strip and for the second strip, respectively, are simple due to mathematical order chosen for their easy acquisition: it means that if you take the strip number X in the first DSSSD stage the corresponding strip in the second DSSSD stage will be Y=31-X).

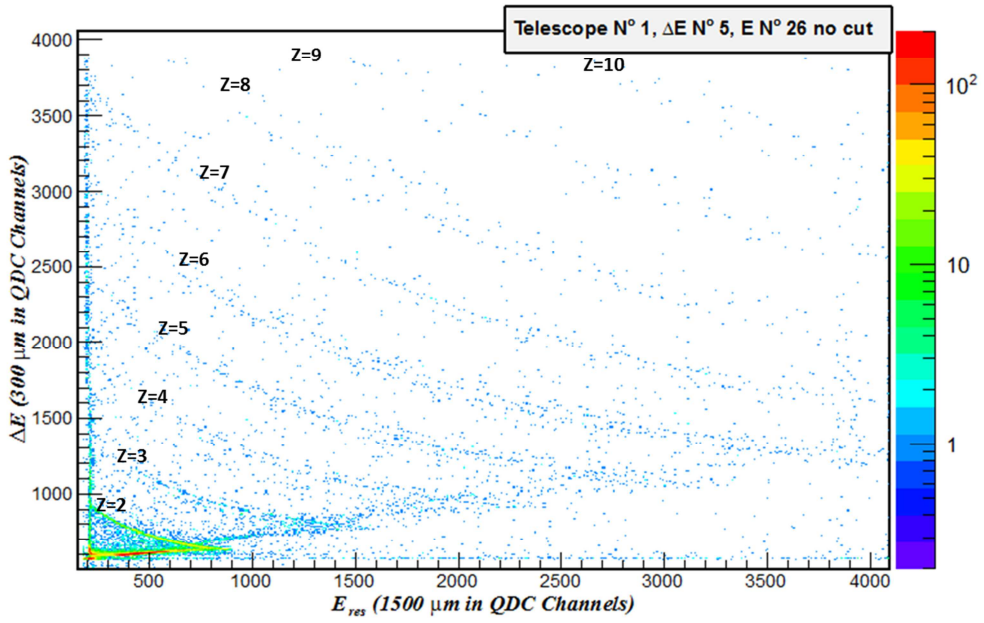

Figure 10: ΔE-E Identification matrix between the first two stages of DSSSD without any conditions.

The figure 10 shows the identification ΔE-E matrix evaluated between the strip number 5 of the first DSSSD and the strip number 26 of the second DSSSD without any conditions in the $Mult_{Hits}$. For each atomic number there is a typical dominant hyperbolic-like locus, that is a crude experimental representation of the ΔE-E behaviour, as expected by the Bethe and Bloch formula, starting form the most visible hyperbola-like corresponding to atomic number equal to 2, alpha particles and He element, up to atomic numbers equal to 10, i.e., Ne element. Looking at the spectra it is possible also to see sub structures corresponding to a given dominant hyperbola lines, each one of these sub structures hyperbola lines represent an isotopes.

The locations corresponding to a given isotope have the hyperbolic functional shape because the formula that describes the phenomenon of loss of energy of a particle in a material has the following relativistic approximation:

$$-\frac{dE}{dx} = \frac{4\pi e^2 z^2}{m_0 v^2} NB \text{ (4.1a)}$$

and

$$B = Z[\ln(\frac{2m_0 v^2}{I}) - \ln\left(1 - \frac{v^2}{c^2}\right) - \frac{v^2}{c^2}] \text{ (4.1b) [KNO00]}$$

where v and z are the velocity and the atomic number of the incident particle, N and Z are the density and the atomic number of the absorber material (the detector), m_0 and e are respectively the mass and the charge of the electron and I is the ionization potential of the absorber material. So taking into account the constants and a non-relativistic approximation the formula 4.1a (largely sufficient for the present work) can be written as:

$$\Delta E \propto \frac{m_p z^2}{E} \cdot \Delta x \text{ (4.2a)}$$

and after simple steps it (4.2a) becomes:

$$\Delta E \cdot E \propto A_p \cdot z^2 \cdot \Delta x \text{ (4.2b)}$$

in which A_p and z are the mass and the atomic number of the incident particle and Δx is the thickness of the detector crossed by the particle. It is clear that for a given Δx the formula (4.2b) represents a hyperbola depending linearly on the atomic number of the particle and quadratically on its charge.

Obviously, the spectra of figure 10 include also some points that do not belong to any hyperbola. It is possible to observe it especially in the lower part of the spectra, within channel 500 in the E_{res} axis.

In figure 11, the same ΔE-E identification matrixes seen in figure 10, there it is shown,

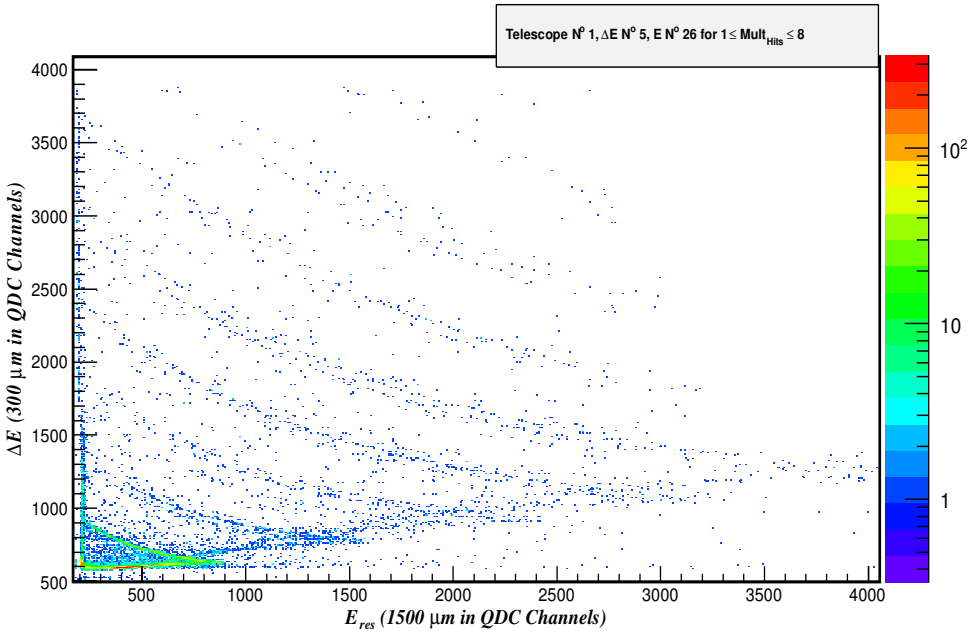

Figure 11: ΔE-E Identification matrix between the first two stage of DSSSD for 1≤$Mult_{Hits}$≤8.

But, here, the condition of 1≤$Mult_{Hits}$≤8 was applied, and the identification matrix became more clear in particular in the lower part of the spectrum, where a strong contribution of the electronic noise was already evidenced. It is also possible to observe that in that identification matrix of figure 11 no particles having atomic number greater than 7, for QDC channels larger than 3000 of the E_{res} signal have been seen. Those particles are in the identification matrix spectrum shown in figure 12 where the constraints is $Mult_{Hits} > 8$.

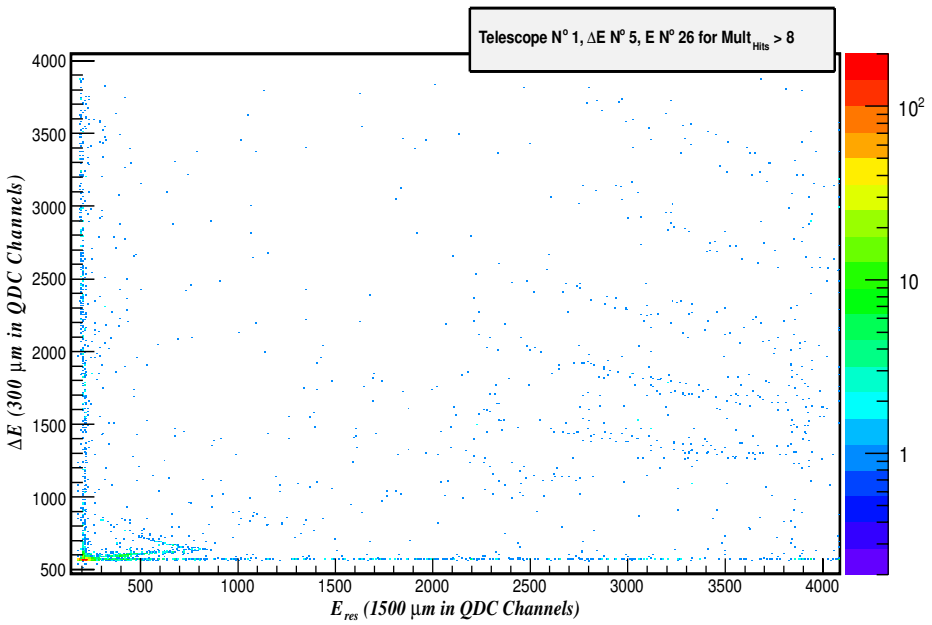

Figure 12: ΔE-E Identification matrix between the first two stage of DSSSD for $Mult_{Hits}$ > 8.

In figure 12 it is possible to see also alpha particle of lower energy of E_{res}, but with the advantage that now we suppress a lot of electronic noise. So, we have also real particles signals (with very limited statistics) in case of $Mult_{Hits}$>8. However, for the purpose of identification procedures, it was chosen to work with the sharp constrain of $1 \leq Mult_{Hits} \leq 8$ in order to go on in the best way (practically, almost total suppression of the electronic noise).

Another effect that was observed studying the particle identification of the prototype of FARCOS array was, what could be named, "Effetto Calotta". This effect is related to the fact that the particle detection is observed not only between a given strip of the first stage geometrically correlated with the corresponding strip of the second stage but also with the strips of the second stage that are adjacent or close to the main geometrically correlated strip (in this analysis, the number 26), as previously described. To be more clear on that effect, referring to the strip number 5 in the first DSSSD stage, we have seen

particle detection in the strip number 26 (in fact $31 - 5 = 26$), as already described, but also there are real coincident particles detected with the strip number 27 of the second stage, as it is possible to see in figure 13.

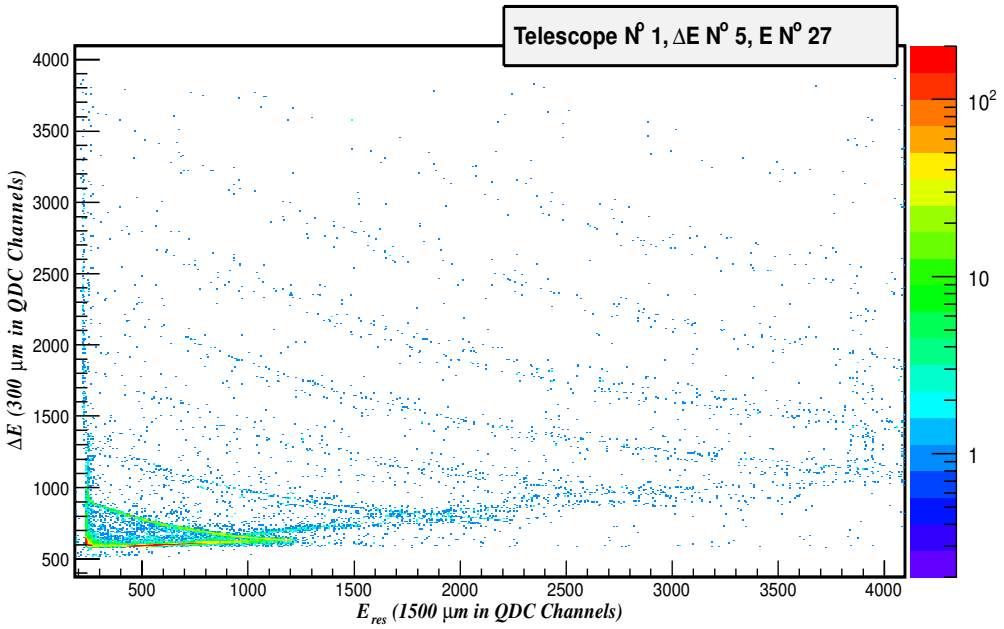

Figure 13: ΔE-E Identification matrix between the first two stage of DSSSD respectively N°5 and N°27.

When an empty identification matrix was expected (see for example figure 14).

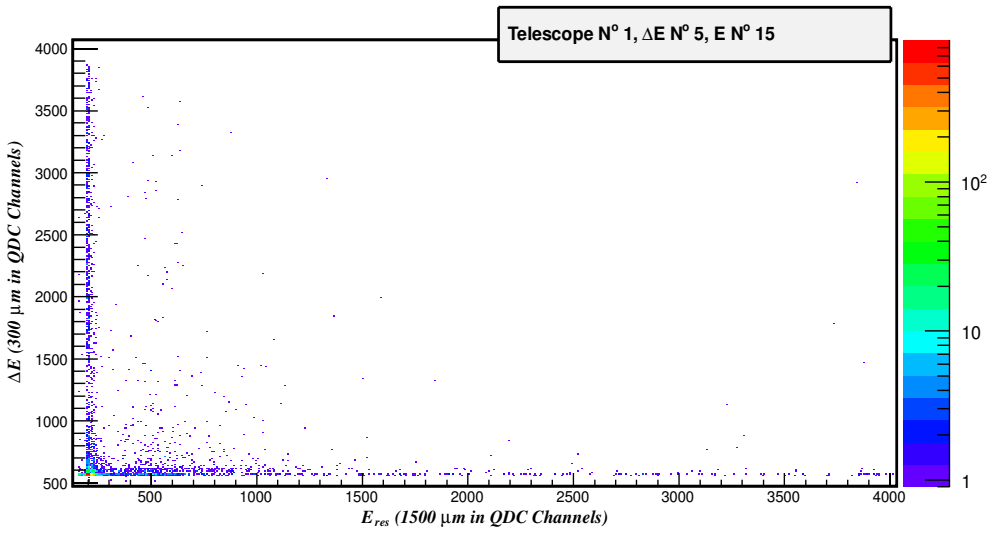

Figure 14: ΔE-E Identification matrix between the first two stage of DSSSD respectively N°5 and N°15.

In figure 14 an example an empty identification matrix evaluated between the strip number 5 of the first DSSSD stage and the strip number 15 of the second DSSSD stage is shown. In this case, evidently, no ‘’effetto calotta’’ was observed. The identification matrix showed in figure 14 is also interesting because it is possible to observe signals due to the pure electronic noise that in that matrix are mostly present within the 1200 fired QDC channel of the 1500μm of the second DSSSD stage and within the 2500 fired QDC channel of the first 300μm DSSSD stage. In Figure 15 the observed “effetto calotta” is reported in a schematic way for the purpose of further clarification of the text.

By looking the figure 15 it is clear that two particles that both pass through the first strip number 5 of the first stage of 300μm of DSSSD can pass through the second stage of 1500μm of DSSSD either through the strip geometrically correlated number 26 (that is just behind the strip number 5) or through the strip number 27 that is just close to the left (front view) with respect to the strip number 26. This means that the identification procedure become very timing

consuming because it is necessary to analyse 32 ΔE-E ordinary identification matrixes between the first two DSSSD stages, and, also, all the ΔE-E identification matrixes due to the " effetto calotta". In summary, taking into account the combinations, in total, it would be necessary to analyse 100 identification matrixes for each cluster of FARCOS array. The main source of the observed effect is due to the very close assembling of the device near the target at a distance of 40cm where strong deviation from a pure portion of a spherical configuration is expected. However, this configuration choice was adopted just to test the device under the severe limit of both geometry, high counting rate and possible small asymmetry in the beam. However, in addition to the DE-E identification matrices, it has to be noticed that, in future, we plan to identify particles also attending other techniques (that were not available in the InKiIsSy experiment, due to severe limitation of the electronics lines, available at that time) like the Pulse Shape Discrimination (PSD) in the first DSSSD stage, and the Time Of Flight (TOF) discrimination, this last not used in the InKiIsSy setup because the FARCOS array was too close to the target (40cm); consequently, the value of 1 ns of resolution (essentially due to the timing of the beam) is not enough to discriminate in mass particles using TOF in so short path of flight.

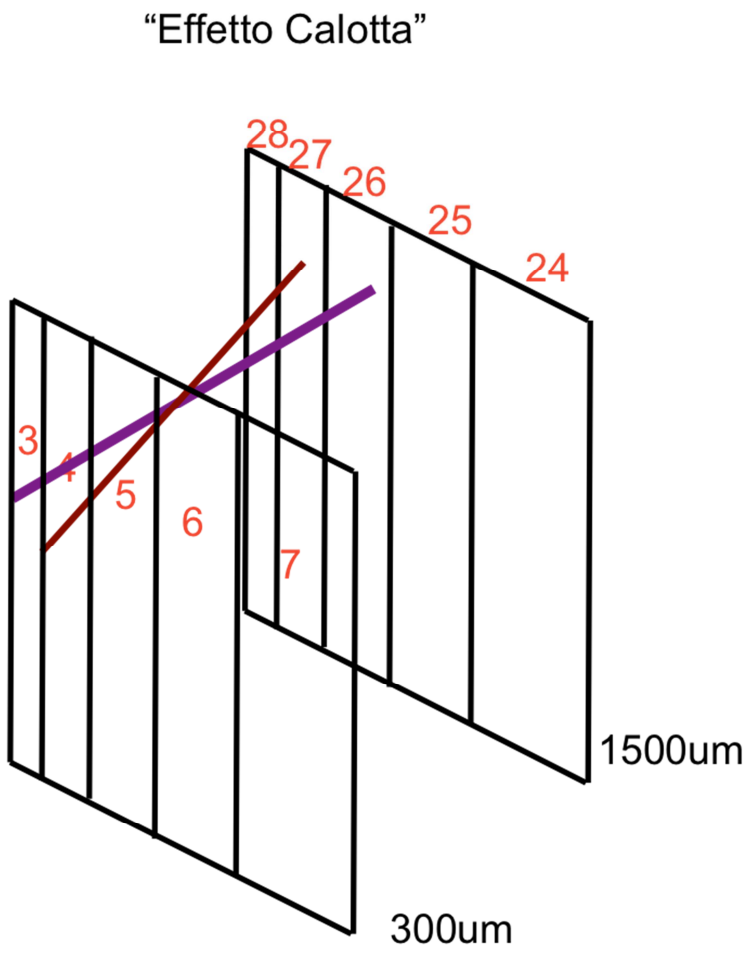

Figure 15: Schematic view of the "Effetto Calotta".

In this PhD work we also have taken in consideration the possibility to find a work procedure in order to make faster the analysis, to reduce as much as possible both time-consuming and manpower. At first, the attention was put in the identification from the first two DSSSD stages.

To achieve a satisfactory method for saving both time and manpower it was necessary to study in detail the response function of single-independent strips and a suitable ensemble of them.

As a first guess it was possible to choose two simple ways to perform the particle identification. One way was to study the particle identification by doing the analysis strip by strip (single-strip way).

Evidently, it means a time consuming identification job; indeed, as just said, if the method was extensively applied to all the strips it would require to analyse about 100 identification matrixes for each cluster and the integration of the available statistics collected by integrating (in this test) 320 runs of the experiments. Alternatively, it was possible to perform the identification by adding the statistics collected by a given number of independent strips (sum-strips way) in such a way to obtain a comparable statistics as in the single-strip way and to minimize the small intrinsic differences (thickness, active depletion, resistivity, etc.) among the independent strips. In principle it is possible to add the statistics collected of many strips in only one identification matrix because the average physical properties of each detector is practically the same (within 1% accuracy of the homogeneity). The only hypothesis is that the difference in thickness among the strips is negligible. The problem is in the fact that, each strip has an independent electronic channel so it means that it is necessary a calibration procedure in order to homogenise many strips either by an energy calibrations with particles or by a pulser calibration, or both of them.

This test analysis was performed using 320 experimental runs. In the figure 16 is shown a ΔE-E identification matrix between the strip number 8 of the first 300μm of DSSSD stage and the strip behind it, i.e., the number 23 in the secondo 1500μm of DSSSD stage. Notice that in order to compare the two working way, the two axes, the Y axis where there are signals coming from the first DSSSD stage, and the X axis where there are allocated the signals coming from the second DSSSD stage, are already calibrate in mV. In that figure, the coloured line represents the identification fits line and each one represents loci of a given atomic number of the detected particle.

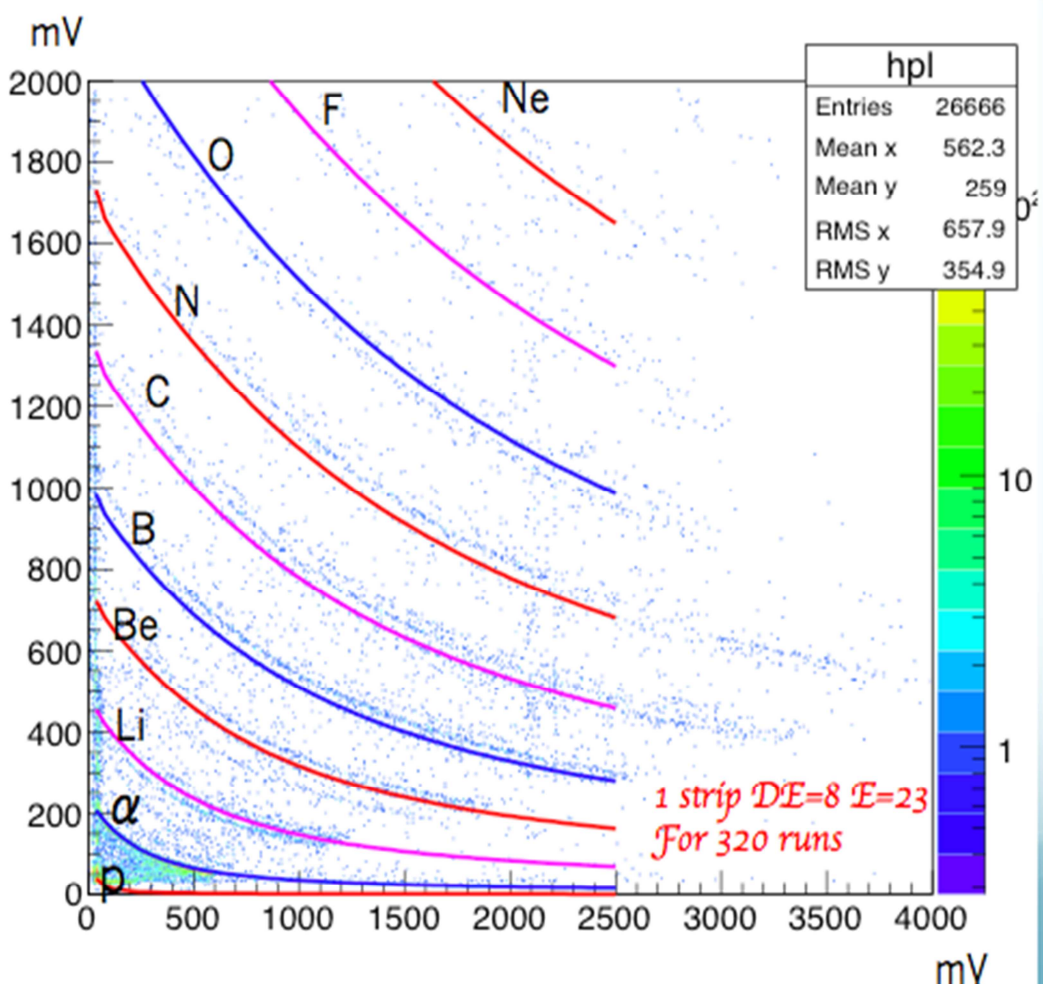

Figure 16: ΔE-E identification matrixes between 1 strip in the first stage and 1 strip in the second DSSSD stage for 320 runs after the pulser calibration in mV [EVP15].

The lines start from Hydrogen (Z=1) element up to Neon (Z=10). It is also visible in the matrix the isotope identification lines that are close to the one associated by the fits to the most abundant element. For instance, in the Beryllium, the red line represent the ^{9}Be but, they are also visible the hyperbola of the ^{7}Be and of the ^{10}Be. The same is visible for Carbon lines where the purple line is for the ^{12}C but, they are also distinguishable the ^{13}C and ^{14}C isotopes. In figure 16 is possible to observe that there are very few count for Z=1 element, and it is impossible to resolve its isotopes (proton, deuteron and triton). This is due to the fact that in the evaluation of this identification matrix it was imposed the further constraint that the particles were just stopped in the second DSSSD stage. In fact we are interested mostly

in Intermediate Mass Fragments (IMFs) with respect to all observed particles, in fact mostly of the light particles (p, d, t, 3He, …) have an energy that is sufficient to punch through both of the two stages of DSSSD (1800μm in total) and, consequently, they are stopped by the CsI(Tl) crystals. In any case, we can identify those light particles by using the PSD in the CsI(Tl) Crystals. Any loss of information is not expected.

In figure 17 is shown the ΔE-E identification matrixes also evaluated between the first two DSSSD stages (as in the figure 16), but there the statistics of 8 strips for the first 300μm DSSSD stage, from the number 8 to the number 15, and of course, 8 strips for the second 1500μm DSSSD stage, corresponding from the 16 to the 23 strip numbers, is considered.

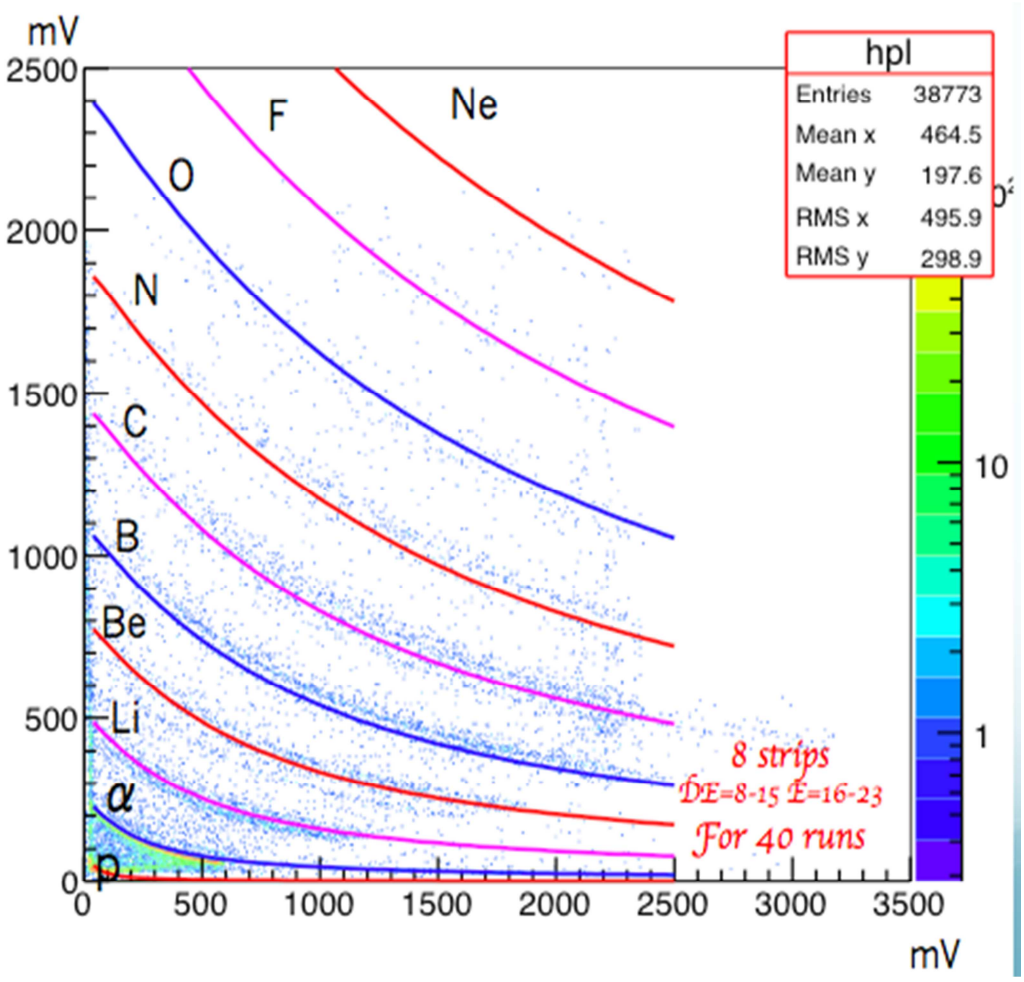

Figure 17: ΔE-E identification matrixes between 8 strips in the first stage (8-15) and 8 strips in the second DSSSD stage (16-23) for 40 runs after the pulser calibration in mV [EVP15].

In this latter identification matrix 40 experimental runs were used in order to get the same statistical significance in comparison with the previous identification matrix (see Figure 16), the latter integrated on much larger experimental runs. In fact in figure 16 there is only one strip for 320 runs and in figure 17 there are 8 strips for 40 runs. It was chosen as a simple method to have more or less the same number of particles in both identification matrixes. For both matrixes, the one in figure 16 and the other in figure 17 it is possible to take into account for similar observation and comments. The big difference that appears evident by inspecting the two identification matrixes is: in the case of

figure 17(addition of 8 strips) the isotopic resolution seems to be reduced with respect to the single-strip way (figure 16).

This aspect can be fully understood by looking the following two figures:

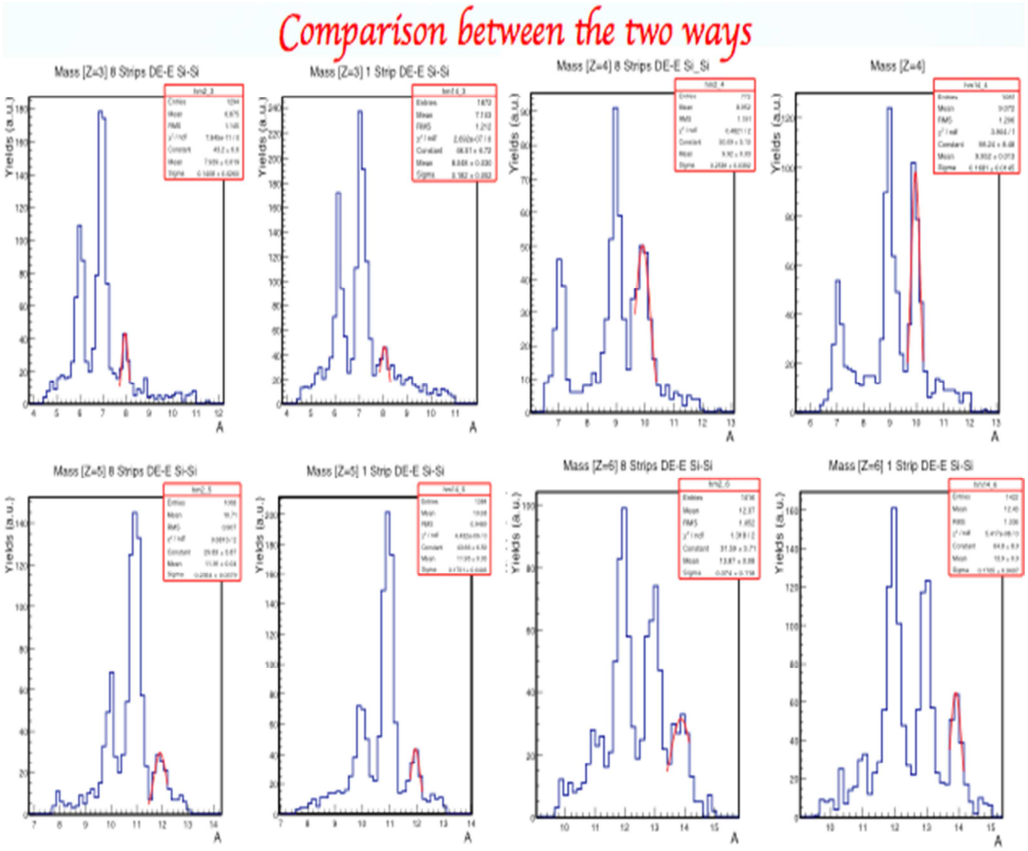

Figure 18: Comparison of the isotopic identification resolution in the two adopted identification procedures for 3≤Z≤6 [EVP15].

Figure 18 shows the comparison in the isotopic identification resolution obtained in the two ways of work for 3≤Z≤6, respectively. For the proper comparison each spectrum is labelled with the corresponding atomic number (at the bottom of each spectrum) and two of these spectra, with the same atomic number, one on the left and one of the right, represent the "sum-strips way'' (left) and the single-

strip way (right). Atomic numbers between 3 and 6 have been selected for the sake of simplicity. As it is possible to see the two isotopic resolutions are almost comparable. In fact, the isotopic identification is slightly better in the case of single-strip way, as it was expected. In contrast, in the range of atomic number 7≤Z≤10 the resolution of the isotopic identification has shown the tendency for better results in the case of one-strip way (see figure 16) than in the case of (sum-strips way) [EVP15, EVP16], as it clearly shown in figure 19.

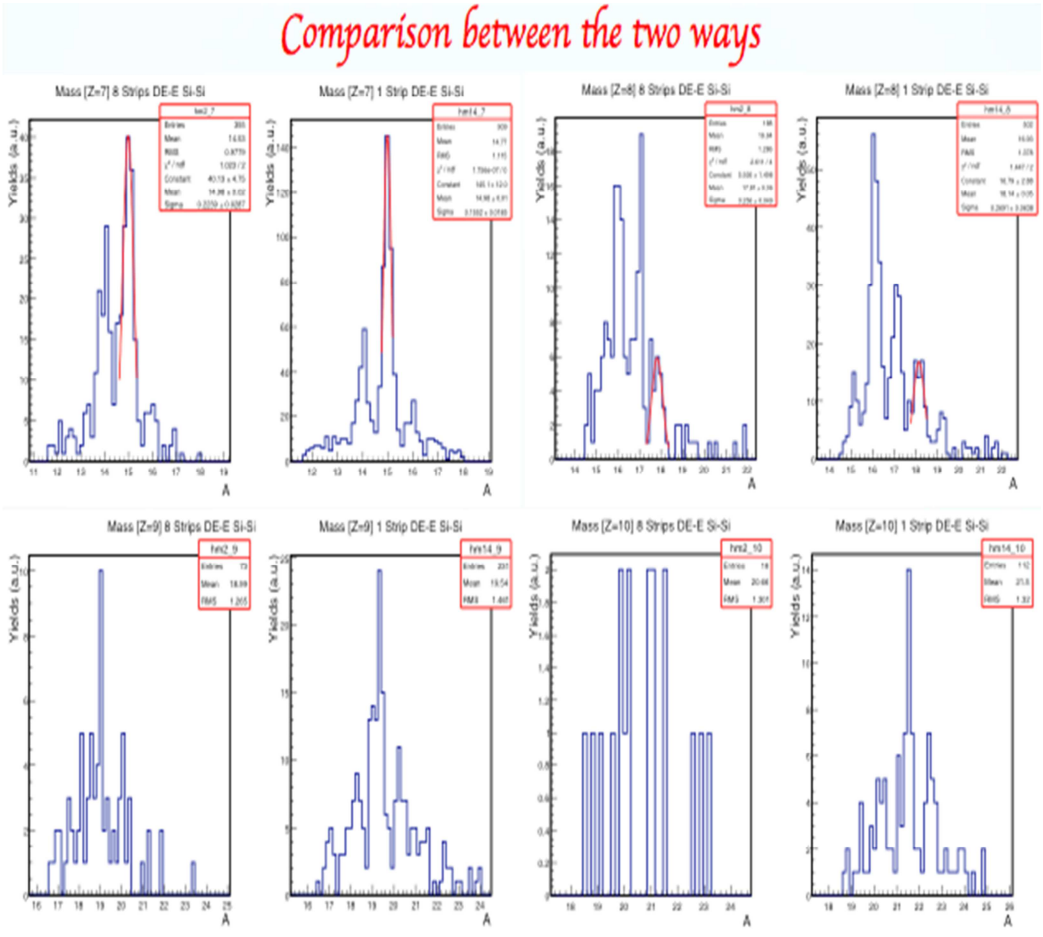

Figure 19: Comparison of the isotopic identification resolution in the two ways for 7≤Z≤10 [EVP15].

The obvious advantage of this single-strip way is to exploit the full resolving power of each cluster of the apparatus. During this experiment FARCOS array was coupled, for the first time with another apparatus, and it was also the first real experimental test of FARCOS for the purpose to study the interesting case of the IMFs emission.

With the following table 1 it is possible to summarize advantages and disadvantages of the two identification proceures.

"Single-strip way"		"sum-strips way"	
✓	✗	✓	✗
Good Isotopic Resolution Not necessary energy calibration	Long identification work (100 Matrix for each telescope, possible if we have only 4 telescopes)	Fast identification work (16 matrix for each telescope, good for 20 telescopes)	Worse isotopic identification resolution (at least for now!)
Wide identification range: 1<Z<10	Need a large statistic in each strip (0.2x4.6 cm)	Good if it is not necessary a wide identification range: 1<Z<2(3)	Necessary energy calibration (mV or better MeV
Good if the detector is near to the target (25cm)		Far to the target(0.8-1.0 m)	Good if not have large statistic

Table 1: Summary upon the comparisons of the two ways for the identification procedure between the first two stages.

Taking in to account the purpose of the InKiIsSy experiment and the fact that in that case we were using only four telescopes of FARCOS array it was decided to identify particles by the single-strip way in order to use the fully resolving power of FARCOS.

4.4 Light Charged Particles (LCPs) identification

Light particle identification procedures come principally from the de Pulse Shape Discrimination in the Caesium Iodate crystals. This is a good identification method in particular for energetic light charged particles (LCPs) like protons, deuterons, tritons, Helium and lithium isotopes. In that experiment, substantial cross section was associated with Projectile like emissions. This fact means that LCPs deposit few energy in the first two silicon strips stages while they are full stopped in the CsI(Tl) crystals.

The identification method of LCPs is based on the electronic shape analysis of the respective pulses, that for the different particles is changing by varying the particle type. In practice, the method consists in measuring the fast component of the electronic signal between 0 and 600ns and the slow component between 900ns and 6μs, in hardware way.

In the case of the InKiIsSy experiment this method was used to discriminate light particles, protons, deuterons, tritons, Helium isotopes, Lithium isotopes and ^{8}Be having enough kinetic energy to punch through the first two steps of DSSSD and to be arrested in the last CsI(Tl) stage. In figure 20 and 21 the typical identification fast/slow matrixes for the FARCOS prototype are shown. Indeed the two figures refer to the same identification matrix, in other words, they are zooms of the same identification matrix of one CsI(Tl) crystal of FARCOS, in order to show better the identification power of this technique for light particles. In both matrixes, in the X axis there is the slow component of the signal in QDC channels and in the Y axis the

fast component in QDC channels. In the X axis of the matrix in figure 20 the signal extends up to about the channel number 2300, instead the same axis in figure 21 starts from the channel 2000. How it is possible to see just inspecting the two figures, there is, for light particles, a very good isotopic identification resolution. This is due principally to the fact that the crystal was of recent manufacturing (2013) and there was no radiation damage (if any), and also because, there is a better light collection due to reduced distance from the entrance window and the Silicon Photo Diode, with respect to the CHIMERA case.

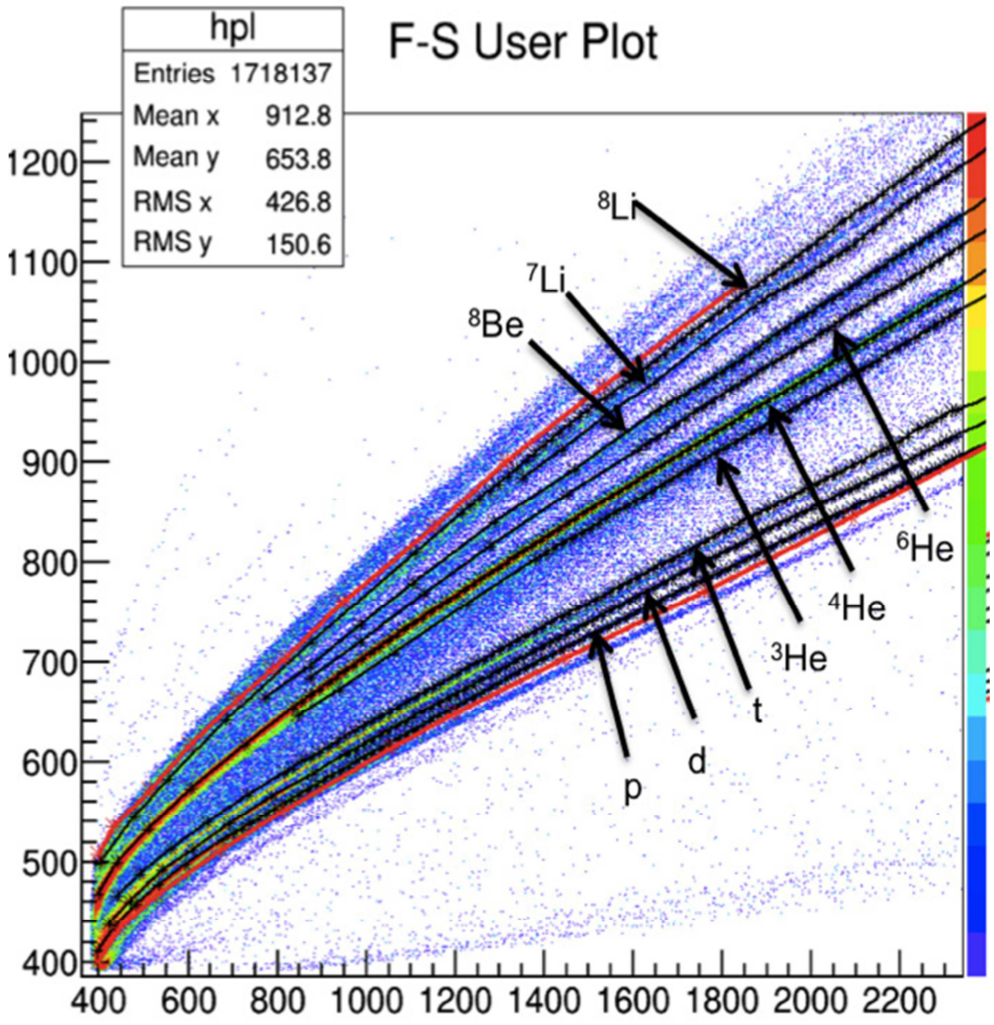

Figure 20: Typical identification matrix for the CsI(Tl) PSD (Fast/Slow) of a crystal form the telescope N°1 of FARCOS [EVP16b].

All of light particles having a sufficient energy to punch through the first two DSSSD stage (1800µm in total) are stopped in the CsI(Tl) crystals and they were very well identify with the PSD technique. The achieved high isotopic identification resolution allows to distinguish protons, deuterons, tritons, ^{3}He, ^{4}He (Alpha particles), ^{6}He, ^{7}Li, ^{8}Li until ^{8}Be, these last are on the line corresponding of the two alpha particles arriving in the same time in the crystal due to its very short half-life, $\tau \cong 6.7 \cdot 10^{-17} s$. In fact ^{8}Be is practically absent in the ΔE-E identification pattern from the first two stages.

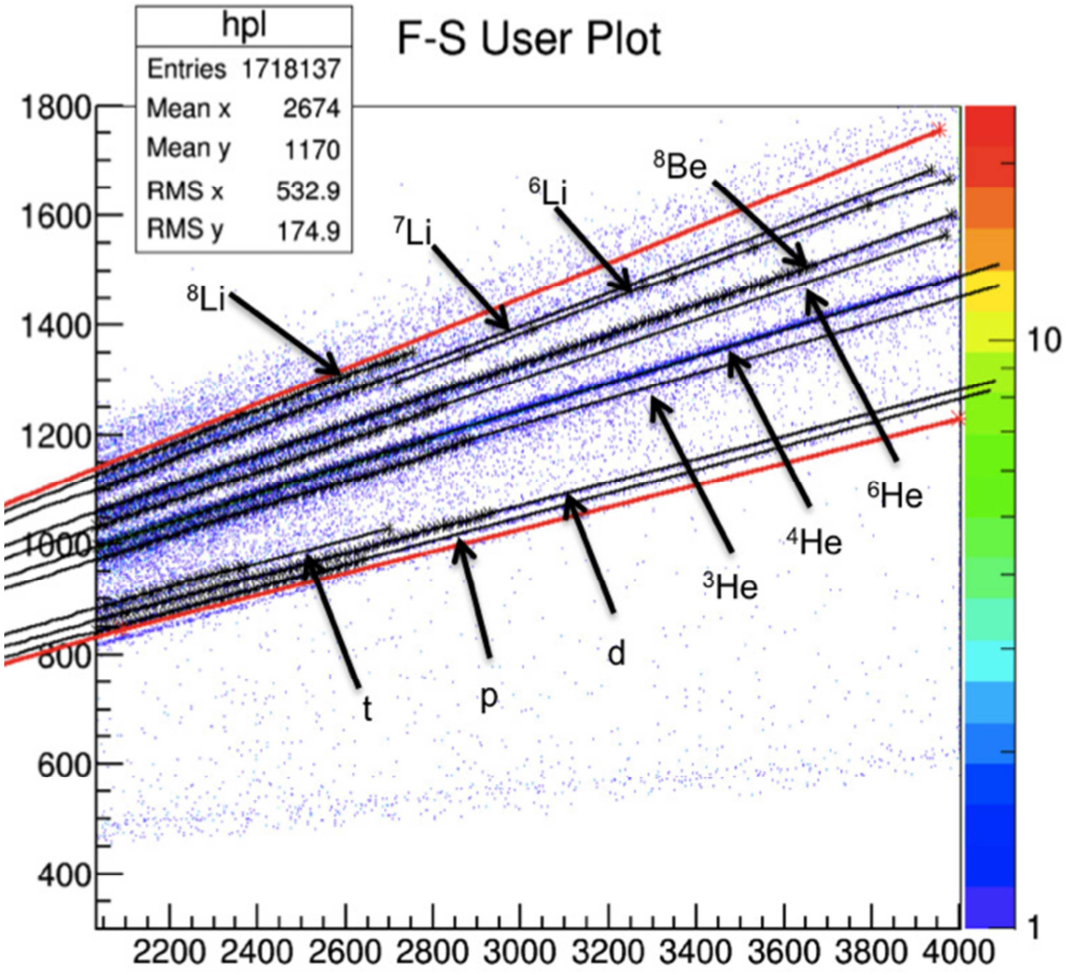

Figure 21:The second part of the same matrix figure 20 [EVP16b].

In particular, in figure 20 it is also possible to see a clear locus just below the proton's line: it is the line of Gamma rays. At the moment we are focusing the efforts in detection on charged particles but we do not exclude to work in a second step, to identify also the ϒ part of the signals [EVP16b].

4.5 A new versatile electronic: GET (General Electronic for TPC)

The GET (Generic Electronic for TPC), is an integrated system of data acquisition designed to handle a very large number of independent electronic channels (more than 30 kch). GET process starts from the analogic signals coming from the detectors and goes on towards digital acquisition and storage (DAQ). The innovative GET performances such as high versatility and compactness make the GET project also a good candidate to process signals in a detector array like FARCOS having a large number of electronic channels (132 for each cluster) in a very small volumes (about $7\times7\times10$ cm^3). In principle, this electronics could be not adapted for the purpose of FARCOS electronics. Indeed the GET system is not designed for read-out of silicon detectors, but the preliminary results of tests, still under way, supports feasibility of using get for FARCOS array. To have more definitive conclusions more testes are needed, so no definite conclusion can be given in the present work [SDL16].

GET is based on a chip, AGET, that is able to process 64 independent electronic channels with a preamplifier, a filter, a discriminator and with an array of 512 capacitors for each channel. The sampling frequency is in the range from 1 to 100 MHz. Four of this AGET are allocated on another board, called ASAD, where the signals are digitalised. Each ASAD is able to process 256 channels. These ASADs are read-out by an electronic module called CoBo that is able to collect signals from 4 ASADs (1024 chs). The CoBos are housed in a μTCA crate, allowing to allocate up to 10 CoBos, together with the MUTANT (MUltiplicity Trigger ANd Time) module that is able to synchronize different CoBos in order to manage the main-trigger. A general Data Acquisition framework can manage the data flow (event-

building, filtering, storage) coming from different CoBos and from other coupled devices and data acquisitions [POL12]. As already seen, the signals of the detectors were processed by improved versions of standard PACs in use in CHIMERA Detectors [BAS04].

The use of these preamplifiers as a primary read-out stage is necessary because the GET internal preamplifiers are design for different type of detectors systems, such as TPC. However it was possible to by pass the internal GET PACs in order to process the signal by the CIMERA PACs ones. The following figure, the figure 22, that is adapted by a courtesy of Dr. E. Pollacco, shows very schematically the architecture of the GET electronic.

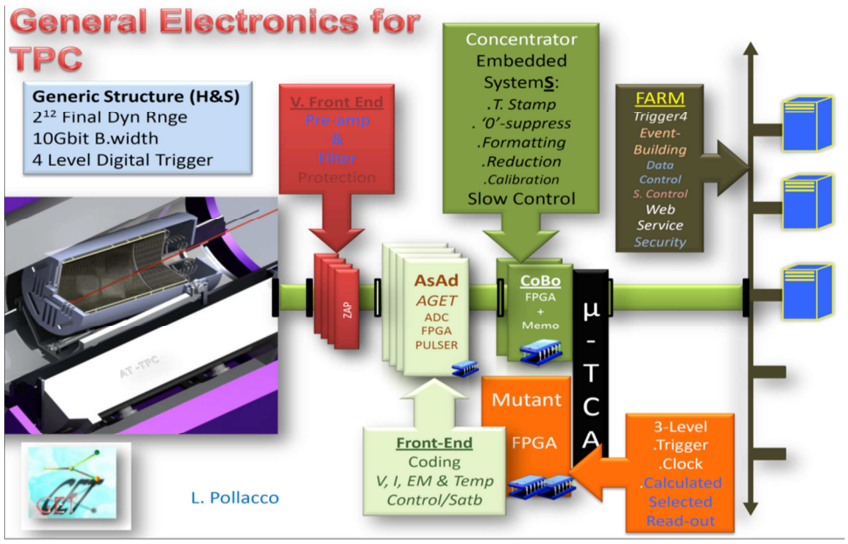

Figure 22: Schematic view of the GET electronic.

The purpose of this PHD work is beyond the purpose of explaining in details in this complicate electronic device. For more details see references [FTDR, ATDR, STDR] that are the FARCOS, ACTAR end SAMURAI TPCs design reports. The latter two are in fact gas detectors where this electronic is particularly adapted. In this work we want just to show the first tests made on the CsI(Tl) crystals and on

the Double Sided Silicon Strip Detector in order to justify its use in different types of detectors others than the ones for which GET architecture was designed.

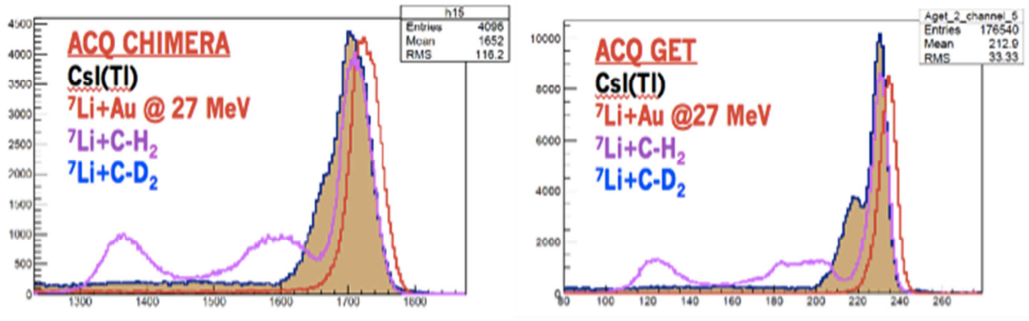

Figure 23: Comparison between CHIMERA acquisition (left panel) and GET acquisition (right panel) in the case of CsI(Tl).

Some results of the CsI(Tl) crystals tests are shown in figure 23. In this case, a Tandem beam @ INFN-LNS of Catania of ^{7}Li of a total energy of 27 MeV was used. The targets used were gold (red line), hydrogenated carbon (violet line) and deuterated carbon (blue line). The left panel corresponds to the case of standard CHIMERA data acquisition, while on the right panel the GET data acquisition is reported. Notice that, in the case of the GET data acquisition the obtained energy resolution, under the experimental conditions, was about a factor 2 better than in CHIMERA one. Of course the CsI(Tl) tested in the case of figure 23 is the same in both acquisition systems. Notice that, the observed improvement in the energy resolution of about a factor two in favour of GET should be due to the fact the in that case the electronic signal is digitalized and the off-line analysis process allows to have much more information (the full shape) instead of only two stored parameters in two QDC channel. Similar result was obtained also in the case of the DSSSD, figure 24, that for the first time was tested using a three peaks Alpha particles source (^{231}Am, ^{239}Pu, ^{244}Cm) at LNS.

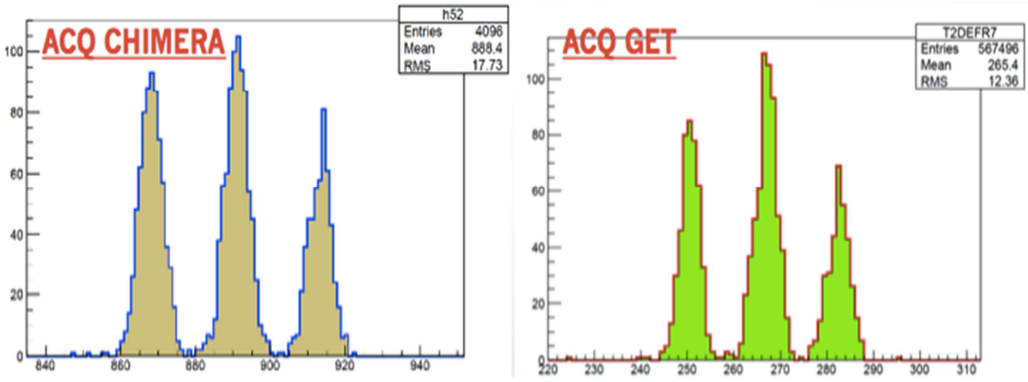

Figure 24: Comparison between CHIMERA acquisition (left panel) and GET acquisition (right panel) in the case of DSSSD test using alpha source.

Comparing the left panel (CHIMERA data acquisition) to the right panel (GET data acquisition) we conclude that the obtained energy resolution around the energy value of 5 MeV looks like almost comparable.

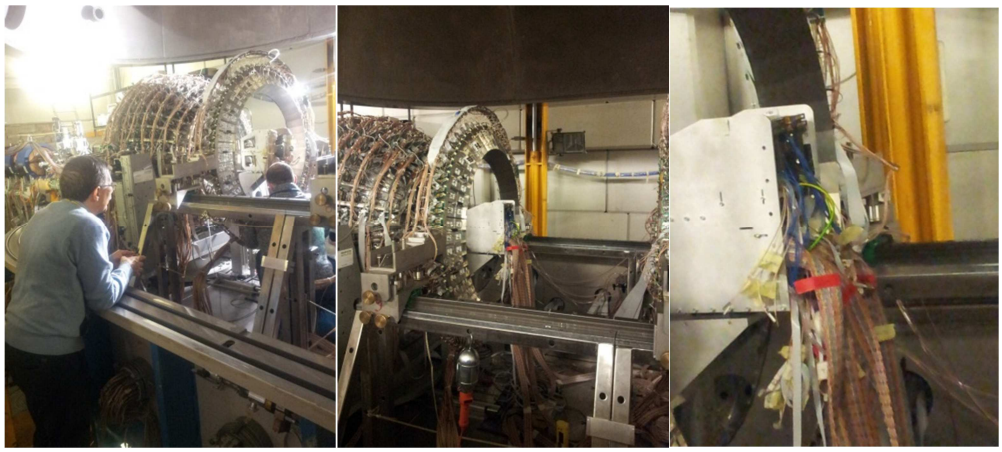

Figure 25: The CLIR experimental setup. FARCOS is positioned in the CHIMERA scattering chamber [EVP16b].

The characterization analysis continued, in particular to test the identification capabilities, during CLIR (Clustering in Light Ion Reaction) experiment performed at the Laboratori Nazionali del Sud (LNS) of INFN on March 2015 (see figure 25). In CLIR experiment

an exotic beam of ^{16}C at 40 AMeV obtained from the FRIBS (in-flight) facility of LNS on a ^{12}C target was used. With the FRIBS facility it is possible to obtain an interesting so-called "Cocktail Beams" having more than one exotic beam at the same time, allowing to perform more experiments at once. In this facility a primary beam accelerated by the superconducting cyclotron impacts to a thick target of Beryllium and produce the secondary beams that are all transported and selected in magnet rigidity along the beam lines to the the experimental halls (in this case the CHIMERA hall) in order to collide to the experimental target. Figure 26 shows the Cocktail Beams in the case of CLIR experiment where the primary beam was ^{16}O at 55 AMeV.

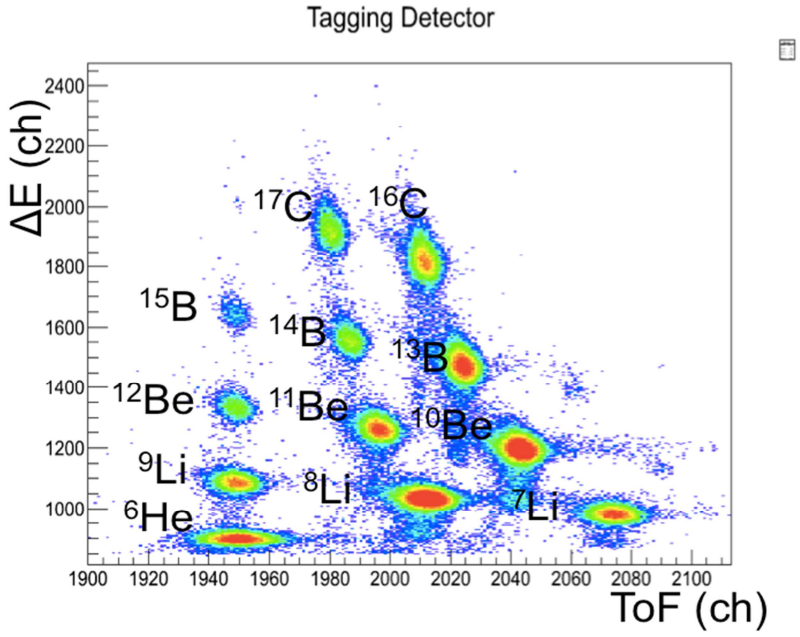

Figure 26: The so-called "Cocktail Beams" from the FRIBS facility od LNS in the case of CLIR experiment.

The matrix showed in figure 26 is obtained measuring particle energies of the beam with a DSSSD, having 32 vertical strips in the front side and 32 horizontal strips in the back side, of 140μm of thickness. The Y axis of the spectrum (in QDC channels) is the DE

signal put in correlation (event by event) with the time of flight of the beams (TOF) measured upon a base of flight of 13 m (X axis of the spectrum (TDC channels).

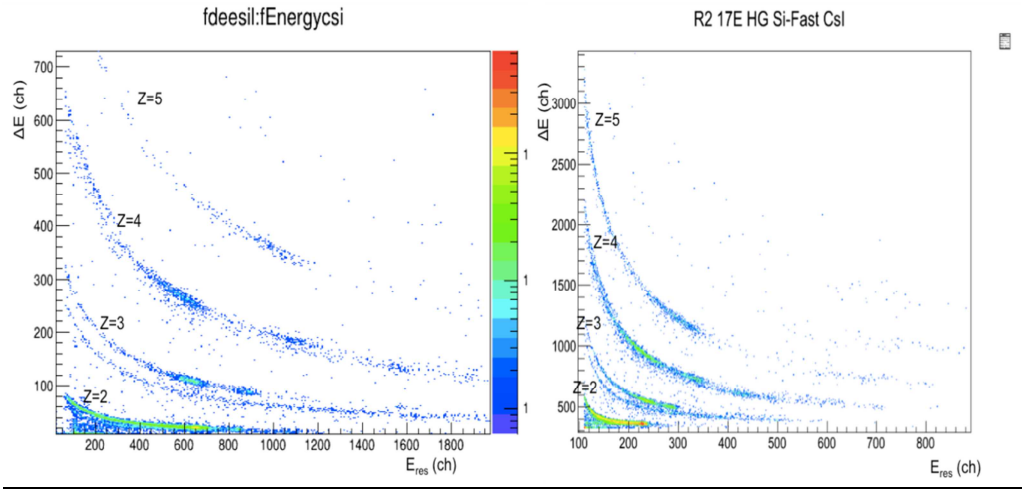

Figure 27: Comparison between two ΔE-E identification matrixes obtained in the reaction $^{16}C+^{12}C$ at 40 AMeV (CLIR experiment) from two telescopes of CHIMERA detector of the same ring 2. Left: signal processed by GET. Right: signal processed by standard CHIMERA electronic [EVP16b].

The comparison between two ΔE-E identification matrixes acquired with two telescopes of ring 2 of CHIMERA multi-detector and using the different electronics is shown in the figure 27. In the Y axis there is the energy loss in the first silicon (300μm) of CHIMERA, and in X axis the residual energy of the detected particle measured in the CsI(Tl) (12 cm) second stage, both in arbitrary units. As it is possible to see the two matrixes show both a good comparable isotopic identification resolution. It means that the GET electronics is working quite good not only for CsI(Tl) crystals but also for silicon detectors [EVP16b].

4.6 Milestones and cost evaluation

Due to both economic problems and the need of some technical developments, the construction of FARCOS correlator will be distributed in almost 5 years. In particular we need a proper time to fully develop the ASIC preamplifiers (under test and construction) to allow for the compact highly integrated structure pencilled above and to decrease the needs for the cooling system. Another module that needs a proper time for its development, is the Dual Gain module (under construction by Dott. G. Saccà from INFN Sezione di Catania) that is necessary to match the needed for a wide dynamical range. In table 2 the milestones of the experiment (2016) are reported.

year	Operation
2015	test acq get for FARCOS - construction of 2 telescopes
	purchase of get electronics - test prototype asic preamplifier - test dual gain module
2016	construction of 6 new telescopes - study of alignment system - new batch asic preamplifier
2017	construction of 4 new telescopes - final design modular support - new batch asic preamplifier
2018	construction of the last 4 telescopes
2019	reworking or substitution if damaged of silicon strip with old kapton connector

Table 2: Milestones of FARCOS construction.

At the time of the writing of the present work, we already have Silicon and CsI(Tl) detectors for 6 complete telescopes. They were purchased using funds from EXOCHIM experiment and a PRIN project of the Minister of the Research and University (under the responsibility of Prof. Giuseppe Politi from Catania University). The cost of such detectors is not included in the present evaluation. In table 3 we list the cost predictions tax included (22%).

Task	number	Cost (no tax)	Cost (tax incl)	year
14+2 spare Si300 µm	16,0	5,0	97,6	2016-2019
14+2spareSi1500 µm	16,0	7,5	146,4	2016-2019
64 CsI(Tl) + 4 spare	60,0	1,0	72,8	2016-2019
Crate µTCA	1,0	8,6	10,5	2016
16+2spareASAD	18,0	4,5	98,8	2015-2016
4COBO+1 spare	5,0	6,5	39,7	2015
1Mutant+software	1,0	26,5	32,3	2015
Power supply HV/LV	1,0	25,0	30,5	2015-2018
Cable - flanges – dualgain	1,0	82,0	100,0	2015-2018
mechanics	1,0	41,0	50,0	2015-2018
preamplifiers	1,0	90,0	109,8	2015-2018
Farm-diskserver-online analysis	1,0	82,0	100,0	2015-2018
contingency	1,0	60,0	73,2	2015-2018
Total			961,7	

Table 3: Cost predictions in k€.

5. Future perspectives: Neutron Detection

The possibility to provide devices for simultaneous detection of charged particles and neutrons, that is enough flexible to be coupled to 4π detector to measure also global variable having signature of neutron signals, is an important challenge for the next future. The neutrons signal plays an important role in all of the physics cases in the energy domain of interest in this PhD work. Evidently, in correlation functions studies, neutrons also can play an important role in order to have information on the asymmetry term of EOS of the nuclear matter, especially in the field of exotic nuclei.

For instance, in figure 1 are shows n-n, p-p and n-p correlation function calculated with BUU theoretical model as a function of the gamma parameter of the symmetry energy and as a function of total momentum of the considered pair of particles. In that work the authors show that proton and neutron coming from the pre-equilibrium phase in central collision, in figure 1 panel (d), (e) and (f), are very sensitive to the symmetry energy [CHE03].

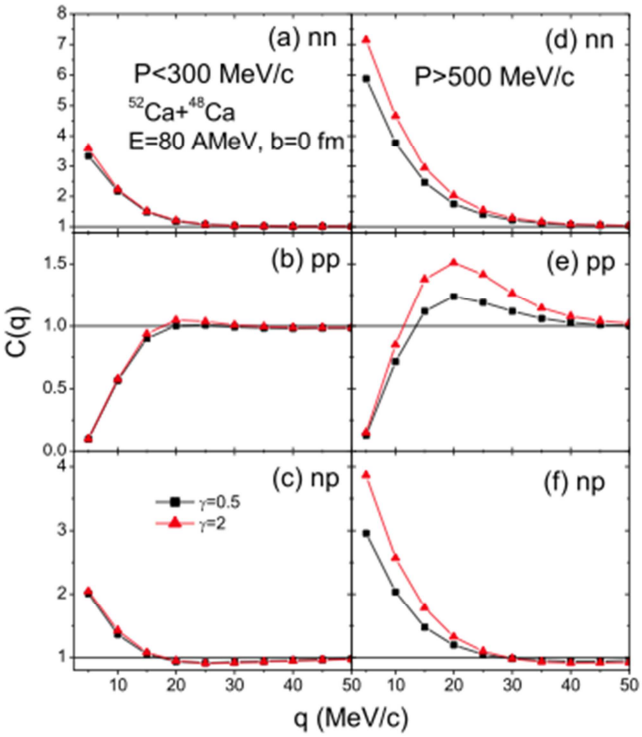

Figure 1: (color line). Two-nucleon correlation functions gated on the total momentum of nucleon pairs. Adapted from [CHE03].

In this case, neutron detection can contribute efficiently to solve the problem of the important role of the final state interaction (present for example in the p-p correlation function) by measuring the two-neutron correlation function [GEL99]. In fact during the last two decades nuclear interferometry has become an important tool for understanding not only emission time and source size in a nuclear reaction [KOO77, PRA87, BOA90, VER06] but also to pin down phase-time characteristics of the emission source [GON93, HAN95, MAR95, ARD97, DEY97, DEY00]. Such information contributes to constrain the theoretical models [GHE01]. Simultaneous measurement of n-n, p-p and p-n correlation functions open new interesting possibilities to characterize the emitting source, since quantum statistical and final state effects contribute differently to the different correlations, making easier the analysis of the different effects [GHE93, CRO93, GHE00].

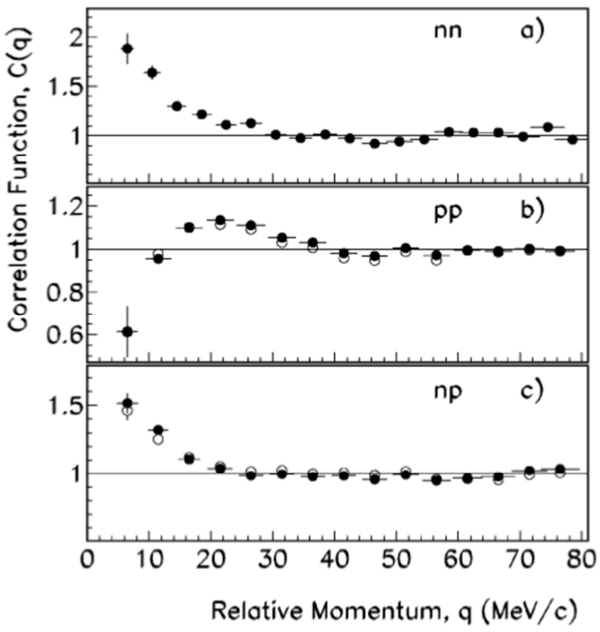

Figure 2: a) Two-neutron correlation function; b) two-proton correlation function; c) n-p correlation function. In b) and c) there is also the comparison with the "event-mixing" technique (open circles) and the "single-product" technique (black dots). Adapted from [GHE00].

In figure 2, examples of n-n, p-p and n-p correlation functions in a specific experiment aimed to study the characteristics of the emitting source are shown [GHE00].

As already penciled in previous chapters, two-particles interferometry in nuclear physics is a well established and powerful experimental procedure to determine the space-time extent of the particle emitting source [BOA90, ARD97]. While at relativistic energies the emission time is negligible and information on the spatial size is obtained with minor ambiguity, at lower energies only the convolution of space time information is obtained, which can be disentangled by means of stringent analysis not easy to do, e.g., directional analysis [PRA78] as already seen in chapter 2. In intermediate energies domain, the extraction of the space-time properties of the emitting source is further complicated by the competition of two effects; one is the presence of multiple sources of particle emission [LAR97, LUK97, DOR00, LEF00, LAN01], another one is the different time scale of statistical

and dynamical emission from equilibrated and non-equilibrated sources [GON90, HAN95b, VER02]. Furthermore, correlations between non-identical particles provide information about the order of particles emission that is sensitive to the details on the reaction mechanism [GEL95, LED96, VOL97 KOT99, GOU00, VER07]. Knowing the emission time sequence of neutrons, protons, and light charged particles can also contribute to the understanding of the nuclear effective interaction and the properties of nuclear matter [SOB97, BAR02, GHE01b, GHE03b].

5.1 EJ-299-33 Plastic scintillator: Tests with source

From the experimental point of view it is important to select tools that can provide not only the neutron multiplicity, but also the neutron energy spectra in an event by event mode, with the highest possible detection efficiency. For this purpose a preliminary study has been performed in this direction and main focused to a new organic plastic scintillator that seems to be very promising for our purposes [POZ13, CES14, LAW14].

The EJ-299-33 pulse-shape discriminating (PSD) plastic scintillator is a detector that enables the separation of gamma and fast neutron signals (in fact by proton detection mainly) on the basis of their timing characteristics using conventional PSD electronics systems [CES14]. Its principal characteristic is summarized in figure 3. [ELJTE]

PROPERTIES	EJ-299-33A EJ-299-34
Light Output (% Anthracene)	56
Scintillation Efficiency (photons/1 MeV e^-)	8,600
Wavelength of Maximum Emission (nm)	420
No. of H Atoms per cm^3 ($x10^{22}$)	4.36
No. of C Atoms per cm^3 ($x10^{22}$)	4.84
No. of Electrons per cm^3 ($x10^{23}$)	3.46
Density (g/cm^3)	1.08
Approx. Mean Decay Times of First 3 Components (ns)	
Gamma Excitation	13, 35, 270
Neutron Excitation	13, 50, 460

Figure 3: Principal properties of the plastic scintillator [ELJTE].

In figure 4 the emission spectrum of the plastic scintillator is shown [ELJTE].

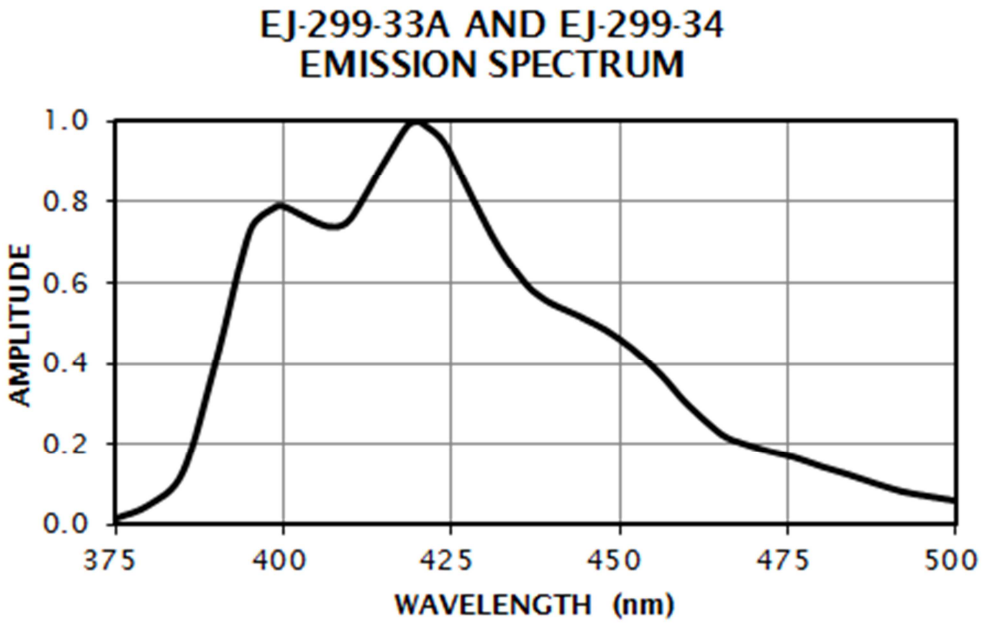

Figure 4: Emission spectrum of the EJ299-33 [ELJTE].

The EJ-299-33 plastic scintillator is produced at the moment by the Eljen Technology and it is possible to have them easily in two geometrical configurations, cylindrical or parallelepiped (see figure 5).

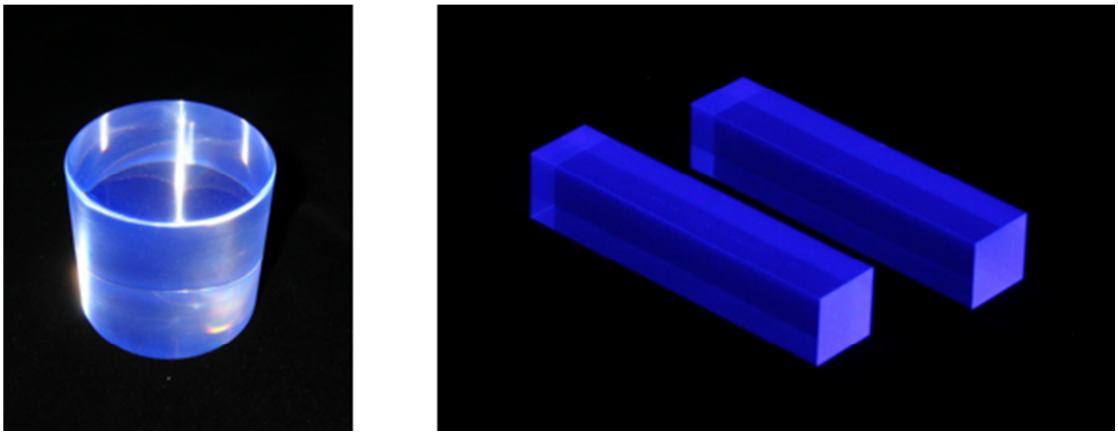

Figure 5: Geometrical configuration of the EJ-299-33 [ELJTE].

This detector was recently tested at LNS with a ^{12}C beam at 20 AMeV delivered by the LNS-superconducting cyclotron in collaboration with the Rochester (USA) group, and the main results are shown in

reference [NYI13]. The principal purpose was to test its capability in charged particles detection and discrimination.

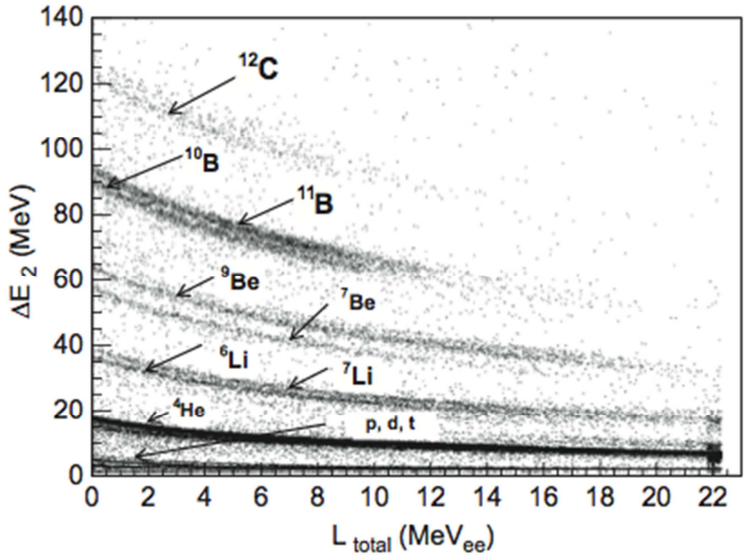

Figure 6: Particle identification patterns for 11 isotopes ranging from hydrogen to carbon. Plotted is the total light output in units of electron-equivalent MeV (abscissa) and the energy lost by the particle in the first transmission silicon detector ΔE (ordinate) adapted from [NYI13].

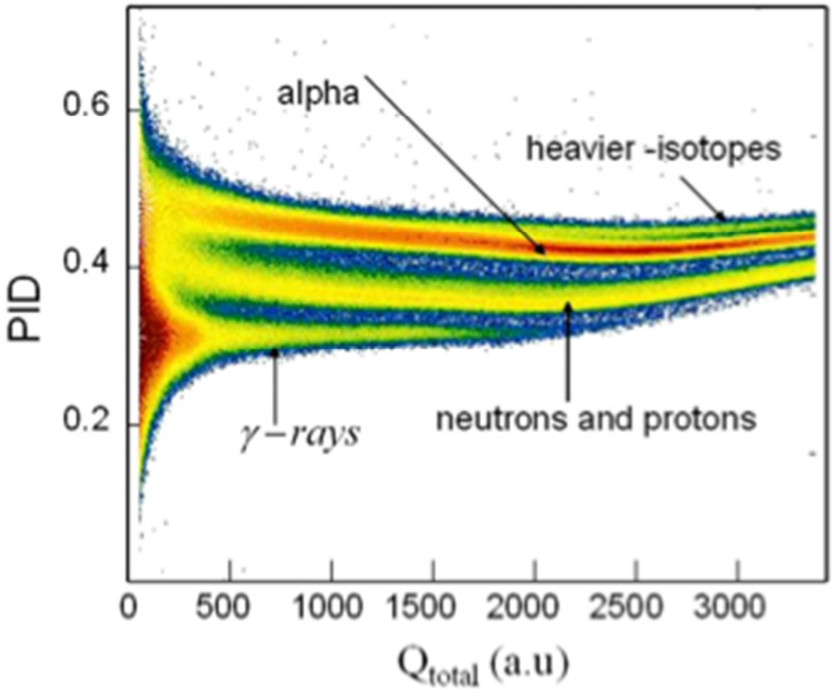

Figure 7: Pulse shape discrimination pattern for γ-rays, protons, α-particles and heavier fragments obtained using a conventional two-gate, two-channel QDC measurement as applied to the anode signals of the EJ 299-33 scintillation detector. Plotted on the ordinate axis is the PID signal derived from the two portions of the charge, total and tail, extracted from the anode of the EJ 299-33 detector assembly. Adapted from [NYI13].

The figure 6 and 7, the charged particles and γ-rays detected with the

EJ-299-33 during the test-experiment are shown. In that test-experiment the plastic scintillator was optically coupled to the photocathode of a Hamamatsu R7724 photomultiplier tube of spectral response range from 300 to 650nm, all operated under high vacuum. The photomultiplier tube was operated at 1.4 kV of anode voltage. The obtained results were very satisfactory.

After these tests, a new series of experiments where undertaken.

In the following, several tests aimed by the purpose to investigate the neutron discrimination from gamma and charged particles in experiments detection using alpha, gamma and neutron sources, are described.

Also in these cases the plastic was optically coupled with a photomultiplier operated at 1.7 kV of anode voltage and quartz window of the type EMI-9954QA, already used in the past to read out BaF2 inorganic scintillators [DEF94, LAN97]; these tests were performed in different configuration inside the CHIMERA scattering chamber as it is shown in figure 8 and 9.

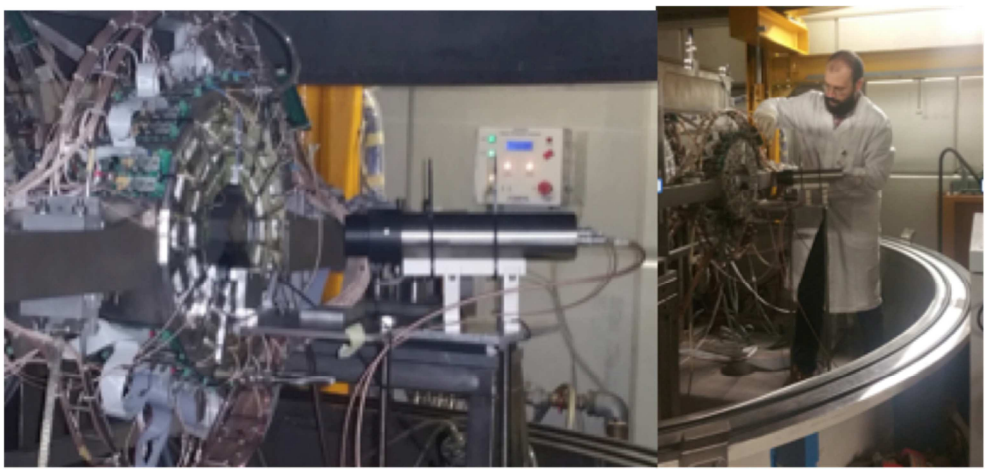

Figure 8: test of the EJ-299-33 close to the first ring of CHIMERA detector.

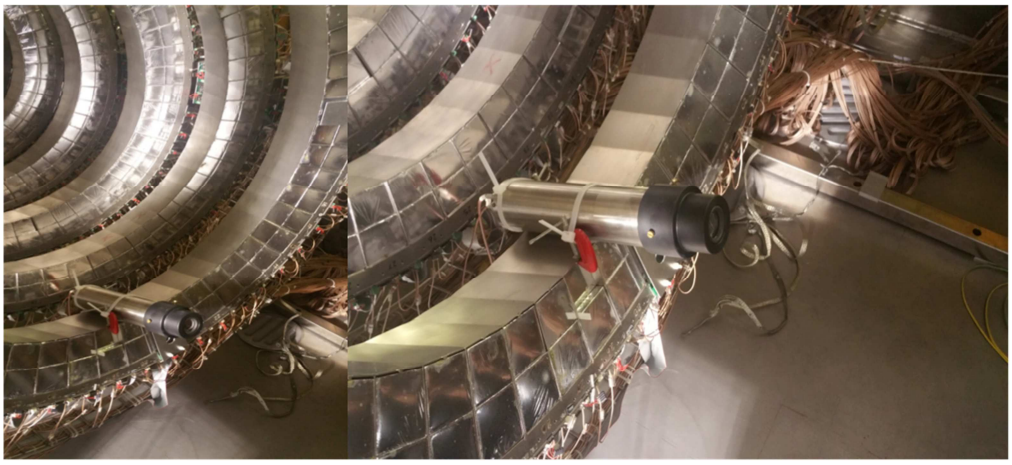

Figure 9: test of the EJ-299-33 close to the sphere of the CHIMERA detector.

As already said, for the tests were used different neutron-source, γ-source and alpha-source. Radioactive sources used in the tests are:

1) γ -Source of ^{60}Co:

$$^{60}_{27}Co \rightarrow ^{60}_{28}Ni + e^{-} + \bar{\nu} + \gamma$$

the energy of the γ rays has two peaks one at $E_\gamma = 1173\ KeV$ and one at $E_\gamma = 1332\ KeV$. The γ are emitted in all of the solid angle.

2) α-Source of ^{241}Am:

$$^{241}_{95}Am \rightarrow ^{237}_{93}Np + \alpha + \gamma$$

the energy of the alpha emitted particles is 5.48 MeV, $E_\gamma = 33\ KeV$.

3) α-Source of ^{232}Th:

$$^{232}_{90}Th \rightarrow ^{228}_{88}Ra + \alpha + \gamma$$

the energy of the alpha is 4.084 MeV, $E_\gamma = 1.3\ KeV$.

4) n, γ -Source of Am-Be:

$$^{241}_{95}Am + ^{9}_{4}Be \rightarrow ^{237}_{93}Np + \alpha + ^{9}_{4}Be \rightarrow ^{237}_{93}Np + ^{12}_{6}C + n + 5.71MeV$$

the excess energy of 5.71 MeV comes from Carbon exited levels and its de-excitation. The energy spectrum of the neutrons is shown in figure 10.

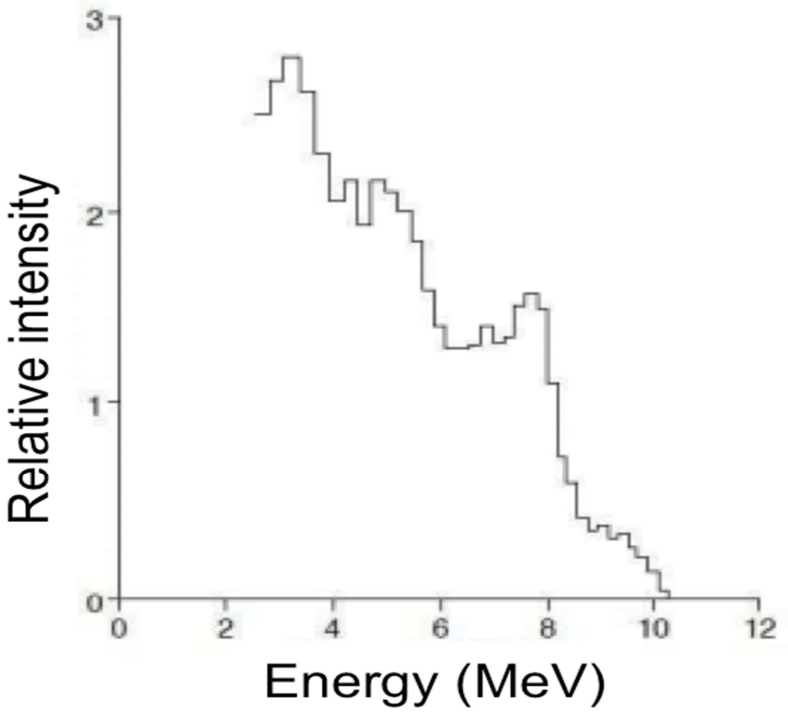

Figure 10: Am-Be neutron source spectrum.

In the following figures are presented the preliminary results of the tests.

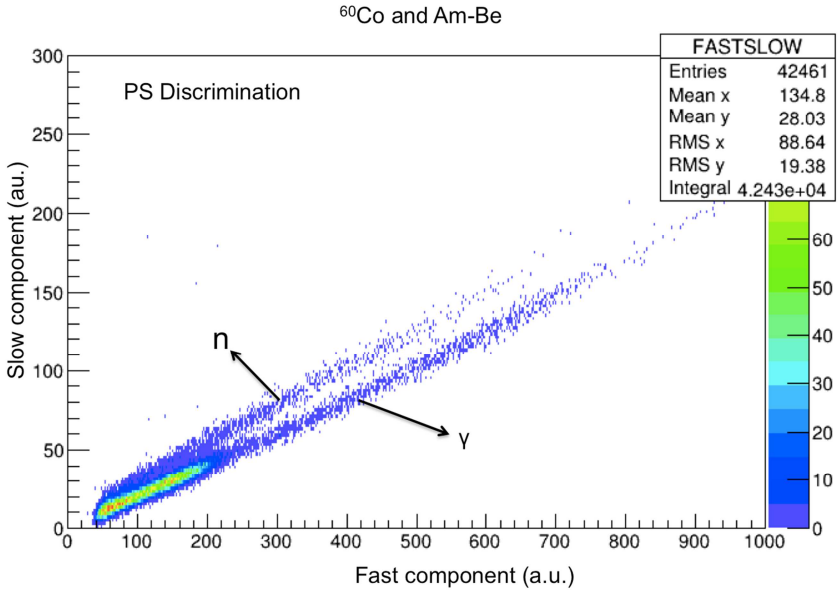

Figure 11: PSD discrimination matrix of the EJ-299-33 using at the same time ^{60}C and Am-Be sources.

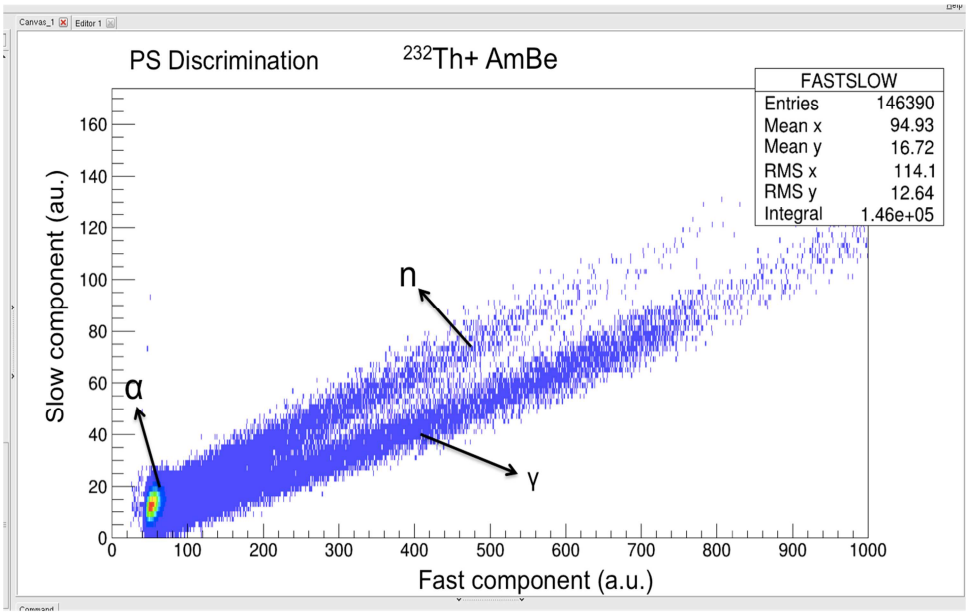

Figure 12: PSD discrimination matrix of the EJ-299-33 using at the same time ^{232}Th and Am-Be sources.

It is important to note that the spectra shown in figure 11 and 12 are collected using the GET digital electronic (see chapter 4). Because the sources, evidently, do not emit protons, in the figure 11 and 12 we have labelled the recoil protons coming from the interactions between neutrons and the hydrogen or carbon elements in the scintillator material as ‘’neutron’’. In figure 11 is it possible to see the good separation between neutron (proton) and gamma rays and in figure 12 there is also reported the signal of the alpha particles collection al lowest channels. These are only preliminary tests and the analysis data will continue also in order to characterize not only the plastic scintillator but also the GET digital acquisition. Our future goal will be to try to have an optical coupling with a Silicon photodiode in order to make this detector more manageable and versatile. In fact, for these latter achievements we need to careful study the coupling of the plastic with a wave length shifter in order to match the emission frequency of the plastic scintillator [see figure 4] with the absorption frequency of a typical Si photodiode, that is ~550 nm (one possibility

under study is the use of the plastic EJ-280, see figure 13).

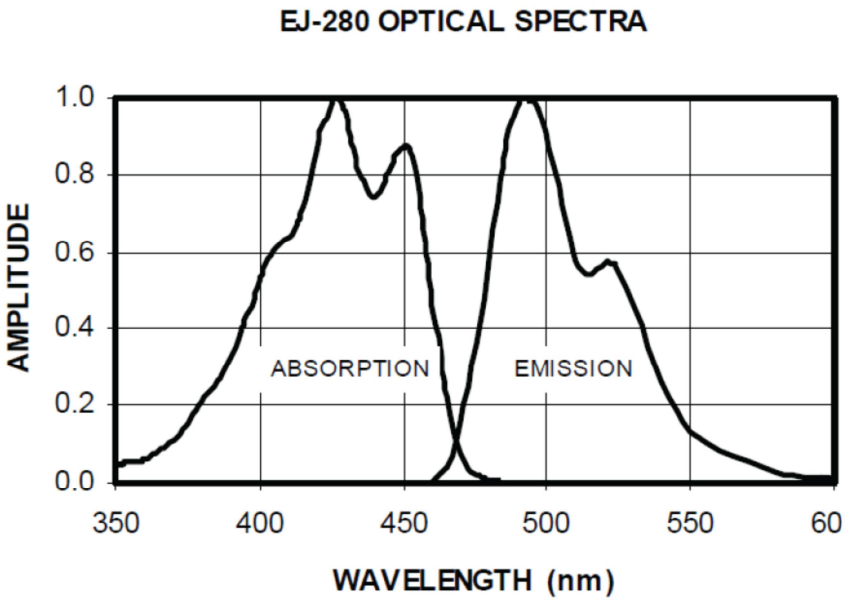

Figure 13: EJ-280 optical spectrum useful for wave length shifter.

Besides the photodiode, we also envisage to use as transductor for read out other available fast devices like Silicon photomultiplier devices (SiPM) [PAPP14].

6. Conclusions

In this thesis different aspects of my PhD work have been described. The work, in agreement with the scientific project submitted by myself to the evaluation committee of the XXVIII PhD cycle on 2012, was motivated by the study, design and construction of the new device FARCOS, whose Technical Design Review [FTDR] was submitted on 2014 and approved by INFN. The TDR includes some contributions of this PhD work. Some crucial tests of the first FARCOS prototype detector array are reported in this work. The prototype has shown good performances in the first crucial in beam tests performed at LNS: good discrimination capabilities in the mass range from light particles to Intermediate Mass Fragments, good angular and energy resolution and good isotopic identification resolution. Due to its compact configuration, it appears to be a very promising device to be coupled to 4π detectors in order to select different reactions mechanism in HI collisions at Fermi energy, from peripheral to central ones. Moreover, its flexibility and compactness allows to move it from LNS to other laboratories (LNL, GANIL, GSI,..), according with our future scientific proposals, to be coupled with different detectors, covering large solid angles. The full configuration of FARCOS will be made by 20 clusters of telescopes (in its final configuration 2018-2019) with an integrated and reconfigurable electronic. Its read-out will be based on ASIC chips equipped directly on a board close to the detectors (under vacuum) and by a digitalized acquisition system based on the GET electronic, that is under full test. Progresses in the understanding of the FARCOS characteristics have been presented, in the frame of this PhD Thesis, in many workshops and conferences. It is also under study (very preliminary) the possibility to couple FARCOS with a flexible neutron detector device essentially based on fast plastic

scintillators (to maintain good timing performances) in order to detect, beside charged particles, also neutrons. In this work some studies (preliminary) were already performed, essentially aimed to test the fast EJ-299-33 plastic scintillator. One hopes to enrich the experimental tool in order to extend the studies on the reaction mechanism to physics cases where neutron detection are expected to be an essential ingredient of the analysis. One of this cases is the study of the symmetry energy in the region of exotic nuclei that are obtained with both ISOL method (LNL, SPIRAL2) and In-Flight method (LNS, GSI-FAIR). In order to progress in correlation studies that are relevant for the FARCOS + CHIMERA coupling, the intensity interferometry method, the so called HBT method, was applied as a new analysis tool on Intermediate Mass Fragment (IMF) correlation, that was aimed in studying the specific case of the ''dynamical fission'', a nuclear phenomenon that is at the frontiers between the ''equilibrated fission'' process and the dynamical neck one. Both of them are well established phenomena in the region of Fermi energy domain. In particular, on one hand, the method was applied in order to characterize the shape of the correlation as a function of the fission asymmetry and, on the other hand, to make a time scale ''calibration'' of the IMF-IMF correlation function, by fixing the size of the emission source, based on previous well understood results obtained either with CHIMERA or other devices. For this reason it was chosen to re-examine for the first time by using the above mentioned independent analysis, ''old'' published data related to the physics case of the so-called dynamical fission of the Projectile-Like Fragment in the inverse kinematic reactions in the neutron-rich system ^{124}Sn+^{64}Ni at 35 AMeV obtained with CHIMERA at LNS. Evidently, the choice of the system, of the apparatus and the data is the most appropriate one, in view of the privileged role played

by CHIMERA as the main multiplicity selector in CHIMERA-FARCOS coupling. By applying the intensity interferometry IMF-IMF correlation function, it was shown (I hope in a convincing way) that it is possible to distinguish between a dynamical process and a statistical one not only by inspecting the differences in the intensity of the correlation functions as a function of the fission-like fragment emissions mass asymmetry, but ,also, by studying and characterizing the full shape of the correlation. Furthermore by comparing the obtained correlations with transport theoretical models (as the one adopted in this work, i.e., the CoMQD-II, developed in Catania) it was possible to pin down the time-scale of the most symmetric mass splitting of the fission process (~ 600fm/c). At moment, due to the very time consuming calculations required by the low probability associated with the asymmetric mass splitting of the fission-like process, no accurate comparisons between data (of high statistics) and simulations (of very limited statistics) were possible within the time constraints of the present PhD work. However more extensive calculations have been started in order to improve the statistics of the simulations. It is argued that more investigations are needed both on the experimental side and theoretical one. It is also of high priority, for the follow on of the present analysis, to make extensive comparisons with other transport theoretical models by using different dynamical approaches like BUU, SBNV (the one, for example developed also in Catania, that was already adopted in describing light fragments $Z<10$, see chapter 2). Of course, this PhD work represents a necessary and essential work in order to apply the intensity interferometry method to others physics cases (on both central and semi-peripheral collisions) and to different and more recent experiments, like the InKiIsSy one, performed at Laboratori Nazionali del Sud of INFN in 2013. The

present PhD work opens new perspectives in the contest of the physics of multifragmentation and related topics. In particular, following the conclusions of this thesis, a new experiment, ''CHIFAR'', has been submitted on the last November 2016 to the PAC LNS Advisor Committee. CHIFAR (CHIMERA and FARCOS) was approved with highest priority A. Spokespersons of the proposal are myself, Dr. Enrico De Filippo and Dr. Paolo Russotto, both co-tutors of this PhD thesis.

ACKNOWLEDGEMENTS

I would like to thank Dr. Paolo Russotto for his guidance, friendship, help and endless patience especially for its expertise in data analysis and programming and for introducing me in the physics cases of both the dynamical fission and the symmetry energy.

Thanks also to Dr. Enrico De Filippo for valuable help and stimulating discussions.

After, I would like to thank Prof. Francesca Rizzo, for her support, tutoring and for her advices both for physics and for life.

I'm also grateful to all the EXOCHIM/NEWCHIM research group, and especially to the national leaders, Dr. Giuseppe Cardella and Dr. Sara Pirrone, for the opportunity to making me always feel part of a big family, and giving me also warnings if necessary.

Thanks are also due to Dr. Giuseppe Verde for introducing me to the intensity interferometry and correlation functions methods and to Dr. Massimo Papa for the evaluable discussion about CoMD-II code.

It was also a real pleasure for me to meet Prof. Giacomo Cuttone, Director of LNS-INFN and his staff, for their kind and friendly assistance.

I also want to thanks Prof. Franco Riggi, coordinator of my PhD XXVIII cycle, for his great availability in solving the various problems that often occur to PhD students.

I want to thank also Dr. Gianluca Santagati to sharing with me coffee and tea.

A special thanks to my family, my mother Rosetta, my sister Grazia and my father Angelo. In particular I want to thank Angelo to his friendship, for his support, for is supervision, for the evaluable discussions about all the foundations of physics and economic issues, for stimulating my interest in science since I was child.

Finally I want to thanks, my wife, Elisa, to her extra-ordinary support, for sharing with me the pleasure in growing two wonderful little baby girls, Greta and Alice.

BIBLIOGRAPHY

[ACO12] L. Acosta et. al., EPJ Web of Conferences 31 00035 (2012).

[ACO16] L. Acosta, et al., Journ. of Phys.: Conf. Seies 730 (2016) 012001.

[AIC91] J.Aichelin, Phys. Rep. 202, 233(1991).

[ALB85] S. Albergo et al., Nuovo Cimento A89 (1985).

[ARD97] D. Ardouin, Int. J Mod. Phys. E 6, 391 (1997).

[ATDR] G. Grinyer et al., ACTAR TPC design report, GANIL 2013 http://pro.ganil-spiral2.eu/laboratory/detectors/actat-tpc/docs/actar-tpc-conceptual-design-report.

[AUD15] L. Audutore, et al., EPJ Web of Conference 88, 01001 (2015).

[BAC95] O. Bacri et al., Phys. Lett. B 353, 27 (1995).

[BAL16] R. Bale, et al. PRC 93, 054908 (2016).

[BAR02] V. Baran et al., Nucl Phys. A703, 603 (2002).

[BAR05] V. Baran et al., Phys. Rev. C 72, 064620 (2005).

[BARR97] J. Barrette, et al., Phys. Rev. Lett. 78 (1997) 2916.

[BAS98]S.A.Bass et al., Prog. Part. Nucl. Phys.41, 225 (1998).

[BAS04] R.Bassini, et al, IEEE Transactions on Nuclear Science 51(5): 1931-1935 November 2004.

[BEA00] L. Beaulieu et al., Phys. Rev. Lett. 84, 5971 (2000).

[BERT81] G.F. Bertsch, Phys. Rev. Lett. 46 (1981) 472.

[BERT88] G.F.Bertsch, S. Das Gupta, Phys. Rep. 160, 190 (1988).

[BER09] C.A. Bertulani, arxiv:0908.3275[nucl-th] 22Aug.2009 in memoriam of Giovanni Raciti.

[BES88] J. Besprosvany, S. Levit, Phys. Lett. B 217 (1988) 1.

[BIR83] J.R. Birkelund and J.R. Huizenga, Ann. Rev. Nucl. Part. Sci. 33 (1983) 265.

[BOA90] D.H. Boal et al., Rev. Mod. Phys. 62, 553 (1990).

[BOC00] F. Bocage et al., Nucl. Phys. A 676, 391-408 (2000). (A. Stefanini et al., fiorentini)

[BOI04] C. Boiano et al., IEEE Trans. Nucl. Sci. 5, 1931 (2004).

[BON86] A. Bonasera, Phys. Rev. C 34, 740 (1986) and references therein.

[BON00] A. Bonasera et al., Rivista del Nuovo Cimento 23 N.2, 1 (2000).

[BOMD95] B. J. Bondorf et al., Phys. Rep. 257 (1995) 133.

[BOR83] V. Borrel, et. al. Z. Phys. A314 (1983) 191.

[BORD90] B. Borderie, M.F. Rivet and L. Tassan-Got, Ann. Phys. Fr. 15 (1990) 287.

[BOTE90] W.Botermans, R. Malfiet, Phys. Rep. 198,115 (1990).

[BOT00] R. Botet et al, nucl-ex/0101012 and Phys. Rev. E62 1825 (2000).

[BOW73] J.D. Bowman, W.J. Swiatecki and C.F. Tsang, Lawrence Berkeley Laboratory Report No. LBL-2908, 1973 unpublished.

[BOW93] D.R. Bowman et al., Phys. Rev. Lett. 70, 3534 (1993).

[BRO97] D.A Brown, P. Danielewicz, Phys. Lett. B 398, 252 (1997).

[BRO01] D.A Brown, P. Danielewicz, Phys. Lett. C 64, 014902 (2001).

[CAS12] G. Casini et al., Phys Rev. C86, 011602 (R) (2012).

[CAV90] Cavata C., et al., Phys. Rev. C 42 1760 (1990).

[CES14] D. Cester , et al., Nucl. Instr. Meth. A 735 (2014) 202-206 and references therein.

[CHA10] Charity R. J. et al., Phys. Rev. C 82 (2010) 014610.

[CHE03] L. Chen et al., Phys. Rev. Lett. 90 N 16 (2003) 162701.

[CHO94] P. Chomaz, "The nuclear liquid gas phase transition and phase coexistence: A review", arXiv:nucl-ex/0410024.

[CHO94b] Chomaz Ph. et al, Phys. Rev. Lett. 73 3512 (1994).

[CHO99] Ph. Chomaz and F. Gulminelli Nulc. Phys. A 647 (1999) 153 and references therein.

[CHO03] P. Chomaz, C. R. Physique 4 (2003) 419-423.

[CHO08] P. Chomaz, F. Gulminelli. Phase Transitions in Finite Systems using Information Theory. *Dynamics and Thermodynamics of Systems with Long Range Interactions: Theory and Experiments*, Jul 2007, Assisi, Italy. 970, pp.175-202.

[COL93] M. Colonna et al., Prog. Part. Nucl. Phys. 30, 17 (1993).

[COL95] M. Colonna et al., Nucl. Phys. A 589, 160 (1995).

[COL03] J. Colin et al., Phys. Rev. C 67, 064603 (2003).

[COR95] E. Cornell et al., Phys. Rev. Lett. 75, 1475 (1995).

[CRO93] M. Cronqvist et al., Phys. Lett. B 317 (1993) 505.

[CUG88] J. Cugnon and M.-C. Lemaire, Nucl.Phys. A489 (1988) 781.

[CUN02] A. Cunsolo et al., NIM A 481 48 (2002).

[DAG96] M. D'Agostino et al., Phys. Lett. B 371, 175 (1996).

[DAG00] D'Agostino M. et al, Nucl. Phys. A650 329(1999).

[DAG03] D'Agostino M. et al, Nucl. Phys. A724 (2003) 455.

[DAN01] P. Danielewicz, Nucl.Phys. A 685, 368c (2001).

[DAV01] B. Davin et al., Nucl. Instr. Meth. A463, 302 (2001).

[DAV02] B. Davin et al., Phys. Rev. C 65, 064614 (2002).

[DAY86] R.A.Dayras, et al., Nucl. Phys. A460 (1986) 299.

[DEF94] E.De Filippo et al, NIM A 342 (1994) 527-533.

[DEF05] E. De Filippo et al., Phys. Rev. C 71, 044602 (2005).

[DEF05b] E. De Filippo et al., Phys. Rev. C 71, 064604 (2005).

[DEF12] E. De Filippo et al., Phys. Rev. **C86,** 014610 (2012).

[DEF14] E. De Filippo and A. Pagano Eur. Phys. J A (2014) 50: 32.

[DEF16] E. De Filippo et al., EPJ Web of Conf. 117, 07017 (2016).

[DEF16b] De Filippo E. et al.,, proceedings of the IWM-EC 2016 (Ganil), to be published in Nuovo Cimento C.

[DES90] R.T. DeSouza et al., NIM A 295,109(1990).

[DEY97] P.A. DeYoung et al., Phys. Rev. C 56, 244 (1997).

[DEY00] P.A. DeYoung et al., Phys. Rev. C 61, 024603 (2000).

[DOR00] D. Doré et al., Phys. Lett. B 491 (2000) 15.

[DUR01] D. Durand, et al., "Nuclear Dynamics in the Nucleonic Regime", Ed. CRC Press (2000), chapter 8, pp 220-266.

[ELJTE] http://www.eljentechnology.com/products/plastic-scintillators/ej-299-33a-ej-299-34.

[ELL00] Elliott J. B. et al, Phys. Rev. Lett. 85 1194(2000).

[EVP12] E.V. Pagano, Master Thesis Work, Catania University 2012.

[EVP13] E.V. Pagano, Il Nuovo Cimento 36, n°4, (2013) 9-18.

[EVP13b] E.V. Pagano, T. Minniti, B. Barker, Proc. Of Sci. (BORMIO 2013) 057.

[EVP14] E.V. Pagano, et al., EPJ Web of Conferences 66, 03068 (2014).

[EVP15]E.V. Pagano et al, EPJ Web of Conferences 88, 00013 (2015).

[EVP16] E. V. Pagano et al., proceedings of the IWM-EC 2016 (Ganil), to be published in Nuovo Cimento C.

[EVP16b] E.V. Pagano, et al., EPJ Web of Conference 117, 10008 (2016).

[FERMI51] E. Fermi, Phys. Rev. 81, n° 5 (1951) 683.

[FIO94] L.Fiore, et al. PRC,50,3, (1994) 1709.

[FIS67] M.E. Fisher, Physics 3, 255 (1967).

[FRI90] W.A Friedman et al., Phys Rev. C42, 667 (1990).

[FTDR] FARCOS Technical Design Report (TDR)/INFN.

[FUC06] C.Fuchs and H.H. Wolter, Eur.Phys. J. A 30, 5-21 (2006).

[GEL95] C.J. Gelderloos et al., Phys. Rev. Lett. 75, 3082 (1995).

[GEL99] C. K. Gelbke Prog. Part. Nucl. Phys. 42 (1999) 91-97.

[GER04] E. Geraci et al., Nucl. Phys. A732 (2004) 173-201.

[GER04b] E. Geraci et al., Nucl. Phys. A734 (2004) 524.

[GER11] Lessons of “Heavy Ions Physics”: prof. Elena Geraci, University of Catania (2011), Unpublished.

[GGLP60] G. Goldhaber, S. Goldhaber, W. Lee, A. Pais, Phys. Rev. 120, 300 (1960).

[GHE93] R. Ghetti et al., Nucl. Inst. Meth. A335 (1993) 156.

[GHE93b] R. Ghetti et al., Phys. Rev. Lett. 91, 092701 (2003).

[GHE00] R. Ghetti et al., Nucl. Phys. A 674 (2000) 277-297.

[GHE01] R. Ghetti et al., Phys. Rev. C 64, 017602 (2001).

[GHE01b] R. Ghetti et al., Phys. Rev. Lett. 87, 102701 (2001).

[GOL59] G. Goldhaber, Phys. Rev. Lett. 3, 181 (1959).

[GOL74] A.S. Goldhaber, Phys. Lett. 53B (1974) 306.

[GOL78] A.Golhaber, Phys Rev. C 17 (1978) 2243.

[GON90] W.G. Gong et al., Phys. Lett. B 246 (1990) 21.

[GON91] W.G. Gong et al., Phys. Rev. C43 (1991) 781.

[GON93] W.G. Gong et al., Phys. Rev. C 47, R429 (1993).

[GOS77] J. Gosset, H.H. Gutbrod, et al. Phys. Rev. Cl6 (1977) 629.

[GOU00] D. Gourio et al., Eur. Phys. J A 7, 245 (2000).

[GRE85] C. Grégorie, Procs. Of Winter College on Fundamental Nuclear Physics, Ed. K. Dietrich, M. Di Toro and H. J. Mang, 467 (World Scientific, 1985).

[GRO90] D.H.E. Gross, Rep. Prog. Phys. 53 (1990) 605.

[GRO93] D.H.E. Gross, Nucl. Phys. A 553 (1993) 175c.

[GRO97] D. H. E. Gross, Phys. Rep. 179 (1997) 119.

[GUA97] A. Guarnera et al, Phys. Lett. B403 191 (1997).

[GUE83] D. Guerreau, et al. Phys. Lett. 131B (1983) 293.

[GUE85] D. Guerreau, Nuclear Physics A 447, 37c (1985).

[GUL97] F. Gulminelli and D. Durand, Nucl. Phys. A615 117 (1997) and ref. therein.

[HAN94] D.O. Handzy et al., Phys. Rev. C 50, 858 (1994).

[HAN95] D.O. Handzy et al., Phys. Rev. C 51, 2237 (1995).

[HAN95b] D.O. Handzy et al., Phys. Rev. Lett. 75, 2916 (1995).

[HAR98]C. Hartnack et al., Eur. Phys. J. A 1, 151 (1998).

[HAU98] J.A. Hauger et al., Phys. Rev. C 57, 764 (1998).

[HBT54] R. Hanbury-Brown, R. Q. Twiss, Philos. Mag 45, 663 (1954).

[HBT56a] R. Hanbury-Brown, R. Q. Twiss, Nature 177, 27 (1956).

[HBT56b] R. Hanbury-Brown, R. Q. Twiss, Nature 178, 1046 (1956).

[HEN12] Henzl V. et al., Phys. Rev. C, 85 (2012) 014606.

[HIN87] D. J. Hinde, J. R. Leigh, J. J. M. Bokhorst, J. O. Newton, R. L.Walsh, and J. E. Boldeman, Nucl. Phys. A472, 318 (1987) 044602.

[JAE92]J. Jaenicke et al., Nucl. Phy. A 536, 201 (1992).

[KIM92] Y. D. Kim et al., Phys. Rev. C45 (1992) 338.

[KIM92b] Y. D. Kim et al., Phys. Rev. C45 (1992) 387.

[KNO00] Radiation detection and measurement, Glenn F. Knoll, Wiley, third edition (2000).

[KOO77] S. E. Koonin Phys. Lett. B70, 1, (1977) pg. 43-47.

[KOT99] R. Kotte and H.W. Barz, Eur. Phys. J A 6, 185 (1999).

[LAN97] G. Lanzanò et al., Il Nuovo Cimento Vol 110 A N° 5 (1997).

[LAN01] G. Lanzanò et al., Nucl. Phys. A683, 566 (2001).

[LAR97] Y. Larochelle et al., Phys. Rev. C 55, 1869 (1997).

[LAW14] C.C. Lawrence, et al., Nucl. Instr. Meth. A 759 (2014) 16-22 and reference therein.

[LEC95] J.F. Lecolley et al., Phys. Lett. B 354, 202 (1995).

[LED96] R. Lednicky et al., Phys. Lett. B 373 (1996) 30.

[LEF00] T. Lefort et al., Nucl. Phys. A 662, 397 (2000).

[LIS91]Lisa M. A., Gong W. G., Gelbke C.K. and Lynch W. G., Phys. Rev. C 44 (1991) 2865.

[LIS93] M. A. Lisa et al., Phys. Rev. Lett. 70, 2545, (1993).

[LIS05] M. A. Lisa et al., Ann. Rev. Nucl. Part. Sci. 55357 (2005).

[LUC97] J. Lukasik et al., Phys. Rev. C 55, 1906 (1997).

[LUK97] J. Lukasik et al., Phys. Rev. C 55, 1906 (1997).

[LYN95] W. G. Lynch, Nucl. Physics A583(1995),471-480.

[MAR95] L. Martin et al., Nucl. Phys. A583, 407 (1995).

[MDT10] M. Di Toro et al., J.Phys. **G37,** 083101 (2010).

[MEN83] A. Menchaca-Rocha, et al. Phys. Lett. 131B (1983) 31.

[MER85] M.C. Mermaz, et al.; Nucl. Phys. A441 (1985) 129.

[MIL98] P.M. Milazzo et al. Phys. Rev. C 58, 953 (1998).

[MIL01] P.M. Milazzo et al., Phys. Lett. B 509, 204(2001).

[MIL02] P.M. Milazzo et al., Nucl. Phys. A 703, 466 (2002).

[MON94] C.P. Montoya et al, Phys. Rev. Lett. 73, 3070(1994).

[MOR78] D.J. Morrissey, et al. Phys. Rev. Cl8 (1978) 1267.

[MORE97] L. Moretto et al., Phys. Rep. 287 (1997) 249-336.

[MUR84] M.J. Murphy, Phys. Lett. B 135 (1984) 25.

[NAT81] J.B. Natowitz, et al. Phys. Rev. Lett. 47 (1981) 1114.

[NAT02] J.B. Natowitz, et al. Phys. Rev C65 034618 (2002).

[NAT02b] J.B. Natowitz, et al. Phys. Rev C66 031601(R) (2002).

[NAT02c] J.B. Natowitz, et al. Phys. Rev Lett. 89 (2002) 212701.

[NGO78] C. Ngo and M. Lefort, Ann. De Phys. 3, 5 (1978).

[NSE14] See : Nuclear Symmetry Energy, Topical Issue, European Physics Journal A50, 2 (2014), Edited by B. A. Li, A. Ramos, G. Verde, I. Vidana.

[NYI13] S. Nyibule et al, Nucl. Inst. Meth. A 728 (2013) 36-39.

[OGI91] C. Ogilvie et al., Phy. Rev. Lett. 67, 1214(1991).

[PAG04] A. Pagano et al., Nucl. Phys. A 734 504-511 (2004).

[PAG12] A. Pagano Nucl. Phys. News Vol 22 N1 (2012) 25.

[PAP01] Papa M., Maruyama T. and Bonasera A., Phys. Rev. C, 64 (2001) 024612.

[PAP07] Papa M. et al., Phys. Rev. C, 75 (2007) 054616.

[PAPP14] A. Pappalardo, et al., IEEE Jour. Of Sel. Top. In Qua. Elect. 20, 6 (2014).

[PEI94] G.Peilert, H.Stocker and W.Greiner, Rep. Prog.Phys. 57 (1994) 533-602 and references therein.

[PIA02] S. Piantelli et al., Phys. Rev. Lett. C 885, 052701 (2002).

[POC95] J. Pochodzalla al., Phys. Rev. Lett. 75, 1040 (1995).

[POL12] E. Pollacco et al.m Phys. Procedia 37 1799-1804 (2012).

[POP98] R. Popescu et al. Phys. Rev. C 58, 270 (1998).

[POZ13] S.A. Pozzi, Nucl. Instr. Meth. A 723 (2013) 19-23, and references therein

[PRA84] S. Pratt, Phys. Rev. Lett. 53, 1219 (1984).

[PRA87] S. Pratt and B. Tsang Phys. Rev. C36 (1987) 2390.

[QUA14] L. Quattrocchi et. al., EPJ Web of Conferences 66 11001 (2014).

[RAN81] J. Randrup and S.E. Koonin Nucl. Phys. A356 (1981) 223-234.

[RAN82] J. Randrup Nucl. Phys. A383, 468 (1982) and reference therein.

[RAM84] F. Rami, et. al, Z. Phys. A318 (1984) 239.

[RAM85] F.Rami, Nucl. Phys. A444 (1985) 325.

[RIC01] J. Richter and P. Wagner Phys. Rep. 350, 1 (2001).

[RIV96] M.F. Rivet, et al. Physics Letters B, Elsevier, 1996, 388, pp.219-223

[RIV01] M. R. Rivet et al., Procs. Of Int. Workshop on Multifragmentation and related topics, IWM2001, Catania, Italy, Nov. 2001, 11.

[RIZ08] J. Rizzo et al., Nucl. Phys. A 806, 79 (2008).

[RUS10] P.Russotto, et al., Phys. Rev. C 81, 064605 (2010).

[RUS14] P.Russotto, et al., Jour. Of Phys.: Conf. Ser. 515 012020 (2014]

[RUS15] P.Russotto, et al., Phys. Rev. C 91, 014610 (2015).

[RUS16] P. Russotto et al., Phys. Rev. C94, 034608 (2016).

[SAN95] T. C. Sangster et al. Phys. Rev. C 51, 1280 (1995).

[SCH90] P. Schotanus and R. Kamermans IEEE Trans, Nucl. Sci. 37, 177 (1990).

[SCHA94] O. Schapiro, A.R. DeAngelis, D.H.E. Gross Nucl. Phys. A568 (1994) 333-349.

[SCHA94b] O. Schapiro, D.H.E. Gross Nucl. Phys. A576 (1994) 428-440.

[SCO83] D.K. Scott, Nucl. Phys. A409 (1983) 291C.

[SDL16] S. De Luca PhD thesis, Università di Messina, XXIX Ciclo (2013-2016).

[SHA55] R.S. Shankland, et al., Rev. Mod. Phys., 27, 167, (1955).

[SHU74] E.V Shuryak, Phys. Lett B44, 387 (1973).

[SOB97] L.G. Sobotka et al., Phys. Rev. C 55, 2109 (1997).

[STDR] T. Kobayashi, T. Motobayashi, K Yoneda, et al. SAMURAI TPC Project, MSU http://ribf.riken.jp/SAMURAI/120425SAMURAIConstProp.pdf.

[STE95] A.A. Stefanini et al, Zeit. Phys. A 351, 167 (1995).

[STEI15] A. Steine et al., W.G. Newton, Phys. Rev. C91, 015804 (2015).

[SUN10] Z.Y. Sun, et al., Phys. Rev. C82, 051683(R) (2010).

[SWE87] L. S. Swenson, Jr Physics Today 40, 24 (May, 1987).

[TOK95] J. Töke, et al. , Phys. Rev. Lett. 75, 2920 (1995).

[TSA96] B. Tsang et al., Phys. Rev. C 53, R1057 (1996).

[VAN73] R. VandenBosh/J.Huizenga, Academic Press NY and London, 1973.

[VDR81] J. van Driel, et al., Phys. Lett., 98B, 5, (1981) pg. 351-354.

[VER02] G. Verde et al., Phys. Rev. C 65, 054609 (2002).

[VER06] G. Verde et al., Eur. Phys. J A 30, 81 (2006).

[VER07] G. Verde et al., Phys. Lett. B 653, 12 (2007).

[VER13] G. Verde et. al., Journal of Physics: Conference Series 420 (2013) 012158.

[VIO85] Viola V. E., Kwiatkowski K. and Walker M., Phys. Rev. C, 31 (1985) 1550.

[VOL97] S. Voloshin et al., Phys. Rev. Lett. 79, 4766 (1997).

[WAG01] A. Wagner et al., Nucl. Instr. And Meth. A 456, 290 (2001).

[WEI35] *von Weizsäcker, C. F. (1935). "Zur Theorie der Kernmassen". Zeitschrift für Physik (in German). **96** (7–8): 431–458.Bibcode:1935ZPhy...96..431W. doi:10.1007/BF01337700.*

[WES76] G.D. Westfall, et al. Phys. Rev. Lett. 37 (1976) 1202.

[WIL76] J. Wilczyinski, Phys. Lett. 47B , 6, (1976) 484.

[WIL05] J. Wilczyński *et al.*, Int. J. Mod. Phys. E **14**, 353 (2005).